Petrographical evolution of reservoir formations in the Edvard Grieg field, North Sea - a study of porosity, permeability and pore geometry development through time.

Ørjan Markussen

Dissertation for the degree of Philosophiae Doctor (Ph.D.)

Faculty of Mathematics and Natural Sciences
Department of Geosciences
University of Oslo
Norway

Series of dissertations submitted to the
Faculty of Mathematics and Natural Sciences, University of Oslo
No. 2095

ISSN 1501-7710

Cover: Hanne Baadsgaard Utigard.
Print production: Reprosentralen, University of Oslo.

Preface

This Ph.D. thesis, entitled "Petrographical and mineralogical evolution of reservoir formations in the Edvard Grieg field, North Sea - a study of porosity, permeability and pore geometry development through time" has been submitted to the Department of Geosciences at the University of Oslo (UiO) in accordance with the requirements for the degree of Philosophiae Doctor (Ph.D.). This Ph.D. work has been conducted at the Department of Geosciences at the University of Oslo and at Lundin Norway in the period 2014-2018. It was supervised by Prof. Henning Dypvik (UiO) and co-supervised by Dr. Erik Hammer, Lundin Norway.

This Ph.D. project was funded by Lundin Norway AS and partners of PL338 licence and is concerned with analysing the evolution of reservoir quality of highly complex deposits in the Edvard Grieg field, Utsira High, Norwegian North Sea. The objective is to better understand the evolution of reservoir properties and which again can result in optimising future well placements and drainage strategies. The study was accomplished using various methods, both traditional petrographic analyses and advanced 3D micro-CT scanning techniques. Supplementary FMI azimuth data, conventional well logs (Gamma ray, sonic, neutron-density, resistivity) and seismic analyses were also used to gain a better overview of the basin evolution. Core sampling and logging description was carried out at Weatherford Laboratories in Stavanger, while 3D micro-CT scanning was done by ThermoFisher Scientific (previously FEI Trondheim) and the Natural History Museum in Oslo.

The dissertation consists of project introduction, a theoretical background and three scientific papers, of which two are already published in international journals. The third paper has been submitted to Marine and Petroleum Geology. The main results from these papers have also been presented to the scientific community during several conferences, both as poster and oral presentations. Paper 1 explores the diagenetic evolution and reservoir quality of the Edvard Grieg reservoir rocks. Paper 2 focusses on nano- to micro-porosity distribution in 3D and the effects of various cements on the reservoir quality. Paper 3 combines much of the previously gathered data, with a focus on refined semi-automatic grain size quantification methods, to explain the relation between basin development, provenance and sediment infill.

IMPORTANT NOTE: Please be advised that from August, 2018, the authors name was legally changed from Orhan Mahmic to Ørjan Markussen.

Acknowledgments

After an intensive learning period, not only in the scientific arena, but also on a personal level, writing this note of thanks is the finishing touch to my dissertation. Undertaking this Ph.D. has been a truly life-changing experience for me and it would not have been possible without the support and guidance that I received from many people.

I owe my first and foremost gratitude to my main supervisor Prof. Henning Dypvik (UiO) for his continuous support of my Ph.D. study, for his patience, motivation, and immense knowledge. He has always been available for valuable discussions and guidance. I could not imagine having a better adviser and mentor for my Ph.D. study.

I would also thank my co-supervisor Dr. Erik Hammer (Lundin Norway AS) who responded to my questions, improved my manuscripts and shared his time and professional knowledge.

I would like to thank Lundin Norway AS and partners of PL338 licence for sponsoring this project, providing the core material, giving permission to publish the results, and for stimulating discussions and meetings.

Appreciations go also to all my teaching and working colleagues. In particular I thank Adrian Read, Øyvind Hammer, Maarten Aerts, Berit Løken Berg, Salahalldin Akhavan, Knut Bjørlykke, Mufak Said Naoroz, Åsgeir Seland, Thanusha Naidoo, Thor Axel Thorsen, Muriel Marie Laure Erambert, Helge Hellevang, and Siri Simonsen for various kinds of help during my Ph.D. study. I would like to also thank all my office friends; Lars Riber, Katrine Fossum and Christian Sætre for the great company and interesting discussions.

I would like to thank my family: my parents and my sister for their constant support and believing in me. Finally, and most importantly, my deepest gratitude goes to my fantastic and dear wife Chloé who always gave support, love and encouragement, and a lot of patience throughout these years. Je t'aime.

List of Papers

The papers and abstracts, listed below, will in the following be referred to as Paper/Abstract 1 to 3.

Paper 1: Mahmic, O., Dypvik, H. and Hammer, E. (2018). Diagenetic influence on reservoir quality evolution, examples from Triassic conglomerates/arenites in the Edvard Grieg field, Norwegian North Sea. Marine and Petroleum Geology, 93, 247-271.

Paper 2: Markussen, Ø., Dypvik, H. Hammer, E., Long, H. and Hammer, Ø. (2019). 3D characterization of porosity and authigenic cementation in Triassic conglomerates/arenites in the Edvard Grieg field using 3D micro-CT imaging. Marine and Petroleum Geology. 10.1016/j.marpetgeo.2018.10.015.

Paper 3: Markussen, Ø., Dypvik, H. and Hammer, E., (2019) Basement clast distribution and sedimentary facies analysis of alluvial fan conglomerates, Edvard Grieg field, North Sea. Unpublished manuscript, submitted to MPG (2019).

Conference abstracts

Abstract 1: Mahmic, O., Dypvik, H. and Hammer, E. (2016). 3D petrographic imaging and diagenetic modelling of reservoir cores at multiple scales. GSA2016, Denver, Colorado, USA.

Abstract 2: Mahmic, O., Dypvik, H. and Hammer, E. (2016). 3D petrographic imaging and diagenetic modelling of reservoir formations. NGF Winter meeting, Helsinki.

Abstract 3: Mahmic, O., Dypvik, H. and Hammer, E. (2017). Multi-scale 3D imaging and quantification of diagenetic phases in siliciclastic reservoirs. NGF Winter meeting, Oslo.

Table of Contents

1. Introduction

The North Sea rift system is considered to be one of the most important hydrocarbon provenances in the Arctic -North Atlantic region. The Utsira High is a large intra-basinal structural high, flanked by the Viking Graben to the west and the Stord Basin to the east (Fig. 1A), and it has probably been a positive element since the Late Palaeozoic (Laursen et al., 1995). Since oil exploration started on the Norwegian shelf, there have been several successful discoveries in the northern and central part of the Utsira High region, such as Balder, Sleipner, Heimdal, Ringhorne, Grane and Jotun.

During the 90s Statoil (now Equinor) drilled two wells in the Utsira High, wells 16/1-4 and 16/1-5. Both wells were drilled to basement. The basement rocks found in these two wells consist of mainly brecciated igneous rocks with minor gas/condensate discoveries (NPD, 2018). Well 16/1-4 revealed sedimentary rocks of Quaternary, Tertiary, and Cretaceous age. The well was abandoned on 13 April 1993. Well 16/1-5 was also abandoned due to only minor hydrocarbon shows in a thin Cretaceous limestone sequence above the Heather Formation, and in the upper 8 metres of the Heather Formation sandstone (NPD, 2018). In 2004 Lundin Norway AS acquired the operatorship (65%) of the licence PL338, which included these two wells (Bøe, 2014). The remaining 50% of the licence belongs to the companies partners; OMV Norge (20 %), Wintershall Norge (15 %). The most recent oil discovery in the Southern Utsira High was made by the well 16/1-25S in fractured porous granitic basement, Rolvsnes (Fig. 1C) (Lie and Nilsen, 2016).

The Edvard Grieg oil discovery was made by Lundin Norway AS in well 16/1-8 (2007) (Fig. 1). It is located in the Utsira High (block 16/1) 35 km south of Grane and Balder in the central North Sea, production licence PL338. It was further evaluated in appraisal wells 16/1-10, 16/1-13, 16/1-18, and 16/1-23S, all being part of the Luno basin. In the northern segment, the Tellus well, 16/1-15, proved a ca. 50 metre oil column in a thin Cretaceous sandstone overlying porous / fractured basement. The segment was found to have pressure communication with the main Edvard Grieg discovery to the south.

Nearby well 16/1-12 carry oil in fractured porous basement to the south of Edvard Grieg while well 16/1-14 demonstrated oil in two Paleocene sand levels; the Balder and Lista/Heimdal and light oil in Lower Cretaceous sandstone.

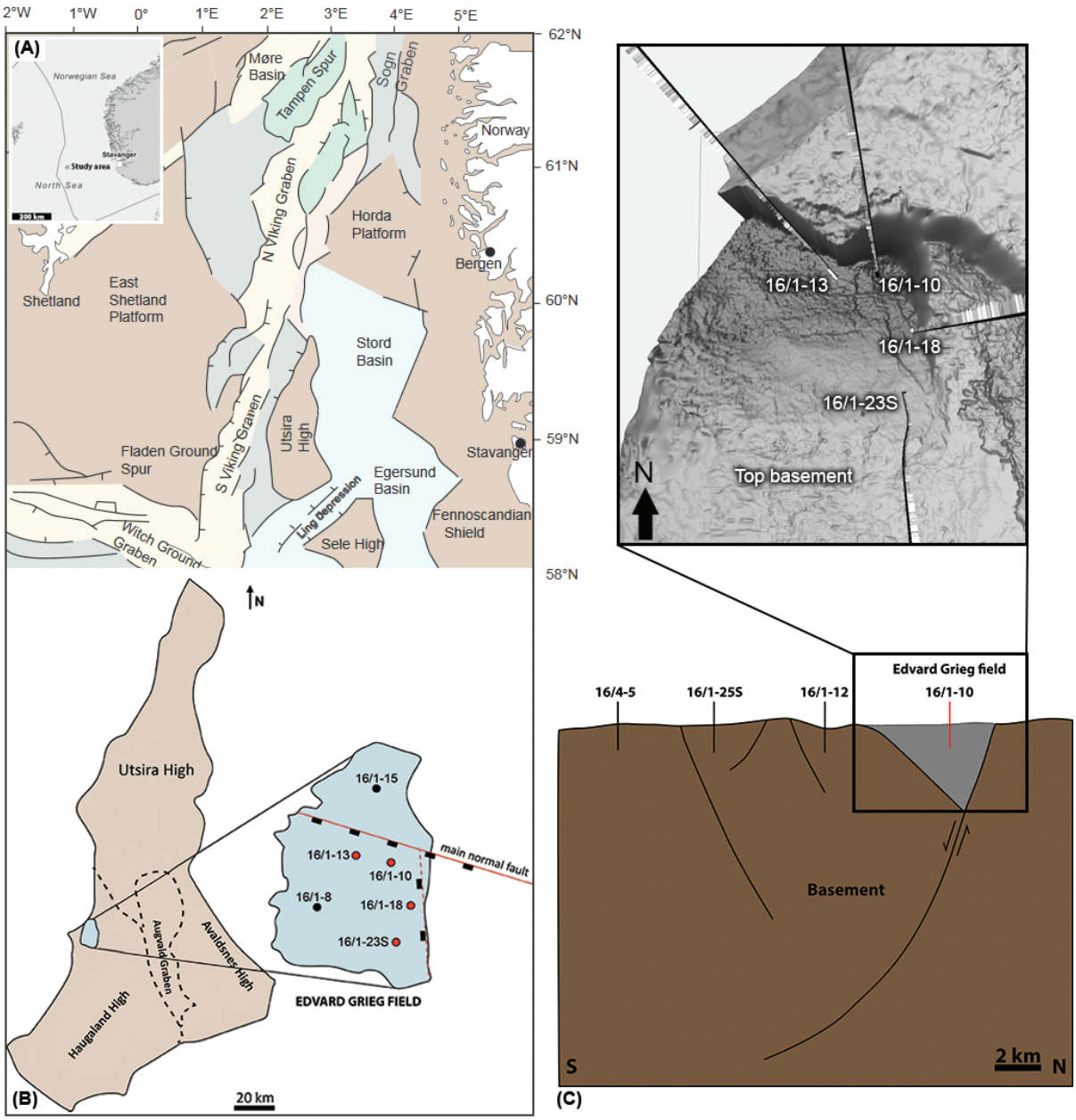

Figure 1 - (A) Regional map, showing the main fault trends, shear zones (grey lines) and different grabens and structural highs in the northern North Sea. (Modified from Riber et al., 2015) (B) Well map showing the wells used in this study (red circles), major normal fault (solid red line) and a minor normal fault (dashed red line). (C) Fault systems on the Southern Utsira High (Haugaland High) and Edvard Grieg field (Modified from Lie and Nilsen, 2016).

Earlier exploration of the licence area included well 16/1-4 up-dip, proving gas/condensate in reworked basement rocks, and well 16/1-5 down-flank finding good oil shows in a Hugin sandstone (Fig. 2). Well 16/1-17 was drilled in the P-graben system east of Luno and found conglomerates of poor reservoir quality overlying granitic basement.

The Triassic reservoirs in the North Sea are commonly located on tilted-fault blocks and their reservoir quality is mainly controlled by the initial depositional facies. The Triassic deposits usually did not undergo significant late-burial diagenesis, in particular compaction, which may be related to development of early diagenetic framework (e.g. grain-coats and early carbonate cement) (Goldsmith et al., 2003). The Edvard Grieg reservoir rocks span in age range from Late Ordovician - Early Silurian (440 Ma) to Early Cretaceous (140 Ma) (Lundin, 2014). The oldest reservoir is located in 440 million year old fractured and weathered granitic basement rocks (see e.g Riber et al., 2015). The main reservoir consists of Upper Triassic to Lower Cretaceous alluvial, aeolian and shallow marine conglomerates and sandstones (Goldsmith et al., 2003; Lundin, 2014). 50 m of Triassic/Jurassic(?) aeolian sandstone with excellent reservoir quality was encountered in well 16/1-13 at a vertical depth of c. 1900 m.

1.1. Regional geological setting

The stratigraphic and structural development of the northern North Sea basin has been extensively studied in the course of intensive petroleum exploration. The hydrocarbon traps are mainly localized in rocks of Devonian to Eocene age (Slagstad et al., 2011). The older basement units were therefore often excluded from investigations due to high drilling risk and costs. However, a few wells have confirmed the presence of pre-Permian sediments below the northern North Sea (Slagstad et al., 2011; Nøttvedt et al., 1995). The Caledonian orogeny was dominated by compressional tectonics and today forms part of the crystalline basement underlying the North Sea (Ziegler, 1990; Bartholomew et al., 1993; Slagstad et al., 2011). During post-Caledonian time the North Sea rift system, including the Viking and Sogn Grabens, underwent several major tectonic phases of basin evolution, e.g. the Permo-Triassic rifting, and the Upper Jurassic-Lower Cretaceous episodes. This is described in the literature, e.g. Ziegler, 1975; Ziegler,1990; Bartholomew et al., 1993; Gregersen et al., 1997; Laursen et al., 1995; Slagstad et al., 2011; Ziegler, 1992; Yielding et al., 1992; Milton, 1993; Rattey and Hayward, 1993;

Nøttvedt et al., 1995; Roberts et al., 1995; Færseth, 1996; Christiansson et al., 2000; Faleide and Berge, 2000; Odinsen et al., 2000; Isaksen and Ledje, 2001; Rupke et al., 2008. The rifting produced an approximately 150-200 km wide N-S trending zone of extension, flanked by the Norwegian mainland to the east and Shetland Platform to the west (Nøttvedt et al., 1995, Færseth and Ravnås, 1998).

The North Sea is composed of several major Mesozoic grabens and highs (Fig. 1) (Gregersen et al., 1997). The Utsira High is one of these large intra-basinal structural highs with intracratonic sedimentary basins, where Edvard Grieg field has been discovered. One of the principles for development of a major sedimentary basin on continental crust is thinning of the crust and the lithosphere. In order to obtain tectonic equilibrium, the result is subsidence of the area (Faleide et al., 2015).

The first rifting phase took place from Permian to earliest Triassic. During this time the Zechstein Sea advanced southwards from the Norwegian-Greenland Sea rift and flooded the Permian basins. Repeated deglaciation and glaciation of Gondwana (Van Der Baan, 1990), and eustatic sea level fluctuation resulted in accumulation of the highly cyclical Zechstein carbonate, sulphate and halite series (Fig. 2) (Isaksen and Ledje, 2001; NPD, 2018).

During the transition from Permian to Triassic, rifting accelerated in the Norwegian-Greenland Sea (Ziegler, 1990; Isaksen and Ledje, 2001), and large rotational movements on the major fault blocks commenced (Steel, 1993). In the northern and central North Sea, the Triassic is composed of continental red bed facies deposited in an arid to semi-arid climate, with shales dominating in the Lower and Middle Triassic and more sandy units in the Upper Triassic (Fig. 2) (Ziegler, 1990; Isaksen and Ledje, 2001). The Upper Triassic to Middle Jurassic sedimentary infill increase in thickness towards the basin centre, with signs of subtle discrete rift-pulses (Ziegler, 1990; Yielding et al., 1992). Erosion of the uplifted fault-blocks led to deposition of nonmarine sandstones on the western flank of the Utsira High (Isaksen and Ledje, 2001). Since the end of Jurassic the rifting has been followed by general thermal subsidence. During this time widespread transgression with deep water sedimentation took place as a consequence of eustatic sea level rise. Following the transgression, shales, often calcareous, with frequent thin interbedded sandstone units were deposited in a low energy shallow to deep marine environment, often of turbiditic origin (Vollset and Doré, 1984). The organic-rich shales of the Draupne

Formation (Fig. 2) were deposited during this period, and are the main source rock in the Viking Graben (Isaksen and Ledje, 2001). During the late Kimmerian another rifting phase took place and partly reactivated the existing faults systems (Ziegler, 1975). This rifting pulse affected mainly the Viking and Central grabens, with subsidence of rotational blocks (Ziegler, 1992; Isaksen and Ledje, 2001). Following the late Kimmerian phase, the rate of crustal extension across the North Sea Graben system diminished gradually (Gowers and Sæbøe 1985; Ziegler; 1992, Isaksen and Ledje, 2001).

1.2. Stratigraphy

The crystalline basement rocks of the North Sea consists of Silurian and Ordovician medium to high grade metamorphic rocks with associated plutons, and were deformed during the Caledonian orogeny (410 - 450 Ma) (Frost et al., 1981; Barton and Wood, 1984).

The sediments of the Rotliegendes Group (Lower Permian) (Fig. 2) rest on the metamorphic basement and consist of clastic sequences of clays, shales, sandstones and conglomerates (Stemmerik et al., 2000; Heeremans and Faleide, 2004; Glennie, 2009; NPD, 2018). The thickness varies substantially, with maximum thickness in the UK Sector. The sandstones of the group are present in the South Viking Graben (Fig. 2) but absent on the local structural highs, e.g. Utsira High and Horda Platform (Fig. 1). The Rotliegendes Group consists of aeolian, fluvial, lacustrine, sabkha and some acid volcanic depositional environments (Glennie, 2009). Overlying the Rotliegendes Group is a thick succession of evaporites and carbonates of the Zechstein Group (Jackson et al., 2010). The sedimentary rocks of the Zechstein Group are widely spread and represent shallow marine water deposition during a fairly arid climate (Isaksen and Ledje, 2001). The group is absent east and north of the Utsira High.

The Zechstein Group is succeeded by the Triassic non-marine Smith Bank (shale-dominated) and Skagerrak (interbedded conglomerates, sandstones, siltstones and shales) formations which are widely distributed throughout the central North Sea (Fig.2). The Skagerrak Formation may have gradational or sharp contact with the underlying Smith Bank Formation. The Smith Bank Formation conformably overlies the Permian sediments, while the Skagerrak Formation is

unconformably overlain by Jurassic and younger sediments. The Smith Bank Formation may locally rest directly on basement rocks (well 10/8-1) (NPD, 2018).

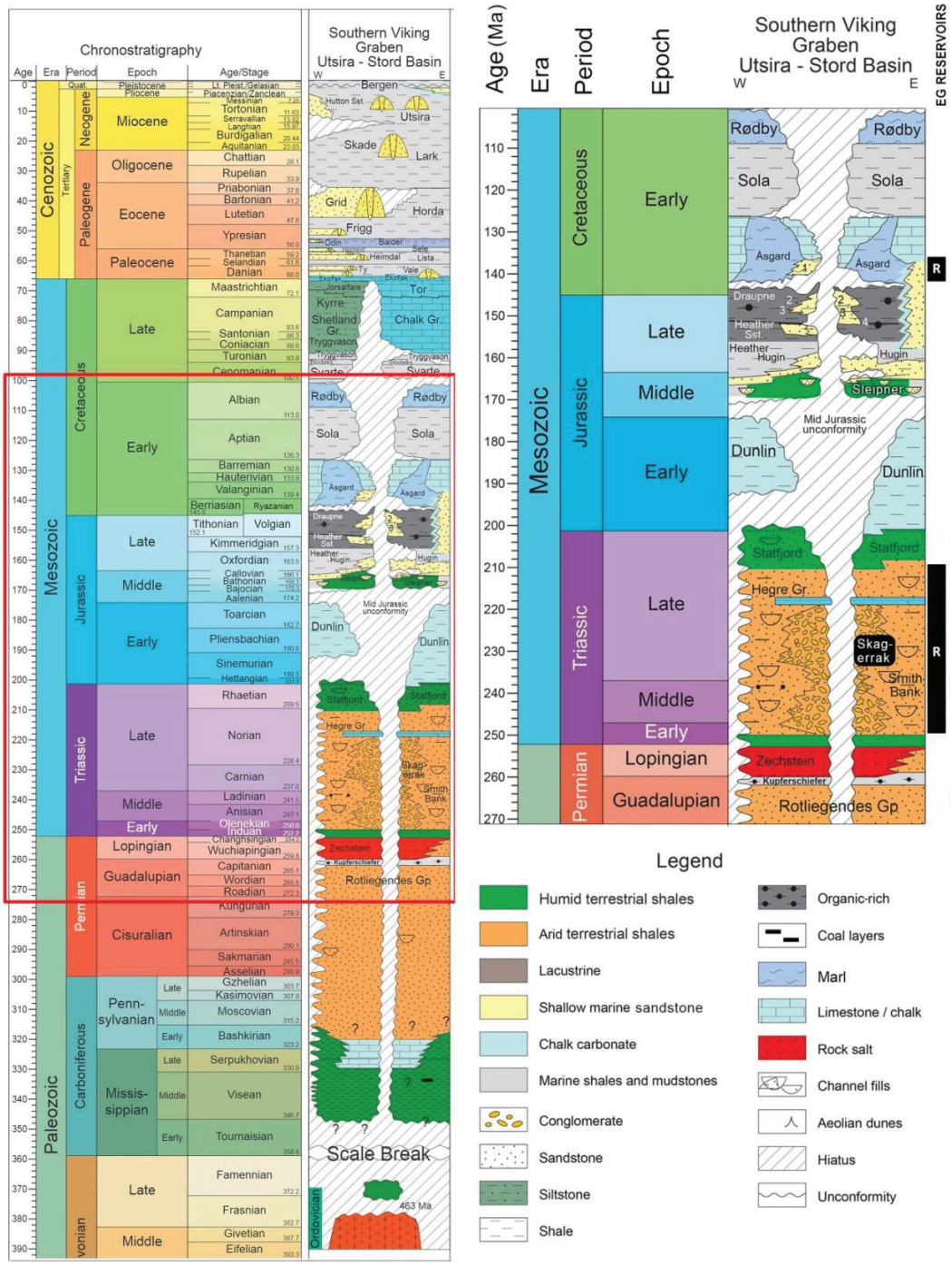

Figure 2 - Stratigraphic column of the Norwegian sector of the South Viking Graben, Utsira and Stord Basin. The main Edvard Grieg reservoir in the Triassic and early Cretaceous rocks (R) is indicated in the right figure. (Modified from NORLEX, 2012)

The Vestland Group (Sleipner, Hugin, Bryne, Sandnes, and Ula formations) of Middle to Upper Jurassic is widely distributed in the southern Northern North Sea and dominated by sandy deltaic sequences with silty and shaly layers and coal horizons (NPD, 2018). The sandy, deltaic Vestland Group overlies the Lower Jurassic shales of the Dunlin Group. The clay-rich Viking Group (Heather and Draupne formations) (Fig. 2) is present in the southern parts of the platform. Both thick- and thin-skinned normal faulting influenced the Middle and Upper Jurassic depositional successions. This led to thickening of the Middle and Upper Jurassic stratigraphic units towards the rift-related faults (Jackson et al., 2010). Post-rift successions from the Cretaceous to the present day are present in most of the wells (Fig. 2).

1.3. Objectives and scope of the study

Reservoir quality is one of the major controls on prospectivity during petroleum exploration. Therefore it is important to have a comprehensive understanding of what controls and influences reservoir quality, i.e. diagenesis, to help target further exploration and evaluation efforts (Selley, 1997).

This project is concerned with the petrological and mineralogical alterations in siliciclastic sediments through time, at the Edvard Grieg field, Utsira High (Fig. 1). The overall scientific aim of the Ph.D. project was to generate new data and improve on our understanding of the evolution of weathering, particle generation, sedimentation, porosity and permeability (P&P), and diagenetic changes in these sediments through time. The goal is that highlighting and explaining the complex, heterogeneous nature of the sediments from the Edvard Grieg field will provide predictive understanding of the properties of carrier beds and reservoir rocks in this already well known petroleum area. The main focus was on the Permo-Triassic siliciclastic rock cores from wells 16/1-10, 16/1-13, 16/1-18 and 16/1-23S (Fig. 1). Furthermore, these Permo-Triassic siliciclastics were compared to the underlying fractured basement rocks, in order to better understand the variabilities in the mineralogy and possible source (provenance). The degree of weathering in the conglomerate material vs. basement rocks was also investigated.

New knowledge of the internal pore structure (micro-fractures versus secondary dissolution porosity) of reservoir rocks at the Edvard Grieg field may help provide a better assessment of the

different production conditions. By utilising the high resolution micro-CT scan imaging method, it is possible to attain much better resolution of rock fabric and texture, giving important and detailed information on the pore space and pore connectivity (Markussen et al., 2019).

The mineralogical composition of the matrix, various cements and grains, was also of major importance in this study. The results were used to construct series of 3D rock models of selected reservoir rocks, from various geological time periods and geological settings, in order to understand the distribution of reservoir properties, applicable for exploration and development of reservoirs in the area (Markussen et al. submitted).

1.4. Analytical methods and samples

The Edvard Grieg field reservoirs are mostly composed of heterogeneous deposits. Integration of different analytical methods, i.e. standard petrographic, mineralogical and geochemical techniques, and semi-automatic core image analyses was used to evaluate the diagenetic history of these deposits. By applying advanced non-destructive 3D micro-CT scan technology and modelling programs it is also possible to gain additional new knowledge on basement weathering and particle generation, as well as on P&P development, and sediment transportation and deposition (Fig. 3).

The petrographical analyses were carried out by the application of optical and scanning electron microscope (SEM) as well as detailed X-ray diffraction analyses of both bulk samples and clay fractions for all identified facies associations.

A total of 100 samples from full-diameter cores from Triassic (Skagerrak Formation) conglomeratic and sandstone dominated successions in wells 16/1-10, 16/1-13, 16/1-18 and 16/1-23S were used for petrographic and diagenetic studies of the Edvard Grieg field deposits (Table 1 and Papers 1-3). Furthermore, high-resolution photographs were taken of all the cores and used for semi-automatic sizing and quantitative distribution of basement clasts (see Section 1.4.1 and Paper 3).

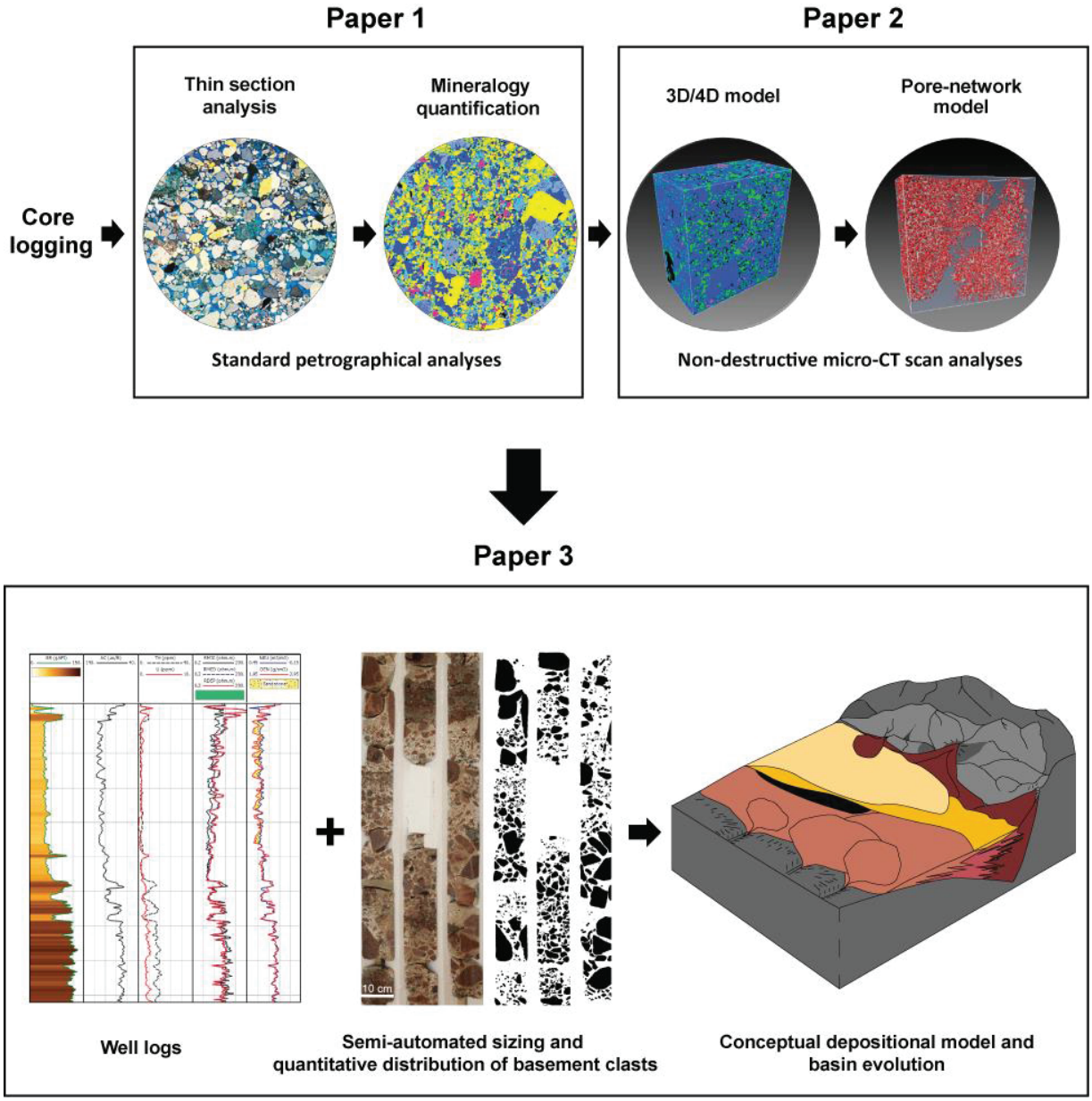

Figure 3 - Workflow undertaken during the Ph.D. study, with core logging, 2D petrographical analyses, and diagenesis study first (Mahmic et al., 2018), then further 3D analyses of representative samples (Markussen et al., 2019). The initial data was then used in combination with well logs + seismic (not included in the Paper 3), semi-automatic grain-size and clast type analysis to shed light on the basin evolution and lithology distribution both vertical and lateral through time (Markussen et al., submitted).

Table 1 - Overview of the four wells and the studied depth intervals in each well. The Skagerrak Formation base was not reached in any of these cores.

Well	Total core length (m)	Core number	Depth interval
16/1-10	92	3-5	1898.10 - 1987.60 mDD
16/1-13	81	3-5	1919.70 - 2001.10 mDD
16/1-18	91	1-8	1896.00 - 1986.00 mDD
16/1-23S	124	3-8	1955.50 - 2064.50 mDD

1.4.1. Semi-automated sizing and quantitative distribution of basement clasts

Full automatic grain-size separation techniques (e.g. McEwan et al., 2000; Butler et al., 2001; Reid et al., 2001; Sime and Ferguson, 2003) from core photos proved challenging to implement in this study. There are several factors that can affect the quality of the image, such as illumination conditions (adding noise in the pictures), low visible contrast between basement clasts and matrix, and low resolution. Therefore, a semi-automatic approach was developed (Fig. 4) and used to quantify basement clasts sizes in the conglomeratic successions. This methodology is shown to be effective time-wise and produces more accurate representation of the clast size distribution than manual counting.

The quantification and characterisation of the basement clasts was done to better understand their distribution and possible changes in the provenance area. The clast versus matrix content is an important factor concerning reservoir quality, since the basement clasts normally are considered close to impermeable. The lithologies with high abundance of basement clasts have reduced reservoir quality compared to more sand-rich lithologies. In addition, due to the high feldspar content in these clasts, traditional well logs fail to recognise sandy units (elevated gamma ray values).

Results from these analyses showed seven commonly occurring basement clast types (which) in the cores from four wells, 16/1-10, 16/1-13, 16/1-18 and 16/1-23S. These have been identified based on their modal composition and visual differences from high resolution core photos.

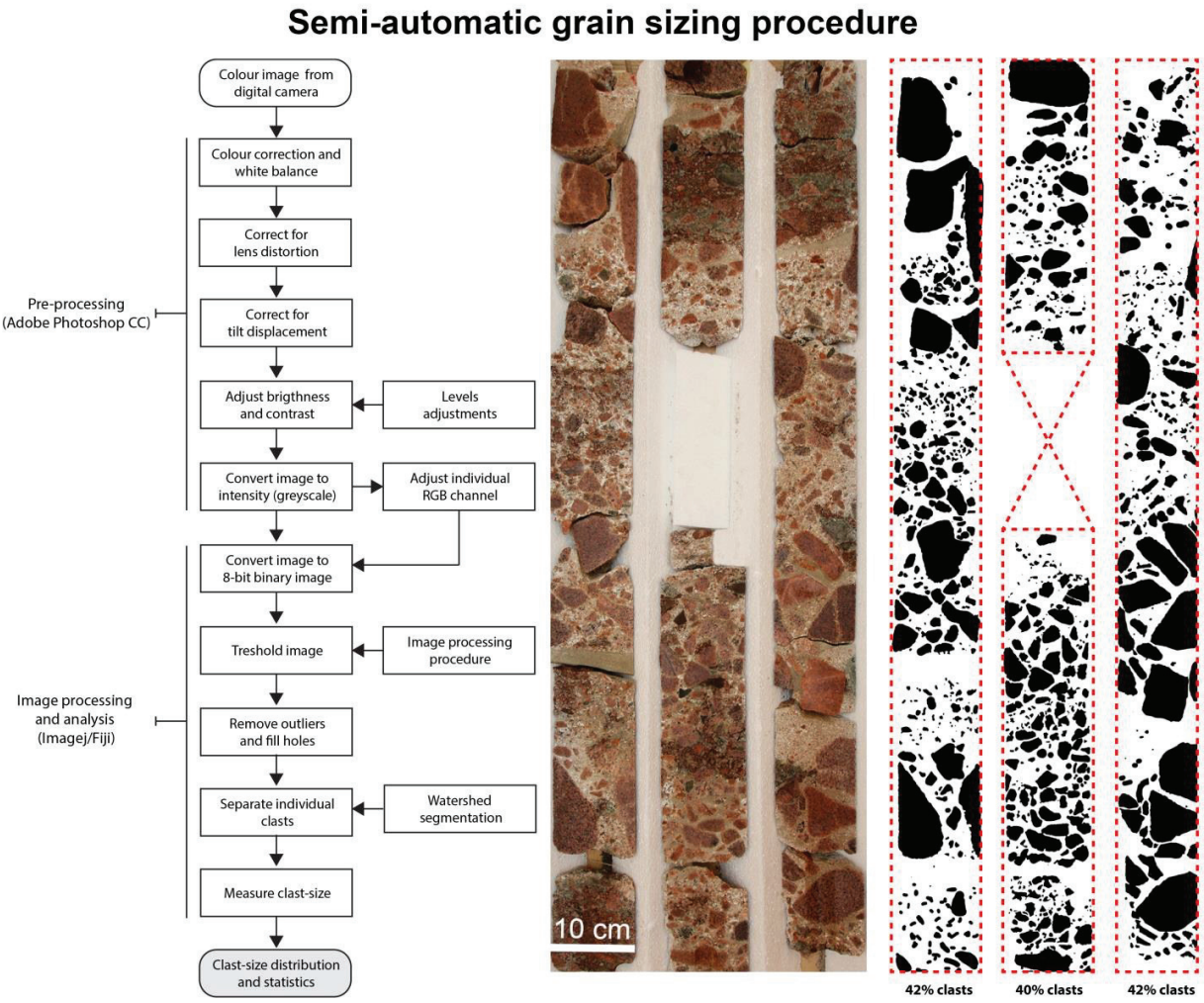

Figure 4 - The left part illustrate the stages required to extract clast -size data from a digital image. If necessary, steps to the right of the main workflow sequence are used to improve separation of the clasts. The centre picture is core photo and on the right is a binary image of the same core interval where clasts (black) are separated from the surrounding matrix (white). Matrix, which can be excellent reservoir, is everything smaller than granule size ($\phi > -1$).

1.4.2. High resolution X-ray computed tomography (micro-CT)

The high resolution micro-CT scan technique provides fairly accurate representation of the porosity values and geometries of the matrix in 3D. The technique was used to characterise the distribution of pores and pore-throats in 3D. This enables us to get detailed petrographical information in 3D across multiple scales (cm to nm) of these complex reservoir rocks. To characterise nano-scale micropores, additional sub-plugs (Fig. 5) were extracted from

appropriate locations in the samples and imaged at higher resolution, down to 1.65µm per voxel (pixel with x-y-z-coordinates). This approach gives more accurate representation of the porosity in the samples due to more easily resolved microporosity, which is mostly located in replacive and pore-lining and pore-filling clays, such as illite-smectite, illite, kaolinite, and chlorite.

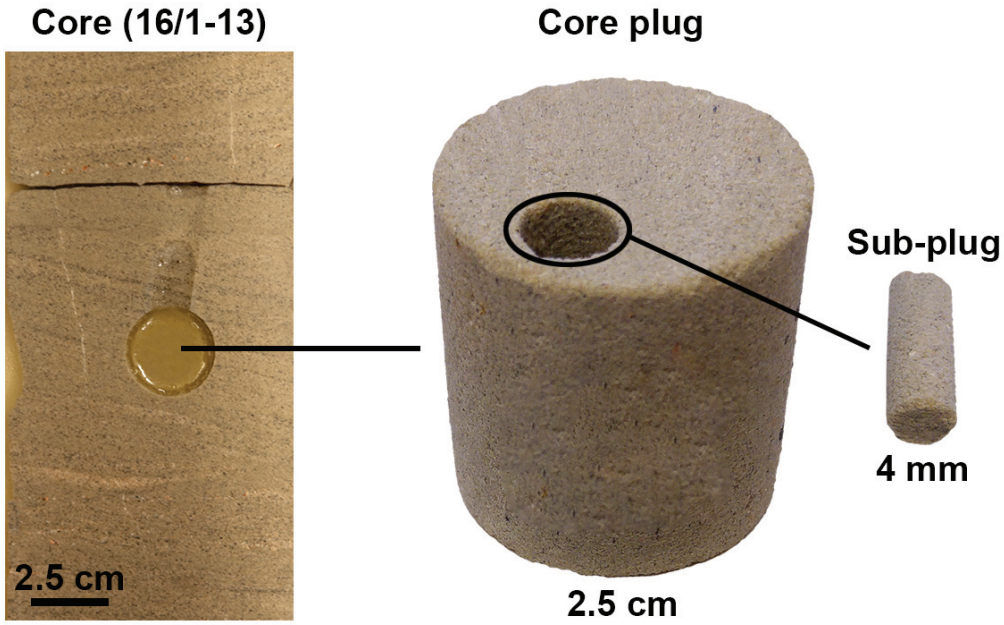

Figure 5 - The left image show example if core section with extracted core plug to the right. The additional sub-plug is extracted from the core plug in order to obtain higher resolution (~ 1.65 µm per voxel) of the rock.

Comprehensive petrological analysis, as mentioned above, was first done to select representative samples and to cover a wide range of observed porosities and permeabilities (Markussen et al., 2019). In order to resolve porosity distribution below image resolution, especially in the heterogeneous samples, the dry/wet method was applied. Here we first scanned samples in dry state, and then we saturated the samples with X-ray attenuation brine (1M NaI-H_2O solution) and scanned them again. With this approach the microporosity (below image resolution) could be located and quantified. This method not only resolves porosity distribution below image resolution, but also the pore throats and connectivities. The final multi-scale 3D models can be used to calculate various petrophysical parameters, e.g. porosity, absolute permeability, formation factor and capillary pressure.

2. Scientific framework

2.1. Alluvial fans

Alluvial fans are fan-shaped bodies of detrital sediment accumulations that develop along foot of mountain fronts, where confined flow channels emerge from a valley or mountain ravine (i.e. fan apex) into an area of reduced stream power (Fig. 6) (Bull, 1977; Harvey, 2011). The abrupt reduction in flow velocity and depth result in localised areas of enhanced deposition. This leads to progressive sediment deposition, forming alluvial fans radiating downslope (Blissenbach, 1954; Harvey, 2011). The angle of dip is relatively steep in the apical area, up to 10º (Blissenbach, 1954), decreasing progressively to the distal fan margins.

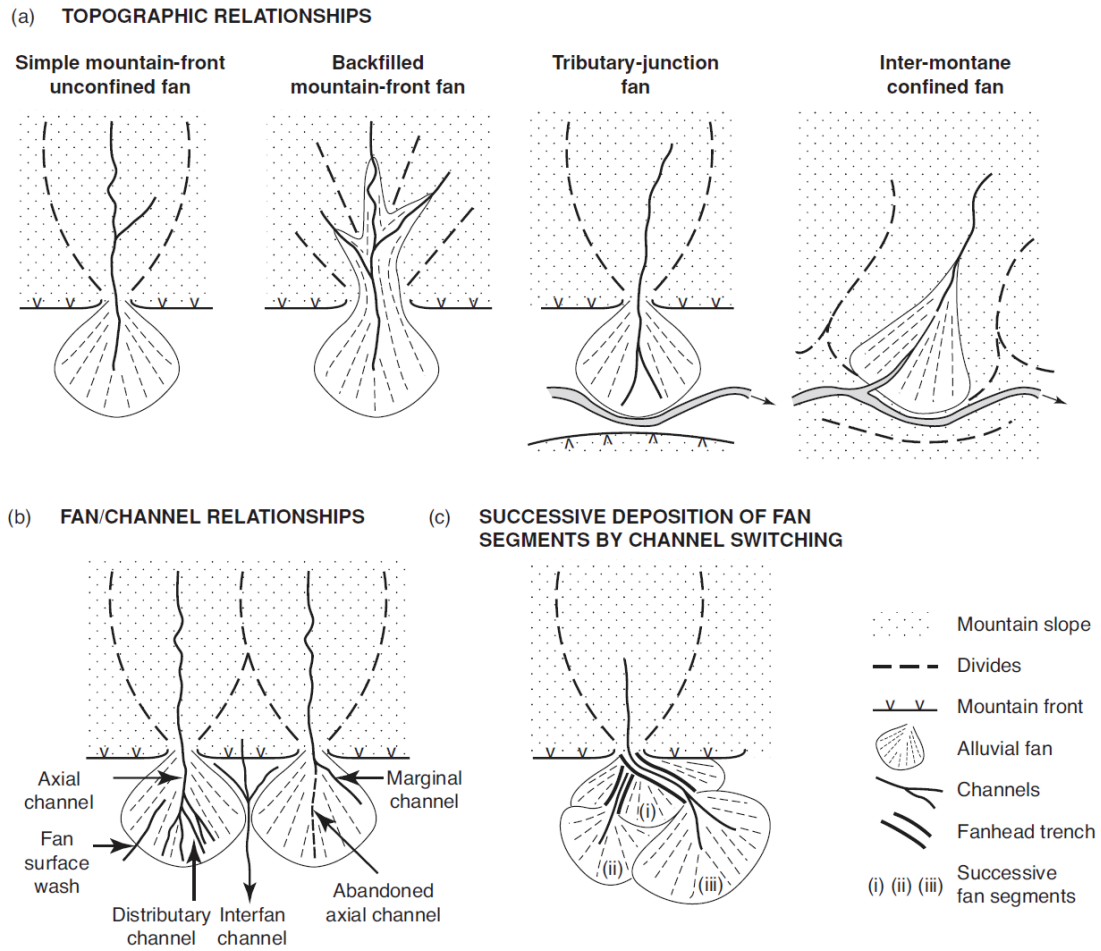

Figure 6 - (A) Topographic relationships; (B) Fan/channel relationships; (C) Channel switching. (From Harvey, 2011)

The alluvial fan sequences, i.e. geometries and grading pattern, plays an important role in basin analysis since they are sensitive to external influences, especially tectonism and climate. Understanding the architecture of alluvial fans will indicate the proximity to active faults and possibly the movement of these faults, as observed in the Edvard Grieg field. Tectonically controlled fans tend to result in prolonged accumulation of thick fans (Bull, 1977). Alluvial fan sediments will influence basin-scale migration, for example they can connect originally isolated distal reservoirs. Distally, fan sediments may intertwine with river, lake or aeolian deposits and produce continuous suites of deposits (Harvey, 2011). The relationship between fan radius and downslope decrease in grain size can give an indication of the dimensions of ancient fan deposits (North et al. 1989).

Alluvial fans are common in arid or semi-arid regions of the world, but they can also occur in humid, mountainous and Arctic regions (Bull, 1972; Harvey, 2011). Several factors influence the transport and deposition, such as climate (precipitation, weathering. transport), tectonic activity, source-area lithology and sediment type, and the slope gradient (Carryer, 1966; Kostaschuk et al., 1986). Sediment transport on alluvial fans can be split into two main categories, stream flow and mass flow processes (Bull, 1972, 1977; Kostaschuk et al., 1986; Harvey, 2011), generally reflecting the amount of water and sediment supply (Fig. 7). Both of these processes have been reflected in sediments of cores from wells in the Edvard Grieg field. The debris flow deposits (debrites) usually dominate in wells 16/1-10 and 16/1-13, while streamflow deposits are more common in the wells 16/1-18 and 16/1-23S. If there is reduced sediment supply and high water supply, the fluvial systems may downcut into the pre-existing successions. Debris flows may also dominate in some humid regions with heavy rainfall and source area rich in fine grained sediments (Collinson, 1996).

The slope and catchment size of alluvial fans can be reflected in the predominant depositional processes. In large catchment areas and gently sloping terrains, generally fluvial processes will dominate, while smaller catchment areas and steeper slopes tend to have more debris-flows and ephemeral streams (Blissenbach, 1954; Kostaschuk et al. 1986).

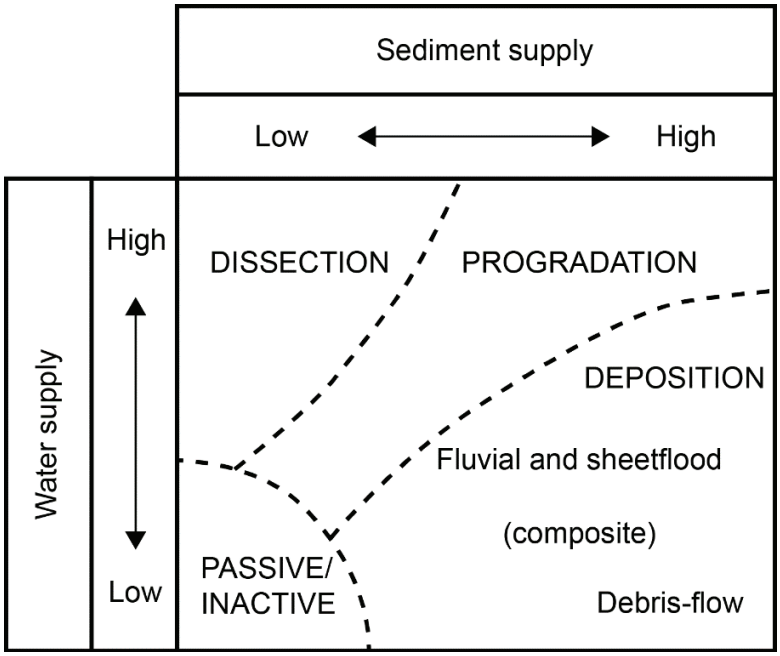

Figure 7 - Schematic model of influence of water and sediment supply on fan style. (From Harvey, 2011)

2.2. Alluvial fan deposits

Alluvial fans build up would normally require an inflow of sediments and fluids from the drainage area, with occasionally high discharge events (Blissenbach, 1954). The large volumes of sediments that need to be transported generally require very strong flow conditions (super critical flow), often the result of heavy precipitation or rapid snowmelt (Blair and McPherson, 2009; Harvey, 2011). Supercritical flow is more dominant in the steeper parts of the fans, with low water depth. This results in the deposition of coarse material in the upper section of the fan, while the finer material will be deposited down fan (Blair and McPherson, 1994).

Debrites generally display an unsorted to poorly sorted, massive to stratified texture, and graded to ungraded bedding. Such deposits are commonly associated with conglomerates in the Edvard Grieg field (see e.g. Mahmic et al., 2018). These conglomerate deposits can have little or no bedding, depending on the internal shear regime of the flow. Inverse grading may occur due to density differences during transport and so called kinematic sieving (Nemec and Steel, 1984). In general the thickness of debris flow deposits ranges from a few centimetres to several metres, and they are generally matrix-supported with some larger clast interaction due to internal

shearing (Pierson, 1981; Harvey, 2011). Furthermore, the bed thickness typically displays a positive, linear correlation with the clast size (Nemec and Steel, 1984). With increase in water content and improved fluidity, i.e. sediment/water mixtures with between 40 and 80% sediment by weight, the mixture behaves as a hyperconcentrated flow (Fig. 8) (Nemec and Steel, 1984; Pierson and Scott, 1985). These kinds of intermediate-type flows produce sheet-like beds, and are characterised by normally graded massive or graded massive to stratified beds, comparable to core interval 1906-1920 mDD from well 16/1-10 (Papers 1 and 2). On any alluvial fan the sediment/water ratio may differ during a rain storm and also vary downfan. Therefore, the catchment size, channel gradient, and sediments eroded during a storm, will control whether the fan is dominated by debris-flow or streamflow facies (Wells and Harvey, 1987).

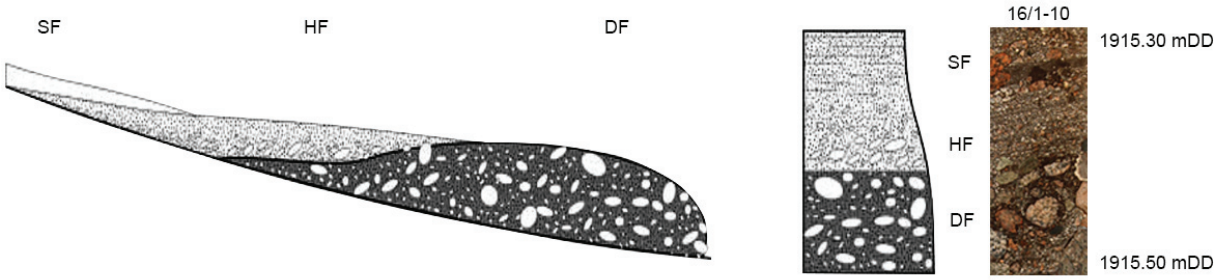

Figure 8 - Subaerial debris flow (DF), hyperconcentrated flow (HF), and streamflow (SF). Example of aggradation from subaerial debris flows, coarsest sediment in the flow head and progressively more finer-grained toward the tail, i.e. streamflow deposits. The core section on the most right is from well 16/1-10 (1915.50 mDD) showing the same aggradation pattern. (Modified from Sohn et al. 2002)

Conglomeratic braided-stream deposits are generally characterised by a clast-supported fabric (Rust, 1978; Nemec and Steel, 1984). The textural maturity of the gravel deposits partly reflects the distance from the source and degree of reworking during transport (Fig. 9). Primary ephemeral (flashy) flood-transported alluvial fan stream deposits tend to retain most of the original textural characteristics and show least textural maturity (Nemec and Steel, 1984). The deposits can often show evidence of tractional transport, such as stratification, imbricated clasts and basal scouring.

The streamflow deposits are often the result of suspension, saltation and traction transport by flowing water in either channellised or non-channellised flow. The deposits are normally well

stratified, contain small amount of clay matrix-, are clast -supported and often imbricated relative to the flow direction (Bull, 1972).

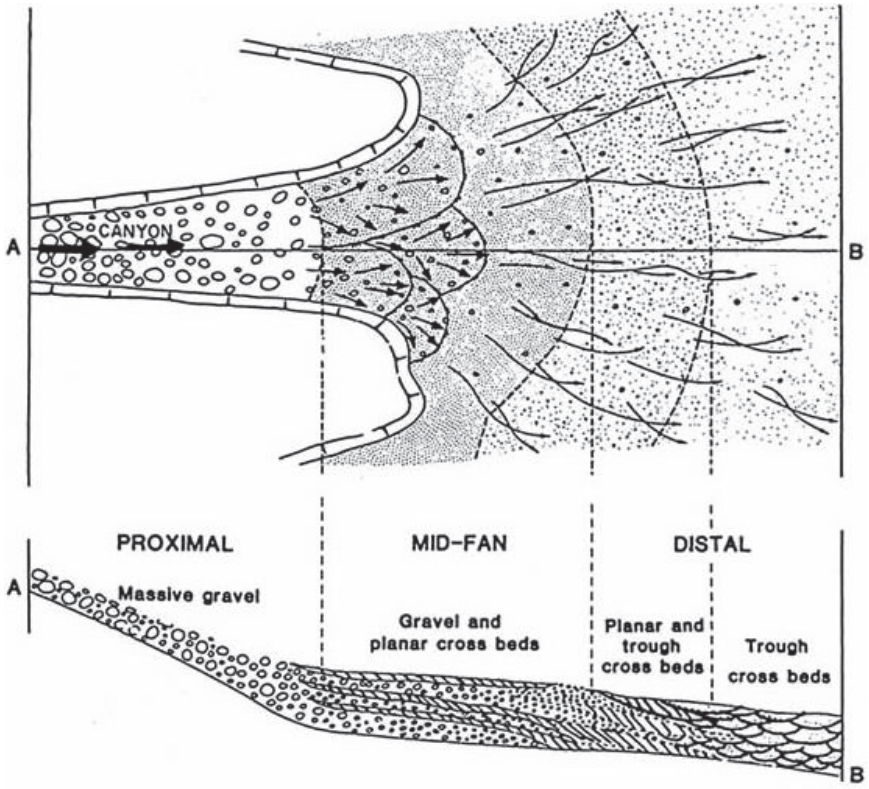

Figure 9 - Idealised cross-section and plan view through a streamflow fan system. (From Steel and Gloppen, 1980)

2.3. Diagenesis and reservoir quality

2.3.1. Early diagenesis

Early diagenesis include postdepositional processes that take place near the surface or in shallow subsurface up to 60° to 70°C, to about 2 km burial depth (Morad et al., 2000) (Fig. 10). The chemistry of the original pore water has a major control on the reactions during this stage (Bjørlykke, 1998). During the mechanical compaction regime, the overburden stresses causes reorientation and breaking of the grains, reduce porosity and bulk volume of the sediments, and result in increased bulk density. The mechanical compaction is normally greater in well sorted fine-grained sand (Bjørlykke, 2014), e.g. aeolian deposits of Edvard Grieg field, than coarse-

grained sand, but due to larger surface area in the fine-grained sand the quartz cement precipitation may be greater during late diagenesis.

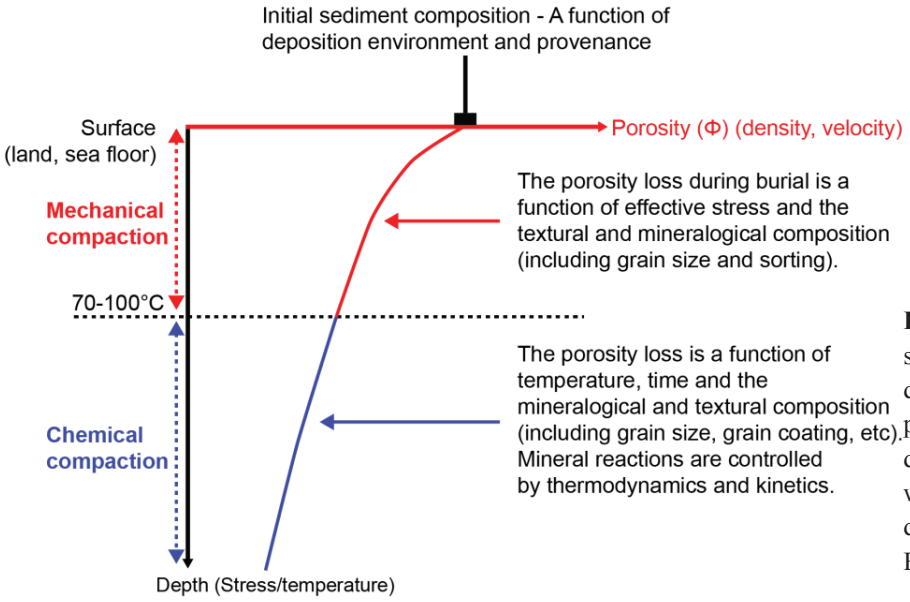

Figure 10 - Compaction of sediments as a function of depositional environment and provenance. Porosity decreases with depth, whereas velocity and bulk density increase. (From Bjørlykke, 2014)

The amount and mineral composition of pore-filling clay minerals from weathering and diagenetic alteration, may reduce porosity and permeability significantly, and is particularly important (Velde and Meunier, 2008) as they may infiltrate previously deposited sediments. Such clays can be introduced in the fabric of siliciclastic sediments by e.g. later mechanical infiltration. An early grain coating by detrital clays may have a positive effect in preservation of porosity with deep burial (e.g. Heald and Larese, 1974; Thomson, 1979; Pittman et al., 1992; Ehrenberg, 1993; Bloch et al., 2002; Anjos et al., 2003; Taylor et al., 2004; Ajdukiewicz et al., 2010; Taylor et al., 2010; Busch et al., 2017). These authors reported significant increase in quartz cementation in sandstones lacking or having poorly developed grain coating. One of the important grain-coating clays is chlorite because it can form continuous layers between the framework grains and pore space, as frequently observed in the Edvard Grieg deposits. Detrital, mechanically infiltrated clays, are normally less continuous than authigenic clay coatings, consequently less effective in inhibiting quartz cementation (Wilson and Pittman, 1977; Bloch et al., 2002). Authigenic clay coatings may partially form from early mechanically infiltrated precursor clay, e.g. smectite, which also may develop during weathering/early diagenesis under warm, arid to semi-arid conditions (Hillier, 1994; Hillier et al., 1996; Morad et al., 2000; Worden and Morad, 2003).

Precipitation of early diagenetic pore-filling kaolinite requires low K^+/H^+ ratios which are generally found in fresh or brackish water (Hancock and Taylor, 1978; Bjørlykke, 1998; 2014). Liberated ions such as Al and Si from K-feldspar, plagioclase, and mica dissolution due to flow of meteoric water, may result in precipitation of kaolinite (Eq. 1 to 3). For these reactions (1 and 2) to occur it is therefore vital that the reaction products K^+ and Na^+ are removed from the system, otherwise the reaction will stop. The leaching of K-feldspar, plagioclase and micas will produce secondary porosity and an equal amounts of kaolinite. In the Edvard Grieg deposits the kaolinite content is often highest in sandstone lithologies with increased porosity and permeability (Mahmic et al., 2018). The leaching process is more intense in humid climates compared to climates with net evaporation. In warm and dry climates the leaching of feldspar is limited to periods of heavy rainfall, resulting usually in less frequent kaolinite precipitation (Chamley, 1989).

$$2K(Na)AlSi_3O_8 + 2H^+ + 9H_2O \leftrightarrow Al_2Si_2O_5(OH)_4 + 4H_4SiO_4 + 2K^+(2Na^+)$$

K-Feldspar Kaolinite Dissolved silica [1]

$$2KAl_3Si_3O_{10}(OH)_2 + 2H^+ + 9H_2O \leftrightarrow Al_2Si_2O_5(OH)_4 + 4H_4SiO_4 + 2K^+(2Na^+) + 2K^+(2Na^+)$$

Mica Kaolinite Dissolved silica [2]

After Bjørlykke et al. (1992).

$$2NaAlSi_3O_8 + 9H_2O + 2H^+ \leftrightarrow Al_2Si_2O_5(OH)^4 + 4H_4SiO_4 + 2Na^+$$

Plagioclase Kaolinite Dissolved silica [3]

After Blum (1994).

Early diagenetic carbonate cements in continental environments (calcrete, dolocrete) may form in either in vadose (pedogenic - soil formation) or phreatic (groundwater) zone (Wright and Tucker, 1991). The Ca^{2+} and CO_3^{2-} sources for calcium carbonate in a warm and dry climate may be introduced by wind or water from the adjacent carbonate-rich playa lakes (Lattman, 1973). The distribution of carbonates in alluvial fans systems can also be explained based on the hydrological pattern, as shown in Figure 11 (Nickel, 1985).

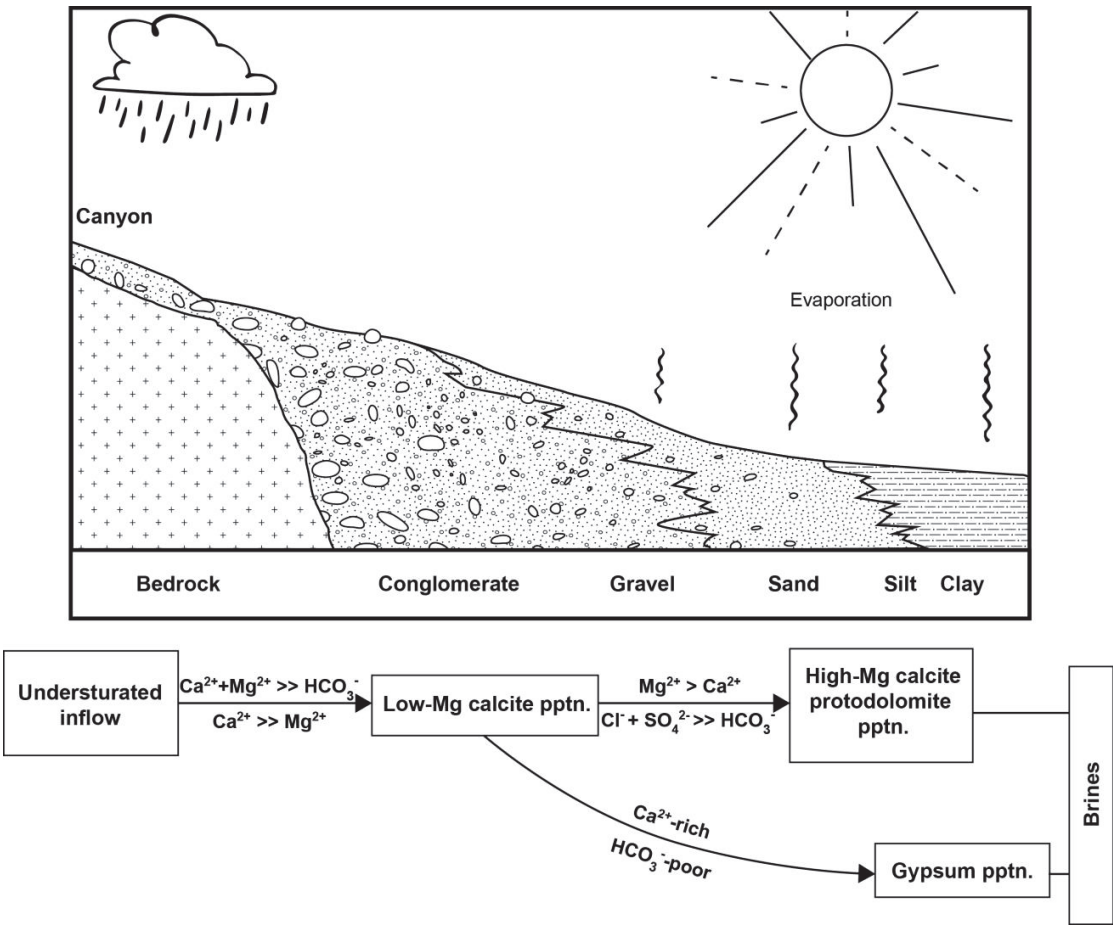

Figure 11 - Conceptual model of alluvial-fan zonation with the evolution of carbonate-sulphate brines from proximal to distal areas in an alluvial-fan system. (Modified from Nickel, 1985)

The net evaporation of the near-surface groundwater in a warm and dry climate may lead to precipitation of authigenic Fe-oxide (e.g. hematite) (Ross, 1969; Acker and Bricker, 1992). These sediments typically have red staining and are commonly observed in the studied Edvard Grieg deposits, mostly in intervals with abundant detrital clay.

2.3.2. Late diagenesis

Late diagenesis normally corresponds to the chemical compaction phase, e.g. clay mineral transformation and quartz cementation, and usually occurs below depths ≥ 2 km burial depth at temperatures ≥ 70°C (Morad et al., 2000). During late diagenesis the system is generally isolated from the surface meteoric water and processes directly related to the surface. Kinetics, compared to thermodynamics, are generally the important controlling factor for the chemical processes

during late diagenesis (Morad et al., 2000). At burial temperatures above 60-90ºC the precipitation rates of quartz cement can be significant and strengthen the rock, typically close to the transition from mechanical to chemical compaction (Bjørlykke and Egeberg, 1993; Lander and Walderhaug, 1999; Wilkinson and Haszeldine, 2002; Bjørlykke, 2014).

Early diagenesis and precipitation of early authigenic clays (e.g. kaolinite) at shallow depths in the pore space may have both positive and negative impact on the reservoir quality (Bjørlykke, 2014); 1) Early pore-filling cements, e.g. carbonate cements and authigenic clay minerals, will normally reduce the porosity and permeability in the system, but 2) the presence of early diagenetic clay coatings, e.g. chlorite coating, may inhibit late quartz cementation. The chlorite coating observed in the Edvard Grieg deposits played such an important role.

In sedimentary basins, available potassium (e.g. K-feldspar and mica) and authigenic clay minerals (e.g. kaolinite) are important reactants for high temperature (>120°C) diagenetic illite, which can to varying extent choke pores and pore-throats (Hower et al., 1976; Pearson and Small, 1988; Peltonen et al., 2008; Lander and Bonnell, 2010). Permeability-reducing illite may also form (from about 60-80°C) from early diagenetic smectite, which originally developed under warm and arid climatic conditions (Hillier, 1994; Hillier et al., 1996; Morad et al., 2000; Worden and Morad, 2003; Nadeau et al., 2005). The estimated burial temperatures for the studied Edvard Grieg deposits range between 75 and 85°C, with an average geothermal gradient of 40.5˚C. This value fits well with observed geothermal gradients in the North Sea, ranging from 30-40˚C (Bjørlykke et al., 1995).

2.3.3. Diagenesis control on reservoir quality

The diagenesis and reservoir quality evolution in siliciclastic sediments can be very complex. Mineralogical composition, fluid chemistry, textural characteristics (e.g. pore geometry, particle size and shape), tectonic setting, depositional facies, environmental factors such as increasing temperature, vertical effective stress (mechanical compaction) and chemical conditions can significantly impact the resulting reservoir porosity and permeability (Taylor et al., 2010). Porosity and permeability variations in siliciclastic sediments are initially controlled by sedimentary conditions at the time of deposition and further altered during early and late diagenesis (Bjørlykke, 1998; Morad et al., 2000). The initial porosity correlates closely to the

depositional grain size and sorting of the sediments, where poorly sorted sand has much lower initial porosity than well sorted sand, but shows less porosity loss during mechanical compaction (Beard and Weyl, 1973; Fawad et al., 2011; Bjørlykke, 2014).

Grain size, sorting, shape, and matrix content determine the intergranular volume (IGV) of the sediments (Ajdukiewicz and Lander, 2010; Nguyen et al., 2013). IGV is the sum of intergranular pore space, intergranular cement and depositional matrix. The reduction of IGV by mechanical compaction in loose sand is limited to 26%, which represents the arrangement of an ideal sphere packing (Houseknecht, 1987). Further reduction in IGV is caused by chemical compaction, i.e. grain dissolution at grain contacts. In the studied Edvard Grieg deposits the original porosity loss, i.e. reduction of IGV, is usually dominated by mechanical compaction in all the main lithology units. High IGV values in the many fluvial and aeolian sandstone deposits of the Edvard Grieg field reflect early carbonate cement, which reduced the effect of mechanical compaction.

3. Summary of papers

3.1. Paper 1

Diagenetic influence on reservoir quality evolution, examples from Triassic conglomerates/ arenites in the Edvard Grieg field, Norwegian North Sea.

Mahmic, O., Dypvik, H., and Hammer, E. (2018). Marine and Petroleum Geology, 93, 247-271.

The overall objective of Paper 1 was to evaluate the various diagenetic events and phases, such as dissolution of unstable grains and precipitation of clay minerals and cements, in the highly heterogeneous reservoir successions in the Edvard Grieg field. Paper 1 discuss how these influenced the development of reservoir quality through time. Several detailed mineralogical and sedimentological analyses have been carried out on these rocks; including sedimentological core logging, and petrographical analyses such as optical mineralogy, X-ray powder diffraction (XRD) and scanning electron microscope (SEM). Quantitative diagenetic analysis was

undertaken to provide data increasing understanding of diagenesis and P&P. This was done by quantifying the main diagenetic phases and reconstructing the initial texture and mineralogy based on the mineral maps. Furthermore, the diagenetic control of reservoir quality as related to the depositional facies.

The results show that depositional facies had a profound influence on the diagenetic development, both during early and late diagenesis. The deposits in the Edvard Grieg field are dominated by matrix- and clast-supported conglomerates and sandstones deposited in a warm and dry climatic conditions. The conglomerates of the deeper studied core sections represents alluvial fan deposits and consists of highly immature, poorly sorted, very fine to coarse gravels with either silty to sandy matrix. The conglomerates generally contain high amounts of early diagenetic authigenic pore-filling clays and cements, which combined with the mentioned characteristics (poor sorting) result in an overall low reservoir quality. The stratigraphically overlying sandstone facies, of fluvial and aeolian affinity, show improved reservoir quality compared to the conglomerates reflecting better sorting, reduced cementation and higher intergranular porosities.

The early diagenesis of the Edvard Grieg deposits was characterised by Fe-oxide grain-coating, dissolution of unstable minerals, e.g. feldspars, precipitation of microcrystalline and poikilotopic carbonates (dolomite and calcite), K-feldspar overgrowths and kaolinite precipitation. The late diagenesis was marked by precipitation of quartz, albitisation, and recrystallisation of illite and chlorite probably from early dioctahedral and trioctahedral smectite.

3.2. Paper 2

3D characterization of porosity and authigenic cementation in Triassic conglomerates/ arenites in the Edvard Grieg field using 3D micro-CT imaging.

Markussen, Ø., Dypvik, H., Hammer, E., Long, H., and Hammer, Ø. (2019). Marine and Petroleum Geology, 99, 265.281.

This paper presents a detailed 3D investigation of the distribution and texture of pores and pore-throats in arenites and highly heterogeneous conglomerates. To achieve this, we used multiscale

high-resolution 3D micro-CT scan techniques to capture and quantify macro- and micropores and their connectivity in 3D.

Since most of the porosity in the conglomeratic facies are on the macroscale (i.e. below image resolution), and generally located in the various authigenic clay minerals, the information on the possible overall processes was usually limited by the resolution of the 3D scans. In order to resolve porosity below image resolution, we applied dry/wet method and extracted sub-plugs and scanned these at higher resolution.

The study gave improved characterisation of microporosity (below image resolution), as well as of macroporosity (above image resolution) and their connectivity and distribution when using dry/wet method. This was especially evident in the heterogeneous and complex conglomeratic matrix. The use of high-resolution 2D SEM-EDS images of thin sections (from core plugs and sub-plugs) and accurate aligning them with the corresponding region in the 3D micro-CT data set, provided quality control and further insight of the nanoscale pores.

The clay-rich conglomerate with both detrital and authigenic components, carries a significant fraction of the porosity in the clay phases (i.e. below image resolution). The macroporosity is usually poorly connected and unevenly distributed. This results in overall low permeability. In the sandstone lithologies, especially the aeolian sandstones, the P&P increase when pores are well connected. The distribution of early diagenetic carbonate cement in the samples was also investigated. It shows that carbonate cement has an negative effect on the pore connectivity (major fluid pathways) and fluid flow capacity. The overall reservoir properties (P&P) improve when the carbonate cement is removed from the generated 3D digital rock model.

3.3. Paper 3 (Submitted)

Basement clast distribution and sedimentary facies analysis of alluvial fan conglomerates, Edvard Grieg field, North Sea.

Mahmic, O., Dypvik, H., Hammer, E. (Submittet) Marine and Petroleum Geology.

The purpose of this study has been to further investigate the various sedimentary facies (seven in total) and depositional environment in more detail by quantifying the type and size of the

basement clasts of the Skagerrak Formation in the Edvard Grieg field. The studied cores from the Edvard Grieg field suggest deposition by mass flows/debris flows, streamflows, ephemeral braided rivers and lakes in an alluvial fan system under a warm, arid to semi-arid climate.

The systematically collected clast data provide additional information of changes in provenance, weathering degree of the clasts, matrix/clast relations, and evolution of the alluvial fan system through time. The clast size data was gathered using a refined semi-automatic image analysis method from several other studies of automatic grain-size distribution (McEwan et al., 2000; Butler et al., 2001; Reid et al., 2001; Sime and Ferguson, 2003).

The basement clasts are mostly granitic in nature and can be classified as: granodiorite, monzogranite and quartz monzodiorite, derived from the local basement exposed to the south, east and north. The granitoid clasts are characterised by a variable amount of weathering, usually consisting of a selective loss of feldspars. Clasts with a weathering rim are also common, but in decreasing abundance upwards through the studied cores (abrasion due to redeposition).

The maximum and average clast size is usually gravel grade, but boulder size (>0.5 m) have been observed locally in some intervals. The clast size is largest in the two wells 16/1-10 and 16/1-13, located proximal to the northern fault system, and reduced in the more distal wells 16/1-18 and 16/1-23S. Furthermore, the results indicate an overall retreating and fining upwards alluvial fan system observed in wells 16/1-10 and 16/1-13, moving from coarse grained conglomerates in the lower cores to finer grained sandstones in the upper cores from wells 16/1-10 and 16/1-13. This trend is not observed in wells 16/1-18 and 16/1-23S where conglomeratic successions dominate the cores.

4. Concluding remarks

The overall aim of this study was to better predict reservoir characterisation and understand the impact of petrology, mineralogy and diagenesis on reservoir quality evolution in the Edvard Grieg field. Different methodologies and scales (nano to metre) have been combined to predict reservoir quality, i.e. porosity and permeability, as a function of initial sediment composition and depositional setting, and conditions that prevailed during postdepositional processes, i.e.

diagenesis. The main factors that influence the course of diagenesis are sedimentary factors, e.g. particle size, fluid content and mineral composition, and external factors such as temperature, effective pressure and chemical conditions (pore-water).

The abundance of coarse-grained debrites, high energy sheetflow deposits, and streamflow deposits in the cores of Skagerrak Formation are all attributed to an alluvial fan setting. The main lithologies that dominate in the Edvard Grieg field are silty and sandy conglomerates, interbedded thin sandstone beds, and gravely sandstones. Large-scale cross-stratified sandstones are interpreted to be aeolian dunes deposited under arid to semi-arid climatic conditions. These different lithologies collectively show various levels of internal interaction, e.g. intermixing of fluvial and aeolian processes on an alluvial fan. Increase in chemical dissolution and reworking in these sandstones is reflected in an overall reduction of plagioclase content compared to the conglomerate matrix. Subordinate thin mudstone horizons are interpreted as having been deposited in ephemeral ponds and lakes.

From the studied cores of the Edvard Grieg field, various diagenetic phases, such as dissolution of unstable grains and precipitation of clay and carbonate cement, have strongly influenced the reservoir quality through time, summarised in Figure. 12. Most of the reservoir reduction is associated with poor sorting in the conglomerate matrix and authigenic pore-filling/pore-lining of illite-smectite, illite, chlorite, smectite and kaolinite clays. Reservoir quality of the conglomerate matrix can be assessed as low to moderate (occasionally good), while the reservoir quality is comparably better in the sandstone lithologies. The aeolian facies display excellent properties related to reduced authigenic cements and better sorting. Further dating of e.g. carbonate cement and quartz overgrowths is recommended to better understand the absolute timing of these cement phases.

An increase in sandstone-dominated alluvial fan deposits in the upper most cores from the two wells 16/1-10 and 16/1-13 is reflected in an increase in reservoir quality compared to the underlying conglomeratic successions.

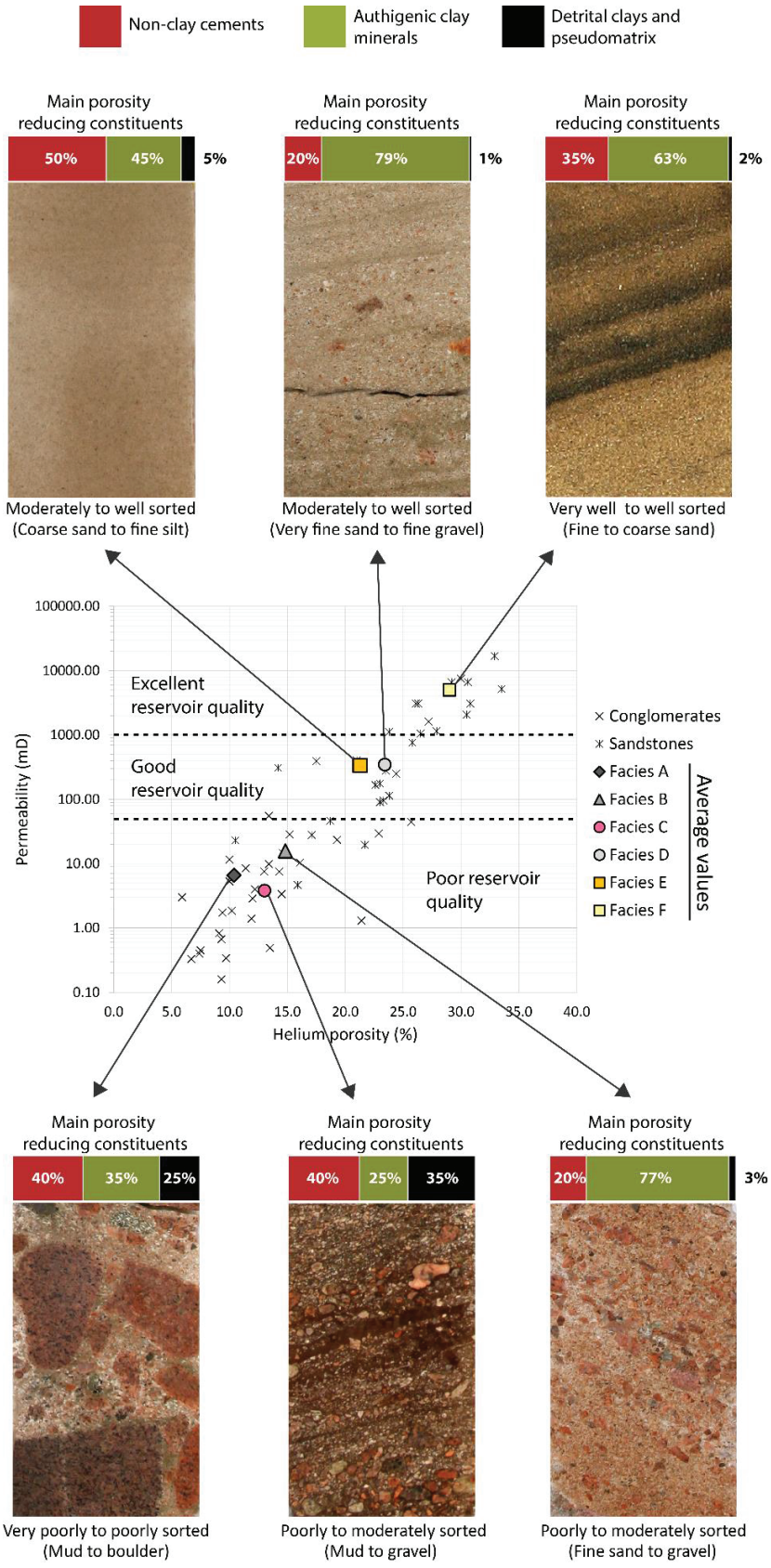

Figure 12 - Laboratory porosity and permeability (P&P) data plot for selected conglomerates and sandstones samples in the Edvard Grieg field. Average P&P data for each facies is also presented in the same plot. **Facies A:** Texturally heterogeneous, structureless conglomerates; **Facies B**: Sand-rich conglomerate; **Facies C:** Planar stratified conglomerate; **Facies D:** Gravelly sandstone; **Facies E:** Planar laminated sandstone; **Facies F:** Fine to medium cross-bedded quartzitic sandstone. The graph above each core photo represents the modal data of the main porosity reducing constituents: Detrital clay and pseudomatrix, non-clay cements (calcite, dolomite and feldspar overgrowths), authigenic clay minerals (coating- and pore filling-clays, kaolinite and Fe-oxides).

References

Acker, J. G. and Bricker, O. P. (1992). The influence of pH on biotite dissolution and alteration kinetics at low temperature. Geochimica et Cosmochimica Acta, 56(8), 3073-3092.

Ajdukiewicz, J. M., and Lander, R. H. (2010). Sandstone reservoir quality prediction: The state of the art. AAPG bulletin, 94(8), 1083-1091.

Anjos, S. M. C., L. F. De Ros, and C. M. A. Silva, 2003, Chlorite authigenesis and porosity preservation in the Upper Cretaceous marine sandstones of the Santos Basin, offshore eastern Brazil, in R. H. Worden and S. Morad, eds., Clay mineral cements in sandstones: International Association of Sedimentologists Special Publication 34, p. 291-316.

Bartholomew, I., Peters, J. and Powell, C. (1993). Regional structural evolution of the North Sea: oblique slip and the reactivation of basement lineaments. Geological Society, London, Petroleum Geology Conference series. Geological Society of London, 1109-1122.

Barton, P., and Wood, R. (1984). Tectonic evolution of the North Sea basin: crustal stretching and subsidence. Geophysical Journal International, 79(3), 987-1022.

Beard, D. C. and Weyl, P. K. (1973). Influence of texture on porosity and permeability of unconsolidated sand. In Diagenesis of Sandstones. AAPG Bulletin, 57(2), 349-369.

Bjørlykke, K., T. Nedkvikne, M. Ramm, and G. C. Saigal, (1992). Diagenetic processes in the Brent Group (middle Jurassic) reservoirs of the North Sea; an overviw, in A. C. Morton, R. S. Haszeldine, M. R. Giles, and S. Brown, eds., Geology of the Brent Group: Special Publication 61: London, Geological Society, p. 263-289.

Bjørlykke, K., and P. K. Egeberg, (1993). Quartz cementation in sedimentary basins: AAPG Bulletin, v. 77, p. 1538-1548.

Bjørlykke, K., Aagaard, P., Egeberg, P. K., and Simmons, S. P. (1995). Geochemical constraints from formation water analyses from the North Sea and the Gulf Coast Basins on quartz, feldspar and illite precipitation in reservoir rocks. The Geological Society, London, Special Publications, 86(1), 33-50.

Bjørlykke, K. (1998). Clay mineral diagenesis in sedimentary basins—a key to the prediction of rock properties. Examples from the North Sea Basin. Clay Minerals, 33(1), 15-34.

Bjørlykke, K. (2014). Relationships between depositional environments, burial history and rock properties. Some principal aspects of diagenetic process in sedimentary basins. Sedimentary Geology, 301, 1-14.

Blair, T., McPherson,J., (1994). Alluvial Fans and Their Natural Distinction From Rivers Based on GeoMorphology, Hydraulic Processes, Sedimentary Processes, and Facies Assemblages:Journal of Sedimentary Research, V. A64, No. 3, P. 450-489.

Blair, T., McPherson, (2009). Processes and Forms of Alluvial Fans, Geomorphology of Desert Environments, Chapter 14, 2nd edition.

Blissenbach, E. (1954). Geology of alluvial fans in semiarid regions. Geological Society of America Bulletin, 65(2), 175-190.

Blum, A.E., (1994). Feldspars in weathering. In: Parsons, I. (Ed.), Feldspars and their reactions. Springer, pp. 595 - 630.

Bloch, S., R. H. Lander, and L. M. Bonnell, (2002). Anomalously high porosity and permeability in deeply buried sandstone reservoirs: Origin and predictability: AAPG Bulletin, v. 86, p. 301-328.

Bull, W. B. (1972). Recognition of alluvial fan deposits in the stratigraphic record.

Bull, W.B. (1977). The alluvial fan environment. Progress in Physical Geography, 1, 222-270.

Busch, B., Hilgers, C., Gronen, L., and Adelmann, D. (2017). Cementation and structural diagenesis of fluvio-aeolian Rotliegend sandstones, northern England. Journal of the Geological Society, jgs2016-122.

Butler, J. B., Lane, S. N., and Chandler, J. H., (2001), Automated extraction of grain-size data from gravel surfaces using digital image processing: Journal of Hydraulic Research, v. 39, no. 4, p. 1-11.

Bøe, A. E. (2014). Utfordreren. Lundin Norways første ti år på norsk sokkel 2004 - 2014, Stenersens forl.

Carryer, S. J. (1966). A note on the formation of alluvial fans. New Zealand Journal of Geology and Geophysics, 9(1-2), 91-94.

Chamley, H. (1989). Clay Sedimentology. Springer-Verlag Berlin Heidelberg, 623.

Christiansson, P., Faleide, J. and Berge, A. (2000). Crustal structure in the northern North Sea: an integrated geophysical study. SPECIAL PUBLICATION-GEOLOGICAL SOCIETY OF LONDON, 167**,** 15-40.

Collinson, J. D. (1996). Alluvial sediments. Sedimentary environments: processes, facies and stratigraphy, 3, 37-82.

Ehrenberg, S. N., (1993). Preservation of anomalously high porosity in deeply buried sandstones by grain-coating chlorite: Examples from the Norwegian continental shelf: AAPG Bulletin, v. 77, p. 1260-1286.

Faleide, J. I. and Berge, A. M. (2000). The geometries and deep structure of the northern North Sea rift system. Dynamics of the Norwegian Margin, 167**,** 41.

Faleide, J. I., Bjørlykke, K., and Gabrielsen, R. H. (2015). Geology of the Norwegian continental shelf. In Petroleum Geoscience (pp. 603-637). Springer, Berlin, Heidelberg.

Fawad, M., Mondol, N.H., Jahren, J., Bjørlykke, K., (2011). Mechanical compaction and ultrasonic velocity of sands with different texture and mineralogical composition. Geophysical Prospecting 59, 697-720.

Frost, R., Fitch, F. and Miller, J. (1981). The age and nature of the crystalline basement of the North Sea Basin. Petroleum geology of the continental shelf of North-West europe**,** 43-57.

Færseth, R. (1996). Interaction of Permo-Triassic and Jurassic extensional fault-blocks during the development of the northern North Sea. Journal of the Geological Society, 153**,** 931-944.

Færseth, R. B., and Ravnås, R. (1998). Evolution of the Oseberg fault-block in context of the northern North Sea structural framework. Marine and Petroleum Geology, 15(5), 467-490.

Glennie, K. (2009). Lower Permian—Rotliegend. Petroleum Geology of the North Sea: Basic Concepts and Recent Advances, Fourth Edition**,** 137-173.

Goldsmith, P. J., Hudson, G. and Van Veen, P. (2003). Triassic. (eds.): The Millennium Atlas: Petroleum Geology of the Central and Northern North Sea. Geological Society, London, 105-127.

Gowers, M. B. and Sæbøe, A. (1985). On the structural evolution of the Central Trough in the Norwegian and Danish sectors of the North Sea: Marine and Petroleum Geology, v.2, p. 298-318.

Gregersen, U., Michelsen, O. and Sørensen, J. C. (1997). Stratigraphy and facies distribution of the Utsira Formation and the Pliocene sequences in the northern North Sea. Marine and Petroleum geology, 14**,** 893-914.

Hancock, N. J. and Taylor, A. M. (1978). Clay mineral diagenesis and oil migration in the Middle Jurassic Brent Sand Formation. Journal of the Geological Society, 135(1), 69-72.

Harvey, A. (2011). Dryland alluvial fans. Arid Zone Geomorphology: Process, Form and Change in Drylands, Third Edition, 333-371.

Heald, M. T., and R. E., Larese, (1974). Influence of coatings on quartz cementation: Journal of Sedimentary Petrology, v. 44, p. 1269-1274.

Heeremans, M. and Faleide, J. I. (2004). Late Carboniferous-Permian tectonics and magmatic activity in the Skagerrak, Kattegat and the North Sea. SPECIAL PUBLICATION-GEOLOGICAL SOCIETY OF LONDON, 223**,** 157-176.

Hillier, S. (1994). Pore-lining chlorites in siliciclastic reservoir sandstones: electron microprobe, SEM and XRD data, and implications for their origin. Clay Minerals, 29(4), 665-680.

Hillier, S., Fallick, A. E. and Matter, A. (1996). Origin of pore-lining chlorite in the aeolian Rotliegend of northern Germany: Clay Minerals, 31, 153-171.

Houseknecht, D. W. 1987. Assessing the relative importance of compaction processes and cementation to reduction of porosity in sandstones. AAPG Bulletin, 71(6), 633-642.

Hower, J., E. V. Eslinger, M. E. Hower, and E. A. Perry, (1976). Mechanism of burial metamorphism of argillaceous sediment: 1. Mineralogical and chemical evidence: Geological Society of America Bulletin, v. 87, p. 725-737.

Isaksen, G. H. and Ledje, K. H. I. (2001). Source rock quality and hydrocarbon migration pathways within the greater Utsira High area, Viking Graben, Norwegian North Sea. AAPG bulletin, 85**,** 0861-0884.

Jackson, C. A., Kane, K. E. and Larsen, E. (2010). Structural evolution of minibasins on the Utsira High, northern North Sea; implications for Jurassic sediment dispersal and reservoir distribution. Petroleum Geoscience, 16**,** 105-120.

Kostaschuk, R. A., MacDonald, G. M., and Putnam, P. E. (1986). Depositional process and alluvial fan-drainage basin morphometric relationships near Banff, Alberta, Canada. Earth Surface Processes and Landforms, 11(5), 471-484.

Lander, R. H., and Bonnell, L. M. (2010). A model for fibrous illite nucleation and growth in sandstones. AAPG bulletin, 94(8), 1161-1187.

Lander, R. H., and A. Walderhaug, (1999). Reservoir quality prediction through simulation of sandstone compaction and quartz cementation: AAPG Bulletin, v. 83, p. 433-449.

Laursen, I., Fugelli, E. and Lervik, K. S. (1995). Sequence stratigraphic framework of the Paleocene and Eocene successions, block 16/1, Norwegian North Sea. In: R.J. STEEL, V. L. F. E. P. J. and MATHIEU, C. (eds.) Norwegian Petroleum Society Special Publications. Elsevier.

Lattman, L. H. (1973). Calcium carbonate cementation of alluvial fans in southern Nevada. Geological Society of America Bulletin, 84(9), 3013-3028.

Lie, J. E., and Nilsen, E. (2016). Benchmarking of seismic broadband acquisition and processing: A unique comparison of technologies on the Edvard Grieg and the Johan Sverdrup fields, offshore Norway. In SEG Technical Program Expanded Abstracts 2016 (pp. 5109-5112). Society of Exploration Geophysicists.

Lundin, (2014). www.lundin-petroleum.com/eng/Development_EdvardGrieg.php [Accessed on September, 2014].

Mahmic, O., Dypvik, H., and Hammer, E. (2018). Diagenetic influence on reservoir quality evolution, examples from Triassic conglomerates/arenites in the Edvard Grieg field, Norwegian North Sea. Marine and Petroleum Geology. Volume 93, Pages 247-271.

Markussen, Ø., Dypvik, H. and Hammer, E., (2019) Basement clast distribution and sedimentary facies analysis of alluvial fan conglomerates, Edvard Grieg field, North Sea. Unpublished manuscript, submitted to MPG (2019).

Markussen, Ø., Dypvik, H., Hammer, E., Long, H., & Hammer, Ø. (2019). 3D characterization of porosity and authigenic cementation in Triassic conglomerates/arenites in the Edvard Grieg field using 3D micro-CT imaging. Marine and Petroleum Geology, 99, 265-281.

McEwan, I. K., Sheen, T. M., Cunningham, G. J., and Allen, A. R. (2000, December). Estimating the size composition of sediment surfaces through image analysis. In Proceedings of the Institution of Civil Engineers-Water and Maritime Engineering(Vol. 142, No. 4, pp. 189-195). Thomas Telford Ltd.

Milton, N. (1993). Evolving depositional geometries in the North Sea Jurassic rift. Geological Society, London, Petroleum Geology Conference series. Geological Society of London, 425-442.

Morad, S., Ketzer, J. R. M. and De Ros, L. F. (2000). Spatial and temporal distribution of diagenetic alterations in siliciclastic rocks: implications for mass transfer in sedimentary basins. Sedimentology, 47(s1), 95-120.

Nadeau, P. H., Bjørkum, P. A., and Walderhaug, O. (2005). Petroleum system analysis: Impact of shale diagenesis on reservoir fluid pressure, hydrocarbon migration, and biodegradation risks. Geological Society, London, Petroleum Geology Conference series vol. 6, No. 1, pp. 1267-1274.

Nemec, W., and Steel, R. 1984. Alluvial and coastal conglomerates: their significant features and some comments on gravelly mass-flow deposits.

Nguyen, B. T., Jones, S. J., Goulty, N. R., Middleton, A. J., Grant, N., Ferguson, A., and Bowen, L. (2013). The role of fluid pressure and diagenetic cements for porosity preservation in Triassic fluvial reservoirs of the Central Graben, North Sea. AAPG bulletin, 97(8), 1273-1302.

Nickel, E. (1985). Carbonates in alluvial fan systems. An approach to physiography, sedimentology and diagenesis. Sedimentary Geology, 42(1), 83-104.

NORLEX, (2012).

www.nhm2.uio.no/norlex/StandardLithostratigraphicWallchartOffshoreNorway.pdf.

North, C. P., Todd, S. P., and Turner, J. P. 1989. Alluvial fans and their tectonic controls. Journal of the Geological Society, 146(3), 507-508.

NPD, (2018). www.factpages.npd.no/FactPages [Accessed on November, 2018].

Nøttvedt, A., gabrielsen, R. and steel, R. (1995). Tectonostratigraphy and sedimentary architecture of rift basins, with reference to the northern North Sea. Marine and Petroleum Geology, 12**,** 881-901.

Odinsen, T., Reemst, P., Van Der Beek, P., Faleide, J. I. and Gabrielsen, R. H. (2000). Permo-Triassic and Jurassic extension in the northern North Sea: results from tectonostratigraphic forward modelling. Geological Society, London, Special Publications, 167**,** 83-103.

Pearson, M. J., and J. S. Small, (1988). Illite/smectite diagenesis and palaeotemperatures in northern North Sea: Clay Minerals, v. 23, p. 109-132.

Peltonen, C., Ø. Marcussen, K. Bjørlykke, and J. Jahren, (2008). Mineralogical control on mudstone compaction: a study of Late Cretaceous to Early Tertiary mudstones of the Vøring and Møre basins, Norwegian Sea: Petroleum Geoscience, v. 14, p. 127-138.

Pierson, T. C. (1981). Dominant particle support mechanisms in debris flows at Mt Thomas, New Zealand, and implications for flow mobility. Sedimentology, 28(1), 49-60.

Pierson, T. C., and Scott, K. M. (1985). Downstream dilution of a lahar: transition from debris flow to hyperconcentrated streamflow. Water resources research, 21(10), 1511-1524.

Pittman, E. D., R. E. Larese, and M. T. Heald, 1992, Clay coats: Occurrence and relevance to preservation of porosity in sandstones, in D. W. Houseknecht and E. D. Pittman, eds., Origin, diagenesis, and petrophysics of clay minerals in sandstones: SEPM Special Publication 47, p. 241-264.

Rattey, R. and Hayward, A. (1993). Sequence stratigraphy of a failed rift system: the Middle Jurassic to Early Cretaceous basin evolution of the Central and Northern North Sea.

Geological Society, London, Petroleum Geology Conference series. Geological Society of London, 215-249.

Reid, I., Rice, S., and Garcia, C., (2001), Discussion of "The measurement of gravel-bed river morphology", in Mosley, M. P. ed., Gravel-Bed Rivers V: New Zealand Hydrological Society, Wellington, p. 325-327.

Riber, L., Dypvik, H. and Sørlie, R. (2015). Altered basement rocks on the Utsira High and its surroundings, Norwegian North Sea. Norwegian Journal of Geology, 93, 57-89.

Roberts, A., Yielding, G., Kusznir, N., Walker, I. and Dorn-Lopez, D. (1995). Quantitative analysis of Triassic extension in the northern Viking Graben. Journal of the Geological Society, 152**,** 15-26.

Ross, G. J. (1969). Acid dissolution of chlorites: release of magnesium, iron and aluminum and mode of acid attack. Clays and Clay Minerals, 17(6), 347-354.

Rupke, L., Schmalholz, S., Schmid, D. and Podladchikov, Y. (2008). Automated thermotectonostratigraphic basin reconstruction: Viking Graben case study. Aapg Bulletin, 92**,** 309-326.

Rust, B.R. (1978). Depositional models for braided alluvium. In: Miall, A.D. (Ed.), Fluvial Sedimentology. Canadian Society of Petroleum Geologists, Memoir 5, p. 605-625

Selley, R. C. (1997). Elements of petroleum geology. Academic Press.

Sime, L. C., and Ferguson, R. I., (2003), Information on grain sizes in gravel-bed rivers by automated image analysis: Journal of Sedimentary Research, v. 73, no. 4, p. 630-636.

Slagstad, T., Davidsen, B. and Daly, J. S. (2011). Age and composition of crystalline basement rocks on the Norwegian continental margin: offshore extension and continuity of the Caledonian-Appalachian orogenic belt. Journal of the Geological Society, 168**,** 1167-1185.

Sohn, Y. K., Choe, M. Y., and Jo, H. R. (2002). Transition from debris flow to hyperconcentrated flow in a submarine channel (the Cretaceous Cerro Toro Formation, southern Chile). Terra Nova, 14(5), 405-415.

Steel, R., and Gloppen, T. G. (1980). Late Caledonian (Devonian) Basin Formation, Western Norway: Signs of Strike-Slip Tectonics during Infilling. Sedimentation in oblique-slip mobile zones, 79-103.

Steel, R. (1993). Triassic-Jurassic megasequence stratigraphy in the Northern North Sea: rift to post-rift evolution. Geological Society, London, Petroleum Geology Conference series. Geological Society of London, 299-315.

Stemmerik, L., Ineson, J. and Mitchell, J. (2000). Stratigraphy of the Rotliegend group in the Danish part of the Northern Permian Basin, North Sea. Journal of the Geological Society, 157**,** 1127-1136.

Taylor, T. R., R. Stancliffe, C. I. Macaulay, and L. A. Hathon, (2004). High temperature quartz cementation and the timing of hydrocarbon accumulation in the Jurassic Norphlet Sandstone, offshore Gulf of Mexico, U.S.A., in J. M. Cubit, W. A. England, and S. Larter, eds., Understanding petroleum reservoirs: Towards an integrated reservoir engineering and geochemical approach: Geological Society (London) Special Publication 237, p. 257-278.

Taylor, T. R., Giles, M. R., Hathon, L. A., Diggs, T. N., Braunsdorf, N. R., Birbiglia, G. V., Kittridge, M.K., Macaulay, C.I., and Espejo, I. S. (2010). Sandstone diagenesis and reservoir quality prediction: Models, myths, and reality. AAPG Bulletin, 94(8), 1093-1132.

Thomson, A., (1979). Preservation of porosity in the deep Woodbine/Tuscaloosa trend, Louisiana: Gulf Coast Association of Geological Societies Transactions, v. 30, p. 396-403.

Velde, B. B., and Meunier, A. (2008). The origin of clay minerals in soils and weathered rocks. Springer Science and Business Media.

Van Der Baan, D. (1990). Zechstein reservoirs in the Netherlands. Geological Society, London, Special Publications, 50(1), 379-398.

Vollset, J. G. and Doré, A. G. (1984). A revised Triassic and Jurassic lithostratigraphic nomenclature for the Norwegian North Sea, Bulletin No. 3, Norwegian Petroleum Directorate.

Wells, S. G., and Harvey, A. M. 1987. Sedimentologic and geomorphic variations in storm-generated alluvial fans, Howgill Fells, northwest England. Geological Society of America Bulletin, 98(2), 182-198.

Wilkinson, M. and Haszeldine, R. S. 2002. Fibrous illite in oilfield sandstones-a nucleation kinetic theory of growth. Terra Nova, 14(1), 56-60.

Wilson, M. D., and E. D. Pittman, (1977). Authigenic clays in sandstones: Recognition and influence on reservoir properties and paleoenvironmental analysis: Journal of Sedimentary Petrology, v. 47, p. 1-31.

Worden, R. H. and Morad, S. (2003). Clay minerals in sandstones: controls on formation, distribution and evolution. In Worden R. H. and Morad S. (eds.): Clay mineral cements in sandstones, 1-41.

Wright, V. P., and M. E. Tucker, (1991). Calcrete: an introduction, in V. P. Wright, and M. E.Tucker, eds., Calcretes, p. 1-22.

Yielding, G., Badley, M. E. and Roberts, A. M. (1992). The structural evolution of the Brent Province. Geological Society, London, Special Publications, 61**,** 27-43.

Ziegler, P. A. (1975). Geologic evolution of North Sea and its tectonic framework. AAPG Bulletin, 59(7), 1073-1097.

Ziegler, P.A., (1990). Tectonic and paleogeographic development of the North Sea rift system, in D. J. Blundell and A.D. Gibbs, eds, Tectonic Evolution of the North Sea Rifts: International Lithosphere Programme, 181, p. 1-36.

Ziegler, P. (1992). North Sea rift system. Tectonophysics, 208**,** 55-75.

Papers

I

Paper 1

Diagenetic influence on reservoir quality evolution, examples from Triassic conglomerates/arenites in the Edvard Grieg field, Norwegian North Sea

By

Mahmic, O., Dypvik, H., and Hammer, E.

Marine and Petroleum Geology

Volume 93, May 2018, Pages 247-271

Marine and Petroleum Geology 93 (2018) 247–271

Contents lists available at ScienceDirect

Marine and Petroleum Geology

journal homepage: www.elsevier.com/locate/marpetgeo

Research paper

Diagenetic influence on reservoir quality evolution, examples from Triassic conglomerates/arenites in the Edvard Grieg field, Norwegian North Sea

Orhan Mahmic[a,*], Henning Dypvik[a], Erik Hammer[b]

[a] Department of Geosciences, University of Oslo, P.O. Box 1047, Blindern, NO–0316, Oslo, Norway
[b] Lundin Norway AS, Strandveien 4, NO–1366, Lysaker, Norway

ARTICLE INFO

Keywords:
Edvard Grieg field
Conglomerate/arenites
Diagenesis
Reservoir quality
Triassic deposits

ABSTRACT

The Utsira High (Southern Norwegian North Sea) has been a petroleum exploration target since the late 1960s. The southwestern part of the Utsira High complex (Haugaland High) attracted new interest when in 2007 Lundin Norway AS and partners Revus Energy ASA and RWE Dea Norge AS discovered commercial hydrocarbon reservoirs in Triassic to Early Cretaceous formations (Edvard Grieg field).

In the present study, four siliciclastic cores from the Edvard Grieg field have been investigated sedimentologically, including core logging, optical mineralogy, X-ray powder diffraction (XRD) and scanning electron microscope (SEM). Quantification and characterization of the different mineralogical phases in thin section have been executed to better understand porosity evolution through time. Intergranular volume (IGV) and cement volume were also compared in order to estimate the most important factors effecting porosity loss within the studied samples.

The results show that through time the various diagenetic events and phases, such as dissolution of unstable grains and precipitation of clay minerals and cements, strongly influenced reservoir quality in the Edvard Grieg field. Two main lithology groups are identified within the cored intervals, conglomerates and sandstones. These two groups can further be sub-divided into four units: 1) sandy conglomerate, 2) silty conglomerate, 3) interbedded sandstone, 4) large scale cross-bedded sandstone. Most of the reservoir quality reduction in the conglomerate matrix can be related to poor sorting, carbonate cement and pore-filling/pore-lining authigenic clay minerals. Better reservoir quality characterizes the sandstone-dominated alluvial fan intervals, which generally are associated with a greater degree of sorting that led to higher intergranular porosities. Large scale cross-stratified sandstone units, interpreted to be of aeolian origin, have the highest reservoir quality. These deposits are moderately to well sorted with only minor occurrences of patchy carbonate cement and generally low proportions of authigenic minerals. However, locally abundant kaolinite has been observed, filling the pore space and reducing the porosity, predominantly by blocking interconnected primary pores.

1. Introduction

Since hydrocarbon exploration started on the Norwegian Continental Shelf (NCS), several discoveries have been made in the northern and central parts of the Utsira High region, e.g. Balder, Sleipner, Heimdal, Ringhorne, Grane, and Jotun fields (NPD, 2017). Initial exploration on the southern part of the Utsira High in the 1970s revealed only minor oil and gas discoveries, in brecciated igneous rock (well 16/1–4) and Cretaceous limestone sequences (well 16/1–5); both wells were abandoned.

The main reservoir units in the Edvard Grieg field consist of conglomerate and sandstone units at a burial depth of approximately 2000 m. Recent analyses (Riber et al., 2015) indicate promising reservoir properties also in the underlying fractured and altered basement, e.g. in well 16/1–15 in the northern part of the Edvard Grieg field (Fig. 1) (NPD, 2017 - the Tellus prospect).

Diagenetic heterogeneities can have a strong influence on reservoir quality and profoundly modify the porosity and permeability characteristics (Morad et al., 2000; Salem et al., 2000; Taylor et al., 2010; Bjørlykke, 2014). Detailed quantification of diagenetic phases may assess reservoir evolution through time by estimating the impacts of mineralogy and the distribution of diagenetic alterations on reservoir quality. This approach allows porosity evolution to be linked with diagenetic phases.

The present paper focuses on the mineralogical and diagenesis development and relevant reservoir characteristics through time in

* Corresponding author.
E-mail address: orhan.mahmic@geo.uio.no (O. Mahmic).

https://doi.org/10.1016/j.marpetgeo.2018.03.006
Received 5 September 2017; Received in revised form 26 February 2018; Accepted 6 March 2018
Available online 09 March 2018
0264-8172/

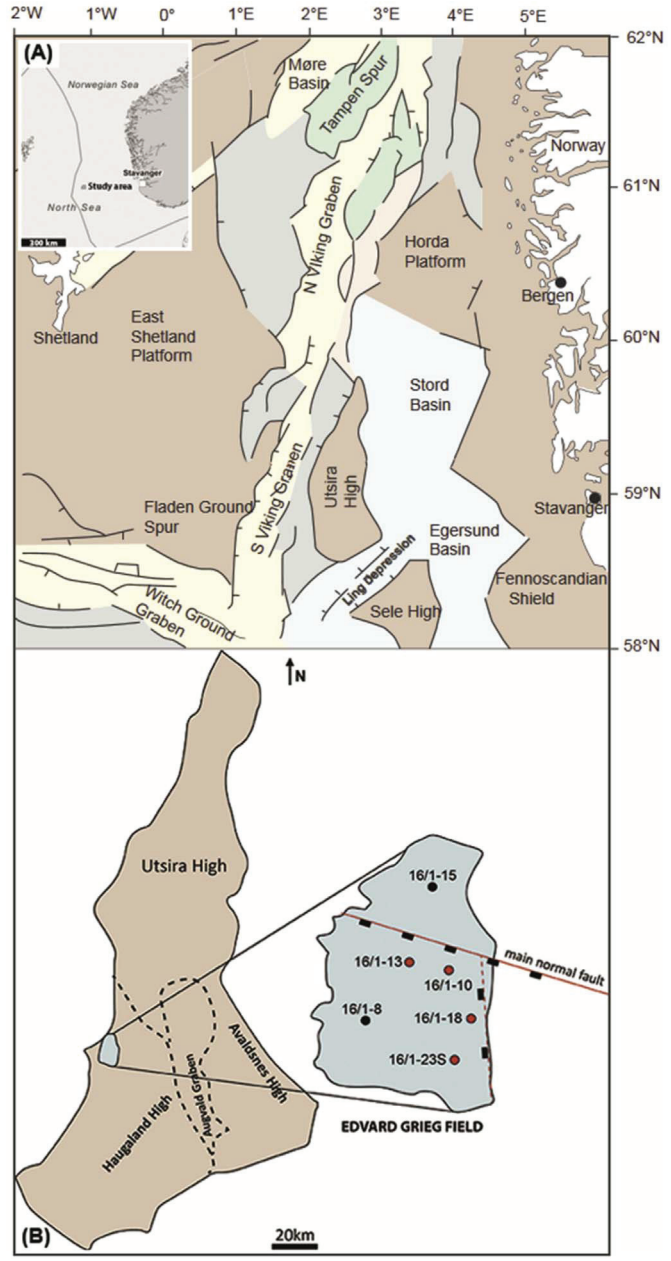

Fig. 1. (A) Regional map, showing the main fault trends, shear zones (grey lines) and different grabens and structural highs in northern North Sea (Modified from Riber et al., 2015). (B) Well map showing the wells used in this study (red circles), major normal fault (solid red line) and a minor normal fault (dashed red line). (For interpretation of the references to colour in this figure legend, the reader is referred to the Web version of this article.)

Triassic siliciclastics. Relative variations in the abundance of various framework grains and their textural relationships with authigenic components have had direct impact on reservoir porosity. Cores and logs from four wells, 16/1–10, 16/1–13, 16/1–18 and 16/1-23S (Fig. 1B), have been made available by Lundin Norway AS and are the basis for the present study.

The term early diagenesis includes processes that take place at the surface or in the shallow subsurface under the influence of depositional fluids and temperatures up to 60° to 70 °C, about 2 km burial depth. Late diagenesis includes processes and reactions that occur from approximately depths ≥2 km and temperatures ≥70 °C, which corresponds to the initiation of chemical compaction, clay mineral transformation reactions and quartz cementation (Morad et al., 2000).

2. Geological setting

The Utsira High is a large intrabasinal structural high (about 200 × 50 km) and has probably been a positive structural element since Late Palaeozoic (Laursen et al., 1995). It is flanked by the Viking Graben to the west, Ling Depression to the south and Stord Basin to the east (Fig. 1). The Edvard Grieg field is part of the southwestern Utsira High (Haugaland High), situated on the eastern margin of the southern Viking Graben. The studied wells are located in a fault-bounded area (half-graben), mostly composed of siliciclastic deposits, most likely of the Skagerrak Formation of the Hegre Group (Steel and Ryseth, 1990; NPD, 2017) (Fig. 2). The major Mid-Cimmerian Unconformity, caused by mantle plume development under the central North Sea (Morad et al., 1990b; Ziegler, 1990, 1992; Nøttvedt et al., 2008; Jackson et al., 2010), separates the underlying Skagerrak Formation from the overlying marine succession belonging to the Åsgard Formation - Cromer Knoll Group of Early Cretaceous age. The uplift phase was followed by subsidence and burial during crustal cooling (Gowers and Sæbøe, 1985; Morad et al., 1990b; Ziegler, 1992; Isaksen and Ledje, 2001). The top of the Skagerrak Formation is defined by an unconformity (BCU – Base Cretaceous Unconformity) that marks the base of the Åsgard Formation, while the base of the Skagerrak Formation has not been reached in the cores, but is known to be the Permian Zechstein Group (Fig. 2).

Sediments deposited during the Triassic corresponding to the Skagerrak Formation are dominated by alluvial and lacustrine systems including aeolian dunes and episodic (flash) flood events operating in an arid to semi-arid climatic regime (Goldsmith et al., 2003; Nystuen et al., 2014). During Late Triassic there was a shift towards semi-humid climate conditions, represented by fluvial sandstones, meandering rivers and an increase in smectite and kaolinite weathering products (Nystuen et al., 2014).

3. Samples and methods

A total 100 samples from full-diameter cores of wells 16/1–10, 16/1–13, 16/1–18 and 16/1-23S were used for determine the petrographic and diagenetic characteristics of the Edvard Grieg field deposits. Sedimentological description and facies characterization of full-diameter cores from the four wells are illustrated in Fig. 3(A) and (B), (C) and (D) and summarized in Tables 1 and 2. The mineralogical and petrographical analyses include optical microscopy, scanning electron microscopy (SEM), X-ray diffraction (XRD) of bulk rock and < 2 μm fraction and SEM-EDS mineralogical maps.

Polished thin sections, ground down to a standard 30 micron thickness, were impregnated with blue epoxy resin which helped the identification and illustration of pore space. Optical thin section microscopy was carried out with a *Nikon Labophot-Pol* petrographic microscope. The modal composition of the samples was estimated by counting 300 points in 78 selected samples, representing the different lithologies (Table 2). The point-counting results were used to calculate the intergranular volume (IGV), which is the sum of intergranular pore space, intergranular cement and depositional matrix. Depositional matrix is defined by silt and clay particles that fill the pore space between the framework grains.

Key samples were investigated under SEM–EDS *(Hitachi SU5000 FE-SEM, with a Dual Bruker Xflash30 EDS system)*. The thin sections were coated with a thin film of carbon, while freshly fractured samples were glued on brass stubs and coated with gold. SEM detectors used for analyses include secondary-electron image (SE), back-scatter image (BSE) and cathodoluminescence (CL) modes. The latter was used to identify quartz overgrowth.

Clay identification were carried out on a *Bruker D8 advanced (40 kV and 40 mA)* diffractometer with *Lynxeye XE High-Resolution Energy Dispersive 1D Detector*, using *CuKα* radiation. The < 2 μm fractions were extracted by gravity settling and analyzed four times: air-dried, treated with ethylene vapour for 24 h, heated to 350 °C for about 1 h, and

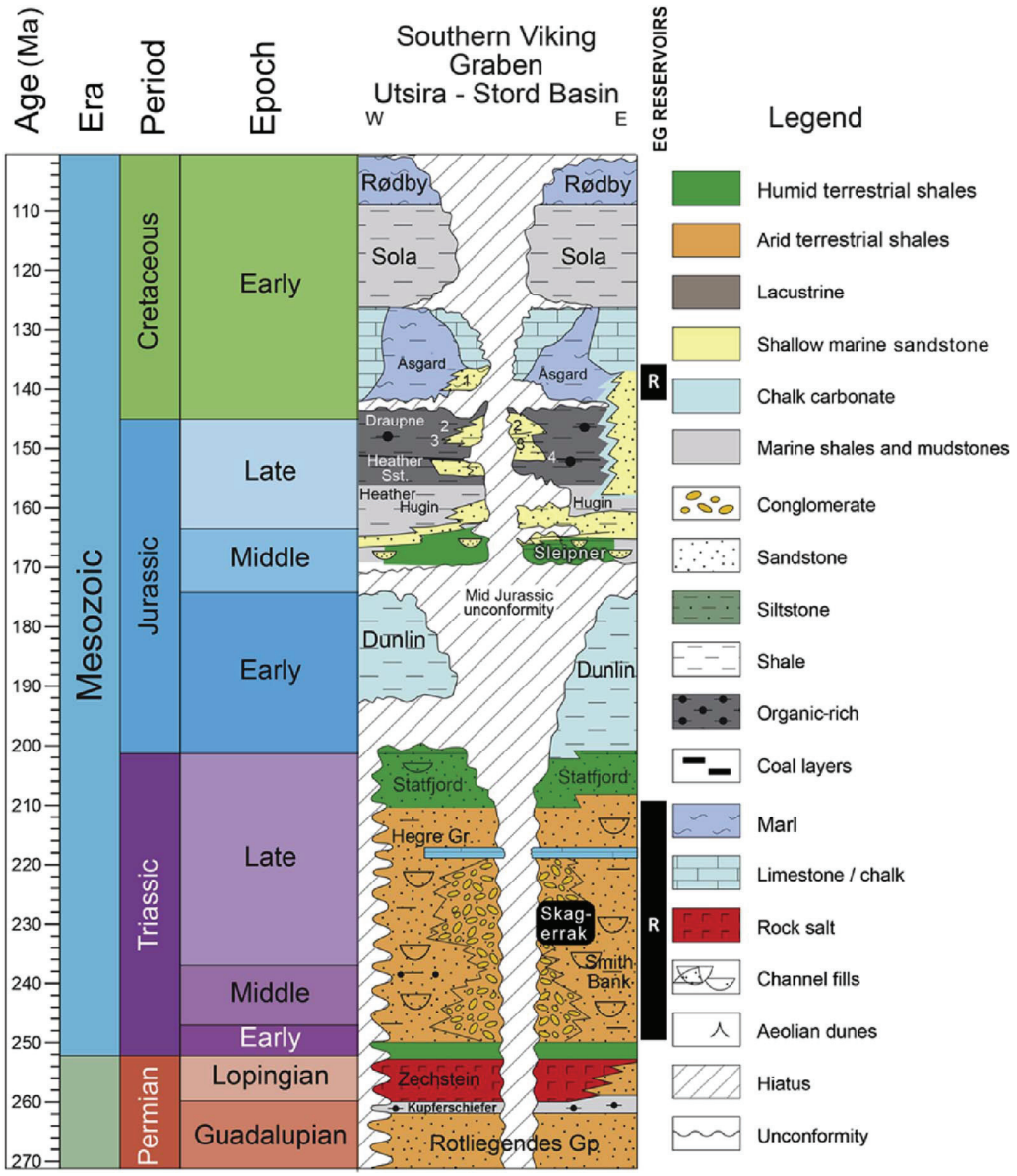

Fig. 2. Stratigraphic column of the Norwegian sector of the South Viking Graben, Utsira and Stord Basin (Modified from NORLEX Project, 2012). The main Edvard Grieg reservoir (R) is indicated in the figure.

finally heated to 550 °C for about 1 h.

Phase identification was conducted with the *Bruker* software Diffrac.EVA according to methods by Moore and Reynolds (1997). The Rietveld method, using the entire peak profile (Rietveld, 1969), was applied for quantification using open source Profex (BGMN) software version 3.8.0 (Döbelin and Kleeberg, 2015).

SEM-EDS HyperMap was used to produce mineralogical maps covering approximately 10 × 7 mm of thin sections. Further phase segmentation, phase grouping and quantification of diagenetic phases were performed on key samples using iSpectra software (Liebske, 2015), Adobe Illustrator and open source Fiji software (Schindelin et al., 2012). Only the main diagenetic phases that had the strongest impact on porosity loss were considered. The phases where then grouped into framework constituents (detrital grains), carbonate cement (calcite and dolomite), clay minerals (pore-filling and pore-lining) and porosity.

4. General sedimentological description and interpretation

Core description from wells 16/1–10, 16/1–13, 16/1–18 and 16/1-23s revealed the presence of two main lithology groups, conglomerates and sandstones (Table 1). Furthermore, the conglomerates can be sub-divided into **silty** and **sandy** conglomerate unit based on the percentage of sandy matrix. The sandstones can also be sub-divided into **interbedded sandstone** and **large scale cross-bedded sandstone** unit. Due to very similar depositional regimes, the silty and sandy conglomerate units are described and discussed together.

4.1. The silty and sandy conglomerate units

Thick conglomerate deposits dominate the logged core sections in the four wells (cf. Fig. 3). The conglomerates are typically composed of poorly sorted detritus and/or matrix supported deposits, displaying sharp erosive bases and tops (Fig. 4). Generally, the conglomerates are non-graded, but occasionally can display crude inverse grading. Clast

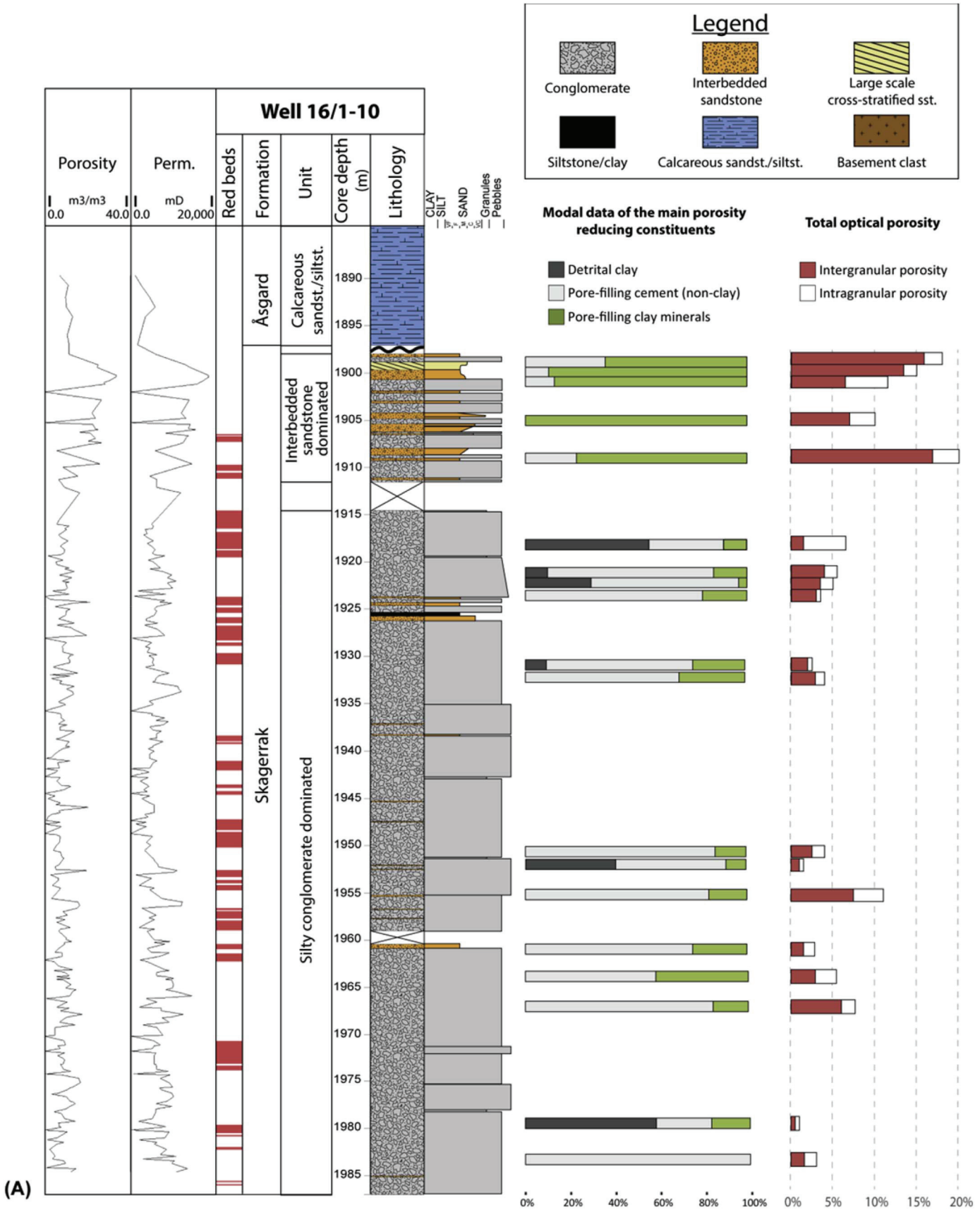

(caption on next page)

Fig. 3. (A) – Main lithologies and units in well 16/1–10. The right-side graph represents the modal data of the main porosity reducing constituents: **Detrital clay**, **Pore-filling cement** (calcite, dolomite and feldspar overgrowths), **Pore-filling clay minerals** (coating- and pore filling-clays, kaolinite and Fe-oxides). Total optical porosity was determined in thin sections analysis and consists of both the inter- and intragranular porosities. Left side graphs show experimental permeability (mD) and total helium porosity (%).
(B) – Main lithologies and units in well 16/1–13. The right-side graph represents the modal data of the main porosity reducing constituents: **Detrital clay**, **Pore-filling cement** (calcite, dolomite and feldspar overgrowths), **Pore-filling clay minerals** (coating- and pore filling-clays, kaolinite and Fe-oxides). Total optical porosity was determined in thin sections analysis and consists of both the inter- and intragranular porosities. Left side graphs show experimental permeability (mD) and total helium porosity (%). See legend in Fig. 3A.
(C) – Main lithologies and units in well 16/1–18. The right-side graph represents the modal data of the main porosity reducing constituents: **Detrital clay**, **Pore-filling cement** (calcite, dolomite and feldspar overgrowths), **Pore-filling clay minerals** (coating- and pore filling-clays, kaolinite and Fe-oxides). Total optical porosity was determined in thin sections analysis and consists of both the inter- and intragranular porosities. Left side graphs show experimental permeability (mD) and total helium porosity (%). See legend in Fig. 3A.
(D) – Main lithologies and units in well 16/1-23S. The right-side graph represents the modal data of the main porosity reducing constituents: **Detrital clay**, **Pore-filling cement** (calcite, dolomite and feldspar overgrowths), **Pore-filling clay minerals** (coating- and pore filling-clays, kaolinite and Fe-oxides). Total optical porosity was determined in thin sections analysis and consists of both the inter- and intragranular porosities. Left side graphs show experimental permeability (mD) and total helium porosity (%). See legend in Fig. 3A.

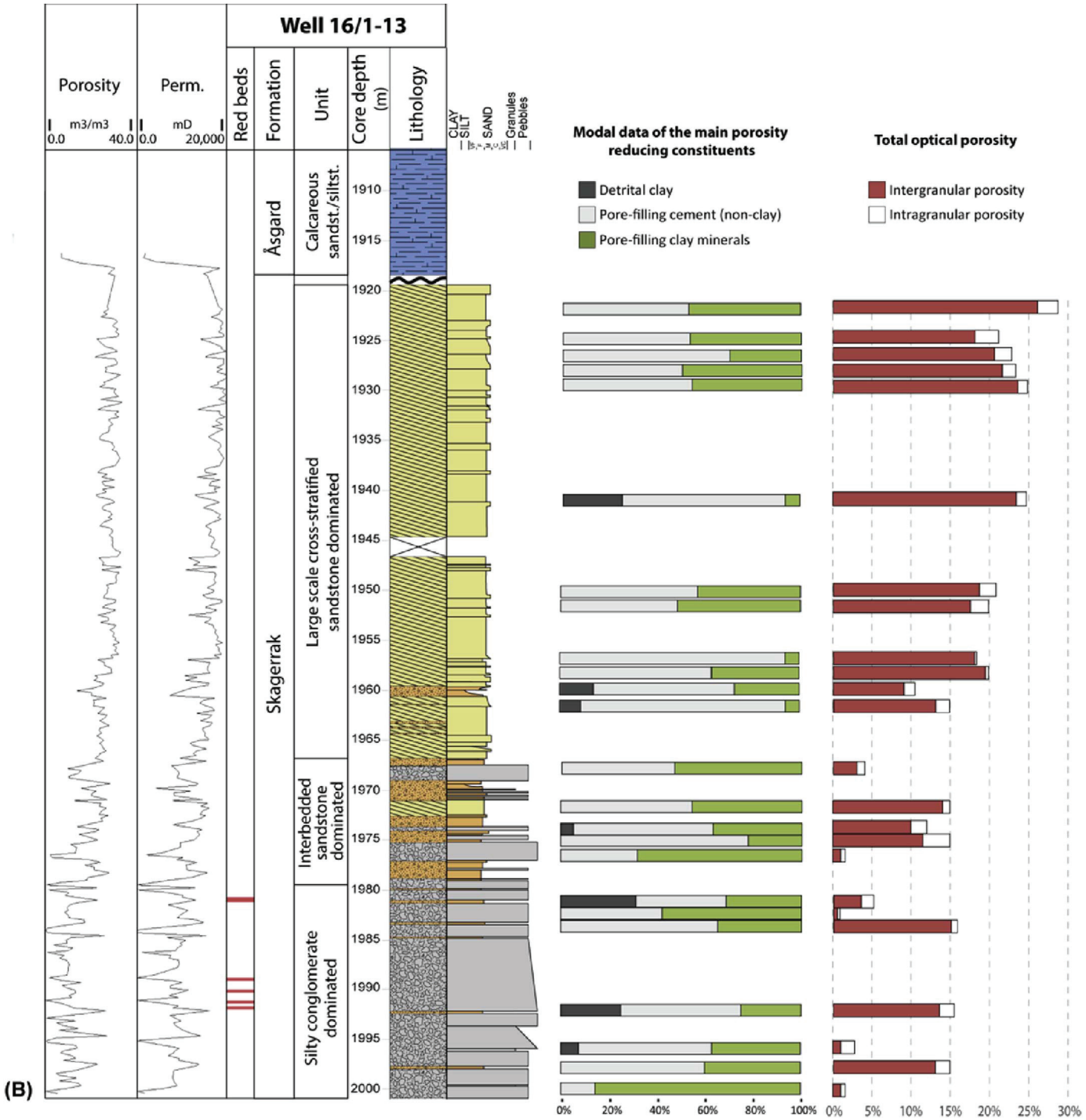

Fig. 3. (*continued*)

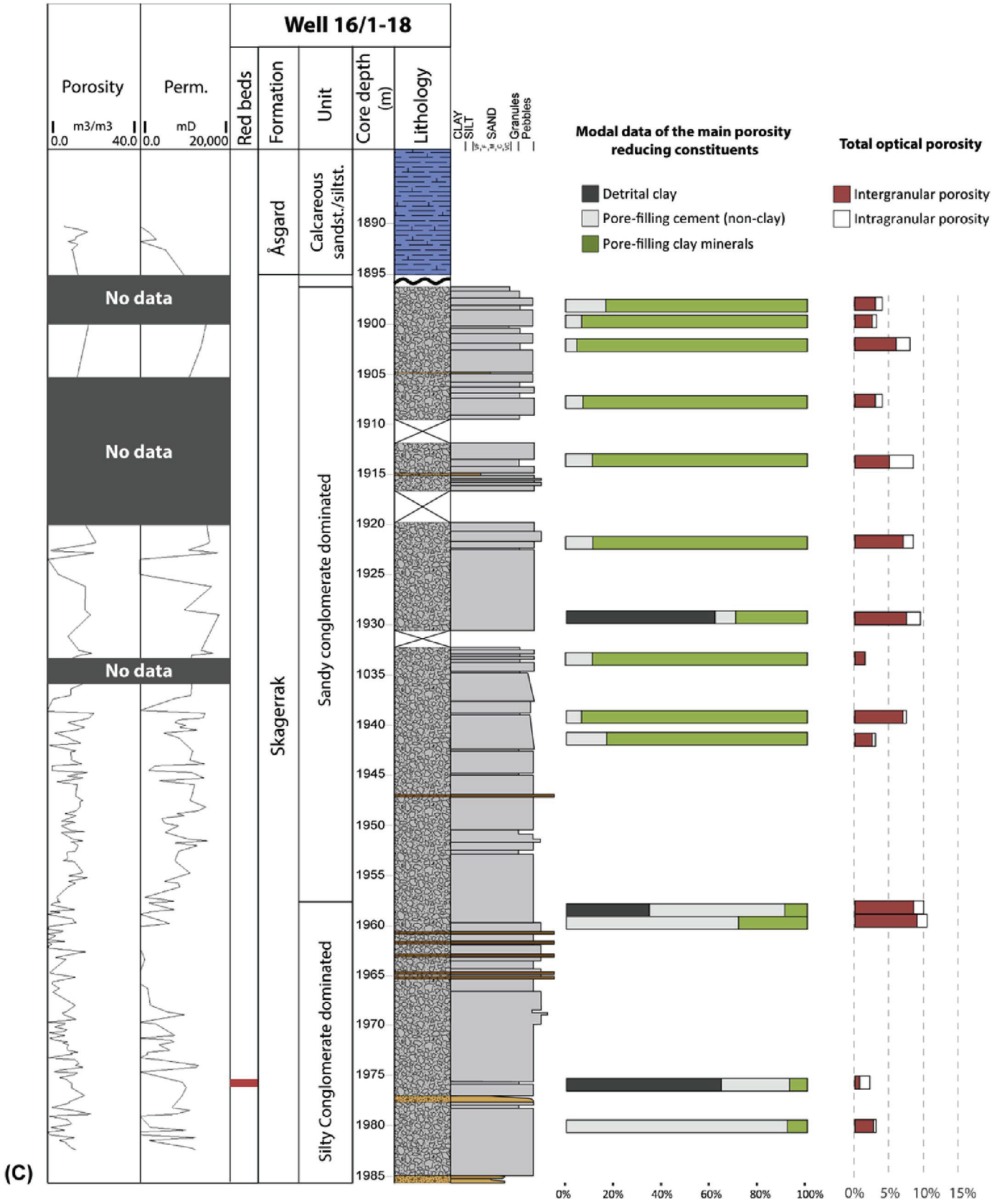

Fig. 3. (*continued*)

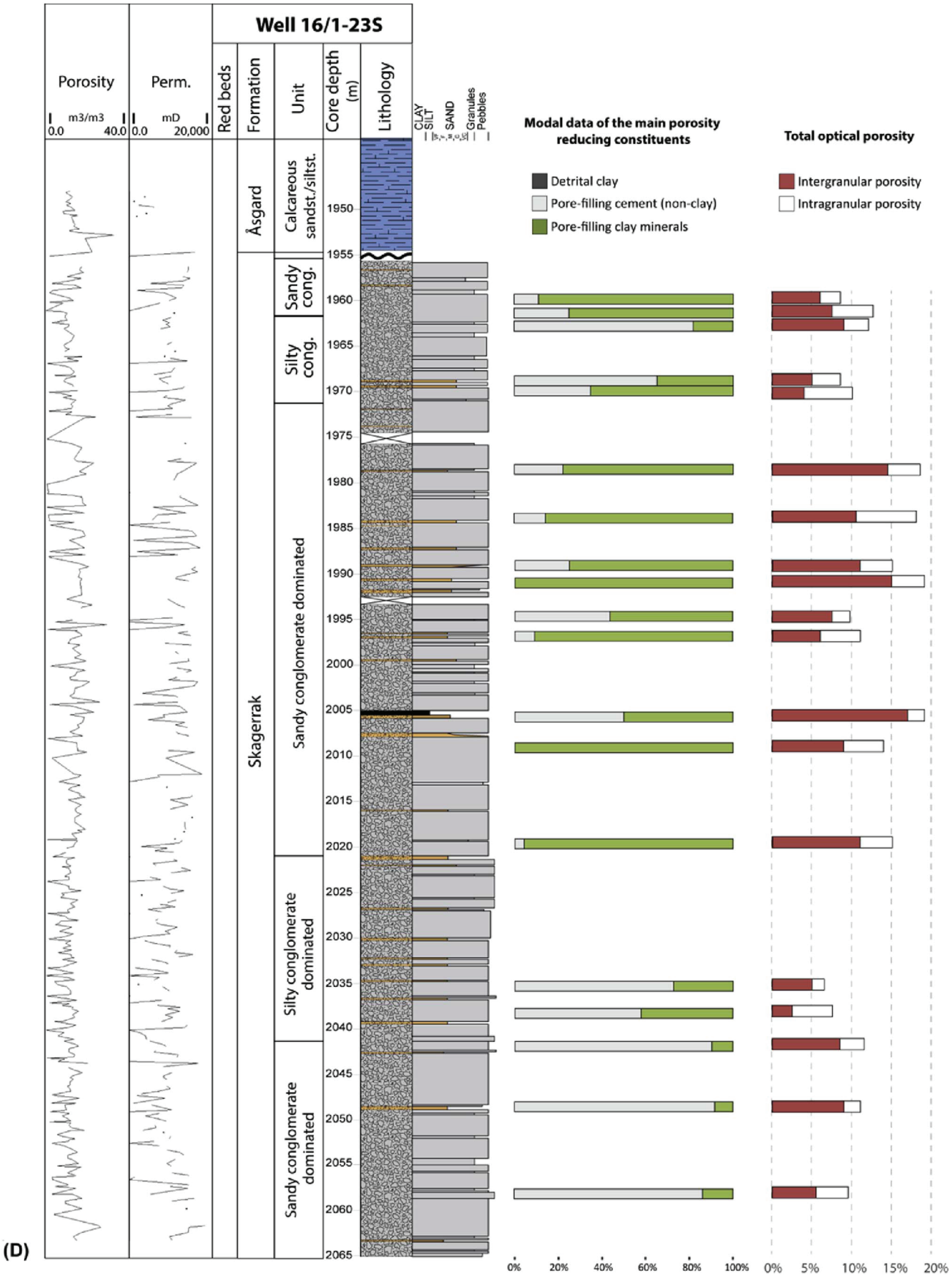

Fig. 3. (*continued*)

Table 1
Summary of characteristics for the four sub-lithologies in Edvard Grieg field.

Lithology group	Sub-lithology unit	Description	Total length in the core
Sandstones	Large scale cross- stratified sandstone unit	10s of meter-scale beds of moderately to well sorted sandstone. The grain size ranges from fine to medium sand. The beds are arranged in large scale cross-stratification sets (upper dm- to lower m-scale), with up to 20–30° dip angles, and planar stratification. Mm-scale pinestrips bedding and inverse grading is observed.	**16/1–10** - 2 m **16/1–13** - 46 m **16/1–18** - 0 m **16/1–23S** - 0 m
	Interbedded sandstone	Moderately to well sorted, fine to locally medium grained sandstone beds in between conglomerate beds. The interbedded sandstones display current ripple cross-lamination (occasionally climbing). The size of individual bed ranges from cm- to m-scale.	**16/1–10** - 10 m **16/1–13** - 10 m **16/1–18** - 4 m **16/1–23S** - 13 m
Conglomerates	Sandy conglomerate	Alluvial fan conglomerate with a more porous, permeable and sandy matrix (> 50%) compared to the sily conglomerate. The clasts are poorly to moderately sorted. The beds are either clast- and matrix-supported which commonly have erosive base and sharp tops. Occasionally beds display low-angle cross-stratification with weak alignment of clasts.	**16/1–10** - 0 m **16/1–13** - 1 m **16/1–18** - 59 m **16/1–23S** - 71 m
	Silty conglomerate	Alluvial fan conglomerate with silty or cemented matrix. The matrix is generally tight, especially in the red matrix zones. The clasts are poorly sorted, ranges up to cobble size. The beds are either clast- and matrix-supported which commonly have erosive base and sharp tops.	**16/1–10** - 76 m **16/1–13** - 24 m **16/1–18** - 25 m **16/1–23S** - 26 m

orientations tend to be variable and range from chaotic to crude imbrication and bedding. The modal grain size of the clasts ranges up to cobble size; they are generally subrounded to subangular. The matrix is mainly comprised of moderately to poorly sorted, very fine to coarse, quartz-rich sand (Table 2 and Fig. 5). The silty conglomerate is generally composed of silty and cemented matrix, and is relative tight, except in the interbedded sandstone layers. However, the sandy conglomerate unit has higher percentage of sandy matrix (> 50%), with thin interbedded sandstone layers. Furthermore, the sandy conglomerate matrix is more porous and permeable compared to the silty conglomerate matrix.

The different colours observed in both of the conglomerate types, i.e. grey, green and red colour (Fig. 6), reflect the distribution of detrital and authigenic clays and presence of Fe-oxides. The red Fe-oxide intervals are present in detrital clay-rich intervals. The green colour is associated with higher abundance of authigenic chlorite and smectite, and is often very similar to the red matrix in terms of reservoir characteristics (i.e. low porosity and permeability). The grey matrix type is dominant in all four wells and usually contain less chlorite but locally can have higher amounts of authigenic kaolinite (Table 3).

4.1.1. Interpretation

Similar deposits described from surface exposures by Bull (1972), Nilsen (1982), Nemec and Steel (1984) and Blair and McPherson (2009), all relate to alluvial fans. The low amount of detrital clay in the conglomerate matrix is indicative of rapid uplift and erosion with weathering confined to exposed granitic basement during arid to semi-arid climate (Blair and McPherson, 1994; Goldsmith et al., 2003; Went, 2005). Clasts in the Edvard Grieg deposits are dominated by feldspar-rich igneous rock fragments (granite and granodiorite composition). Crude inverse grading probably was due to density differentials during transport and kinematic sieving (Nemec and Steel, 1984; Kim and Lowe, 2004). The significant size of some of the clasts (large pebbles, cobble and possibly boulders), and occasional imbrication, indicates a high energy in-channel setting or debris flow deposits. The sandy conglomerate beds may have accumulated as the flow energy decreased in the channels, or could reflect laterally extensive sheetflood deposits.

4.2. Interbedded sandstone unit

The conglomerate units are sometimes interbedded with coarse to very-fine, poorly to moderately well sorted sandstone layers (cf. Figs. 3, 4C and 5). These sandstone beds consist of lithic arenites and wackes (after Pettijohn et al., 1987). The sandstones often exhibit planar-parallel lamination and fining-upwards beds with a pebbly base. Mud stringers, climbing ripples, and seasonal sedimentation (varves) have also been observed. The samples are mostly both texturally and mineralogically mature.

4.2.1. Interpretation

The common fining-upwards sandstone units are often interbedded with the conglomeratic units (Fig. 4A and C), and could represent shallow stream-channel flow, sheetwash, finer elements of hyperconcentrated flows or sandy debris flows (Gloppen and Steel, 1981). These sandstone beds represent waning flow profiles, going from clast-supported to matrix-supported conglomerates, to sandstone with climbing ripples. This suggests flash flood regimes. With increased water content and fluidity, i.e. sediment-water mixtures having between 40 and 80% sediment by weight, the mixture behaves as a hyperconcentrated flow (Nemec and Steel, 1984; Pierson and Scott, 1985). These kinds of flows produce sheet-like beds characterized by normally graded massive, or graded massive to stratified, beds. The deposits formed by sheetwash flood, which is shallow water moving across a shallow incline and not confined to a stream channel, are typically comprised of thin sheets of gravels and sands, often stratified with sand ripples and cross-beds (Bull, 1972; Harvey, 2011). In contrast, stream channel deposits are generally coarser grained and less sorted. The channel deposits can be imbricated, massive, or thick bedded (Bull, 1972). Occasional inverse grading is observed in these stream channel sandstones, which may represent fine-grained debris flow or grain flow deposits. Conglomeratic braided stream deposits are generally characterized by their clast-supported nature (Nemec and Steel, 1984). The textural maturity of the gravel deposits reflects the distance from the source and degree of reworking by transport. Material transported primarily by ephemeral (flash) flooding, e.g. alluvial fan stream deposits, tends to retain most of the original textural characteristics and shows the greatest textural immaturity (Nemec and Steel, 1984). The deposits can often show evidence of tractional transport, such as stratification, imbricated clasts and basal scouring.

The thin wave-rippled silty to clayey beds found in well 16/1–10 and 16/1-23S may reflect the development of an ephemeral pond or lake as exemplified in Gloppen and Steel (1981).

4.3. Large scale cross-stratified sandstone unit

The large scale cross-stratified sandstone units appear in cores from

Table 2
Minimum, maximum and average modal composition of major components (vol. %) for the four main lithologies in Edvard Grieg field. Total cement is sum of carbonate cements and feldspar overgrowth. **Intergranular volume (IGV)** is the sum of intergranular pore space, intergranular cement and depositional matrix. **Compactional porosity loss** is the percent of original porosity destroyed by compaction. **Cementational porosity loss** is the percent of original porosity destroyed by cementation (Ehrenberg, 1995). The **estimated temperature T^{O}** is based on average geothermal gradient of 40.5 °C from the wells. Total 78 thin sections have been analyzed.

	Conglomerates						Sandstones					
	Silty conglomerate			Sandy conglomerate			Interbedded sandstone			Large scale cross-stratified sandstone		
	(n = 23 samples)			(n = 19 samples)			(n = 24 samples)			(n = 12 samples)		
	Min	Max	Ave	Min	Max	Ave	Min	Max	Ave	Min	Max	Ave
Detrital minerals												
Monocrystalline quartz	4.0	19.4	12.7	5.0	32.0	12.5	14.5	39.0	26.8	22.0	33.8	27.6
Polycrystalline quartz	0.5	5.0	1.4	0.5	5.2	2.3	1.0	15.0	4.5	5.3	17.2	8.3
K-feldspar	2.0	16.2	4. S	1.0	15.0	6.1	2.7	17.0	9.2	4.0	15.0	11.8
Plagioclase	0.5	10.0	3.9	2.0	12.0	6.1	1.0	12.5	6.4	0.5	3.5	0.9
Metamorphic rock fragments	–	–	–	–	–	–	–	–	–	0.5	12.5	7.5
Igneous rock fragments	24.4	75.5	51.4	19.0	68.0	45.8	5.0	38.5	17.6	3.5	15.0	8.1
Mud clasts	0.5	5.5	1.9	0.5	3.5	1.5	0.5	5.5	2.0	2.5	2.5	2.5
Pseudomatrix	0.5	5.0	1.5	0.5	2.5	1.4	0.5	2.5	1.3	–	–	–
Mica	0.5	6.1	1.9	0.5	7.0	2.1	0.5	9.0	3.1	0.5	1.1	0.7
Chlorite	0.5	6.5	2.2	0.5	1.0	0.8	0.5	2.0	0.8	0.5	0.5	0.5
Detrital clay minerals	1.0	21.5	9.0	–	–	–	0.5	14.5	3.6	2.4	2.4	2.4
Authigenic phases												
Clay coatings + pore-filling clays	0.5	15.0	4.2	1.5	10.0	5.5	0.5	21.0	5.3	0.5	8.0	3.0
Replacive clays	0.5	8.9	3.7	2.5	9.0	5.2	1.0	9.5	3.6	0.5	7.0	3.3
Calcite cement	0.5	14.5	3.0	0.5	6.0	1.2	0.2	14.0	3.5	0.5	7.0	3.8
Dolomite cement	0.5	14.2	4.6	0.5	11.0	4.4	0.5	12.5	5.2	0.5	0.5	0.5
Kaolinite	0.2	2.0	0.8	0.2	5.7	2.1	0.3	11.5	3.6	0.5	9.0	2.1
Iron oxides	0.5	4.0	1.3	–	–	–	–	–	–	–	–	–
Feldspar overgrowths	0.5	3.5	1.1	0.3	2.0	0.7	0.5	2.5	1.1	0.5	4.0	1.5
Porosity												
Intergranular porosity	0.5	6.0	2.2	2.5	14.5	6.7	5.0	17.0	10.5	16.0	26.0	20.1
Intragranular porosity	0.4	5.0	1.4	0.5	7.5	3.0	1.0	5.0	2.5	1.0	5.5	2.6
Totals												
Detrital grains	70.0	93.0	81.3	67.3	84.3	76.4	57.5	79.5	70.5	59.0	70.5	64.7
Cements (non-clay)	0.5	16.5	7.3	–	14.0	2.8	–	14.5	5.9	2.5	8.0	4.5
Optical porosity	1.0	7.0	3.5	3.0	18.5	9.7	7.5	20.0	13.0	18.0	29.0	22.7
Intergranular volume (IGV)	4.7	24.0	14.7	10.5	26.0	15.9	15.0	36.5	23.7	23.5	37.0	29.4
Compaction-porosity loss	7.1	26.5	17.6	4.5	21.8	16.6	5.5	29.4	20.8	4.8	21.6	14.7
Cementation-porosity loss	2.2	21.0	10.1	3.2	31.3	7.8	2.2	23.9	10.6	3.8	16.3	8.1
Quartz (Q)	5.0	30.8	13.5	8.5	56.8	20.0	25.4	64.0	47.6	47.5	73.0	56.3
Feldspars (F)	3.1	33.0	12.3	3.8	31.5	17.3	14.4	74.1	26.8	7.4	25.4	20.0
Lithics (L)	43.1	91.8	68.1	29.0	85.0	62.7	9.9	55.8	28.2	17.9	29.7	23.7
Helium porosity	5.9	21.4	11.0	9.4	19.3	15.2	10.2	30.5	21.6	23.8	33.5	28.4
Permeability Kh (mD)	0.2	55.2	6.3	1.7	46.2	17.3	1.9	2062	336	249	16,809	4636
Grain size (median value)	0.1	6.6	0.3	0.1	4.8	0.5	0.1	1.7	0.2	0.1	0.9	0.3
Estimated temperature T°	77.3	82.5	79.4	76.8	82.7	79.3	76.9	83.3	79.9	76.9	79.3	78.4

well 16/1–13, between 1960 and 1920 m depth, and possibly a minor interval in well 16/1–10 at 1899.80 m depth (Fig. 3). The large scale cross-stratified sandstone in well 16/1–13 consists of fine to medium grained, moderately well sorted sandstones (Table 2 and Fig. 5). Well defined mm-scale pinstripe bedding can be observed in thin sections (Fig. 7). The deposits are dominated by large scale cross-stratification (upper dm-to lower m-scale), with up to 20-30° dip angles, and planar stratification. These cross-sets exhibit steepening-upward bottomset to foreset transitions with truncated tops (Fig. 4D). Examples of inverse grading have been observed. The cross-stratified sandstones are dominantly arenites and texturally mature. The dominant colour is light to medium brown, due to hydrocarbon staining.

4.3.1. Interpretation

The sedimentological features, e.g. truncated bed tops, inverse grading and 20-30^{O} foreset inclination observed in the large scale cross-stratified sandstone in the Edvard Grieg field are consistent with aeolian dune deposits (meter-scale) (Mountney, 2006; Rodríguez-López et al., 2012). The well-defined pinstripe bedding observed in thin sections (Fig. 7E) may either represent wind ripple migration, or grain flow and grain fall processes (Mountney, 2006). The individual cross-stratified sets often show steepening-upward development from bottomset to foreset with truncation on the tops (Fig. 4D). This steepening-upwards trend records the migration of individual meter-scale dunes over previous, truncated aeolian beds.

Periodical sharp erosional surfaces with pebbly lag, imbrication, trough cross-stratification, may indicate fluvial processes interrupting aeolian dune development. Reworking of aeolian deposits by fluvial streams may lead to difficulties in interpretation, as sedimentological characteristics of these fluvial deposits would carry inherited characteristics for the aeolian mechanisms of transport and deposition. Evidence of planar laminated siltstone beds and intraformational

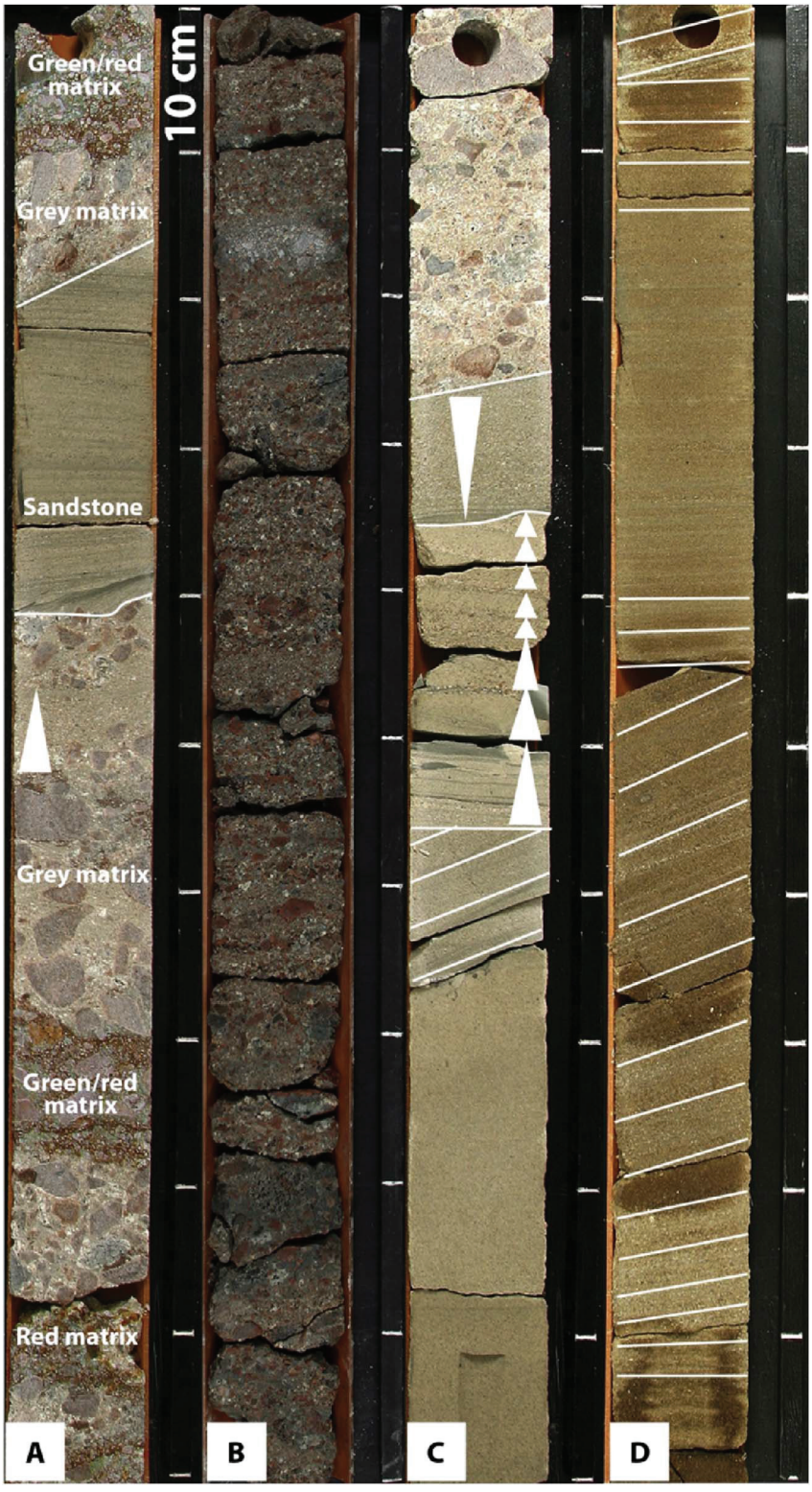

Fig. 4. (A) The silty conglomerate-dominated alluvial fan deposits (16/1–13, 1992–1993 m) consist of poorly sorted, pebble-to cobble-grade, clast- and matrix-supported conglomerates. Note the inter-bedded sandstone interval and red/green matrix. (B) The sandy conglomerate (16/1-23s, 2054–2055 m) is composed of poorly sorted, pebble-grade matrix- and clast-supported conglomerate and has higher sand content than the silty conglomerate. (C) The inter-bedded sandstone unit (16/1–13, 1977–1978 m) showing fining upwards intervals with one upwards coarsening interval that is overlain by silty conglomerate. The lower part may represent an interval of the large scale cross-stratified sandstone. (D) The large scale cross-stratified deposits (16/1–13, 1936–1937 m) are composed of moderate to well sorted sandstones. The picture shows truncation surfaces separating cross-sets. Relative steeply dipping foresets have been observed, steepening upwards from bottomset to foreset. (For interpretation of the references to colour in this figure legend, the reader is referred to the Web version of this article.)

mudstone may suggest the presence also of interdune ponds (Mountney, 2006).

5. Results

5.1. Textural data

Modal grain size within the studied thin sections varies from silt to upper coarse sand, with majority of the samples ranging from fine to medium sand (Fig. 5 and Table 2). The coarsest (upper medium to upper coarse sand) plot within the lithic field, generally indicating decreasing maturity with increasing grain size. There is a large variation in sorting, ranging from poorly sorted conglomerates to moderately well sorted sandstones. Additionally, many samples of the sandy conglomerate have moderate sorting.

The QFL plots (Fig. 5) shows that majority of the large scale cross-

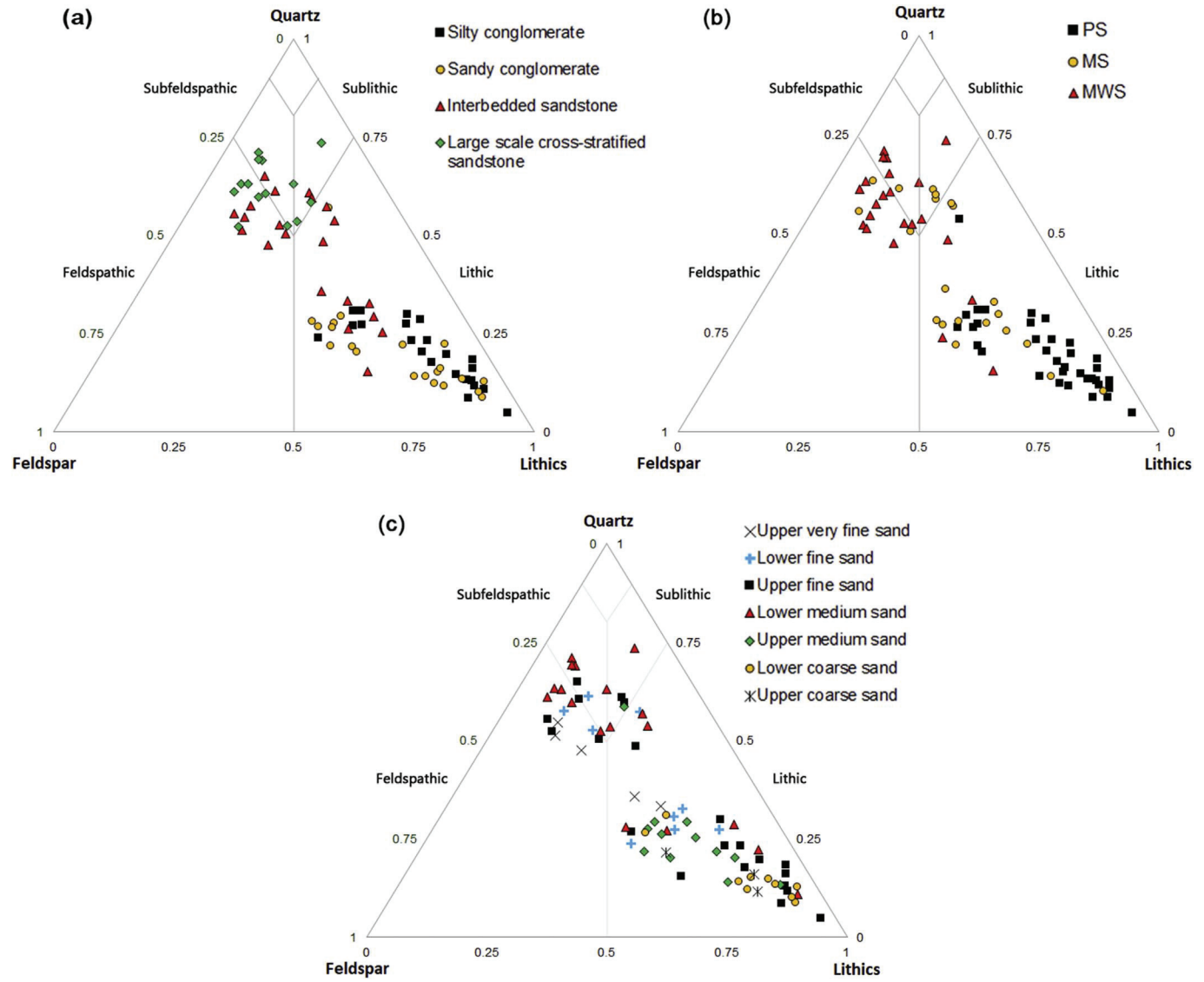

Fig. 5. Detrital composition of the different lithology units (QFL plots) from all four wells, divided into a) four main lithology units, b) petrographically-derived sorting where PS = poorly sorted, MS = moderately sorted and MWS = moderately well sorted, c) petrographically derived grain size. (After, Pettijohn et al., 1987).

stratified sandstone and interbedded sandstone samples plot around the subfeldspathic/feldspathic boundary, which indicate no major variation in quartz, feldspar and lithic proportions. Furthermore, these samples are also better sorted and more mineralogically mature compare to the poorly sorted and immature conglomeratic samples that plots around the lithic end-member. However, half of the interbedded sandstone samples also plot in the sublithic/lithic area. These samples are moderately mature and contain higher portion of lithic grains. The textural composition also resembles that of the sandy conglomerate matrix.

5.2. Petrographic data

5.2.1. Detrital minerals

The main framework constituents in all the lithologies are quartz, feldspar, and locally abundant rock fragments (Table 2 and Fig. 5). The SEM and XRD analyses show that the detrital clay minerals are composed of mixed-layer illite/smectite (I/S) and illite + mica mixtures. Micas (biotite, muscovite and chlorite), opaque minerals and heavy minerals occur in varying amounts throughout the cores.

Quartz grains generally have the highest abundance and correspond mostly to monocrystalline quartz, with varying but minor amounts of polycrystalline quartz. The quartz ranges from very fine to medium grained, subangular to rounded grains.

Feldspars may occur in abundance, exceeding 25% in some samples. They display varying degrees of preservation, from no traces of weathering to totally altered or dissolved grains. The highest weathering degree is developed on the plagioclase grains. Plagioclase grains are lamellar twinned and often largely replaced by authigenic clay minerals, e.g. kaolinite and illite. Some grains look fresh while others are highly or totally weathered to clay minerals, for example kaolinite and smectite. K-feldspars (microcline) are locally altered to kaolinite and other clay minerals, and locally overgrown by K-feldspar cement.

Rock fragments are mostly composed of igneous lithologies, such as granite and granodiorite, eroded from the adjacent basement rock. The abundance of rock fragments differs significantly between the lithological units (Table 2) with highest abundance in the conglomerate units (up to 75.5%). Some metamorphic rock fragments, e.g. gneiss, have also been documented in the cross-stratified sandstone, which may indicate different provenance areas. The igneous fragments are predominately composed of quartz and K-feldspar, with varying amounts of plagioclase, muscovite, biotite and chlorite. The rock fragments are generally altered in some degree and usually replaced by authigenic clay minerals and carbonate cement.

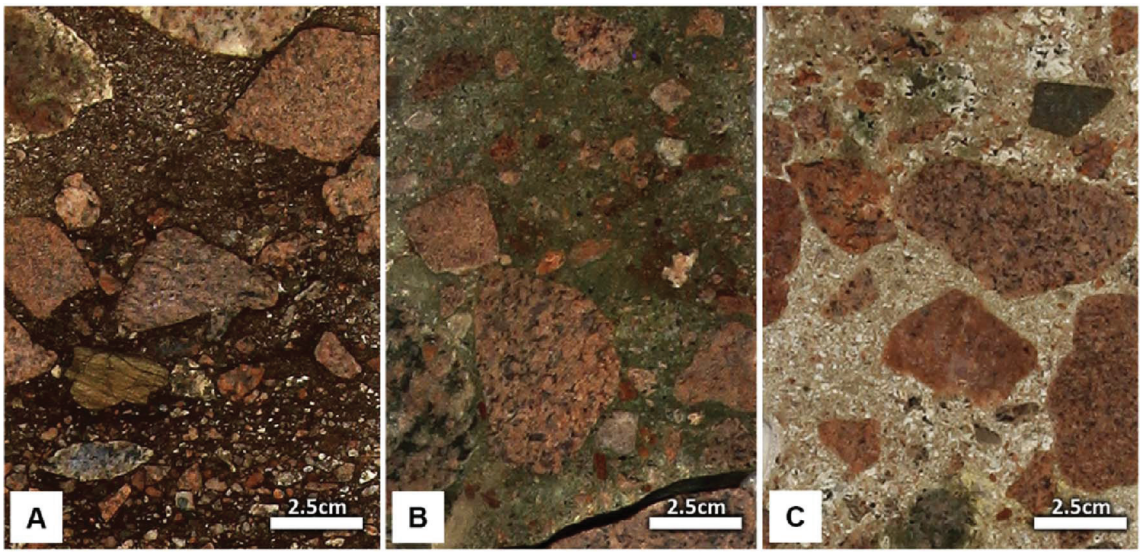

Fig. 6. (A) Example of red matrix type. The red-brown colour is Fe-oxide staining in clay-rich areas. The red matrix intervals are dominant in well 16/1–10 and to a small degree in wells 16/1–13 and 16/1–18 and have the lowest reservoir quality of all the four wells. (B) Green matrix intervals are generally associated with higher content of chlorite, which gives the green colour. (C) The grey matrix is the dominant matrix type in all four wells, and generally is the matrix type with the best reservoir quality. (For interpretation of the references to colour in this figure legend, the reader is referred to the Web version of this article.)

Micas are generally deformed and locally expanded and partially to wholly altered either to vermicular kaolinite or chlorite (Fig. 7A). According to the XRD analyses (Table 3), the highest content of kaolinite is found in the grey matrix of the conglomerates and in the sandstone/cross-stratified sandstone lithologies.

Detrital clays mainly occur as early grain-coatings, occasionally stained by Fe-oxides. Pseudomatrix, as defined by Dickinson (1970) as a discontinuous interstitial paste formed by the deformation of weak detrital grains, is rather problematic to distinguish from authigenic clays, due to limitations of the optical microscope. Minor occurrences of ductile rock fragments have been observed, represented by compacted and weakly degraded claystone and siltstone grains.

5.2.2. Authigenic mineralogy

The authigenic clay minerals have been determined by optical microscopy and SEM, as well as by bulk of whole rock and clay fraction (< 2 μm) XRD. The authigenic clay minerals are volumetrically variable and occur in several textures, as replacement of detrital grains, grain-coating clay, and pore-lining and pore-filling clays (Table 2). Replacive clays are generally observed in relation with the dissolution and alteration of unstable minerals in rock fragments, like feldspars and micas. Pore-filling and pore-lining clays were also identified in variable amounts in all the studied samples. Based on XRD and SEM analyses, these clays include chlorite, illite, mixed–layer I/S, mixed–layer C/S and kaolinite. The pore-filling clays locally choke the primary and secondary pores and pore throats, resulting in lower permeability.

Chlorite is common and appears in several textures as pore-filling clay, grain coating, replacement of micas, and less frequently of detrital grains. It displays usually flaky/webby morphology, similar to smectite, but may also show excellent euhedral rosettes or honeycomb texture (Fig. 8). Smectite is fully expandable to 17 Å. The sharpness of the XRD peak and the delicate nature of the clay flakes indicate an authigenic rather than a detrital nature. Diagenetic illite, based on SEM analysis, occurs either as fibrous or pore-bridging.

Table 3
Minimum, maximum and average bulk XRD mineralogy (weight %) of the main lithologies from the four wells. Note that the conglomerates are divided here based on the matrix colour to show the key differences (values in grey).

	Conglomerates									Sandstones					
	Grey matrix			Green matrix			Red matrix			Interbedded sandstone			Large scale cross-stratified sandstone		
	Min	Max	Ave	Min	Max	Ave	Min	Max	Ave	Min	Max	Ave	Min	Max	Ave
Quartz	22.9	46.0	30.3	9.0	34.6	26.2	22.1	32.6	28.5	33.2	66.7	45.1	38.7	73.0	59.8
Plagioclase	2.0	32.7	24.0	11.5	30.6	22.5	18.4	27.0	23.2	1.9	21.3	15.5	1.3	20.4	6.8
K-feldspar	11.7	29.0	20.2	12.7	26.8	19.6	16.8	26.6	19.7	8.0	20.8	15.9	9.0	18.5	13.1
Chlorite	2.4	9.7	5.3	**4.0**	**17.6**	**6.9**	3.4	7.7	4.8	2.0	11.9	5.7	1.2	7.0	3.9
Kaolinite	-	**5.7**	**1.7**	0.1	2.3	0.8	0.3	1.4	0.7	0.1	4.8	1.7	0.2	6.5	2.5
Biotite	0.1	3.6	1.9	1.4	2.9	2.2	1.4	2.8	1.9	-	2.8	1.6	0.0	2.8	1.5
Illite+Mica	0.6	23.8	4.6	0.7	12.0	4.0	1.1	12.5	6.1	0.4	11.2	5.8	3.0	7.8	5.0
Iron-oxide	-	-	-	0.2	2.6	0.6	**0.5**	**3.4**	**1.8**	-	-	-	-	-	-
Calcite	0.3	13.6	1.8	0.2	9.9	2.8	0.2	5.5	2.8	0.1	7.0	1.8	1.0	7.6	3.6
Dolomite	-	17.6	3.0	0.2	12.6	3.9	0.3	15.9	4.6	-	11.0	3.4	0.1	3.1	2.1
Smectite	0.1	14.3	7.1	**0.1**	**21.9**	**11.7**	1.2	10.2	7.2	-	15.4	4.1	-	6.7	2.5
Siderite	-	0.9	0.2	0.1	0.5	0.3	0.1	0.8	0.4	-	0.8	0.3	-	0.1	-

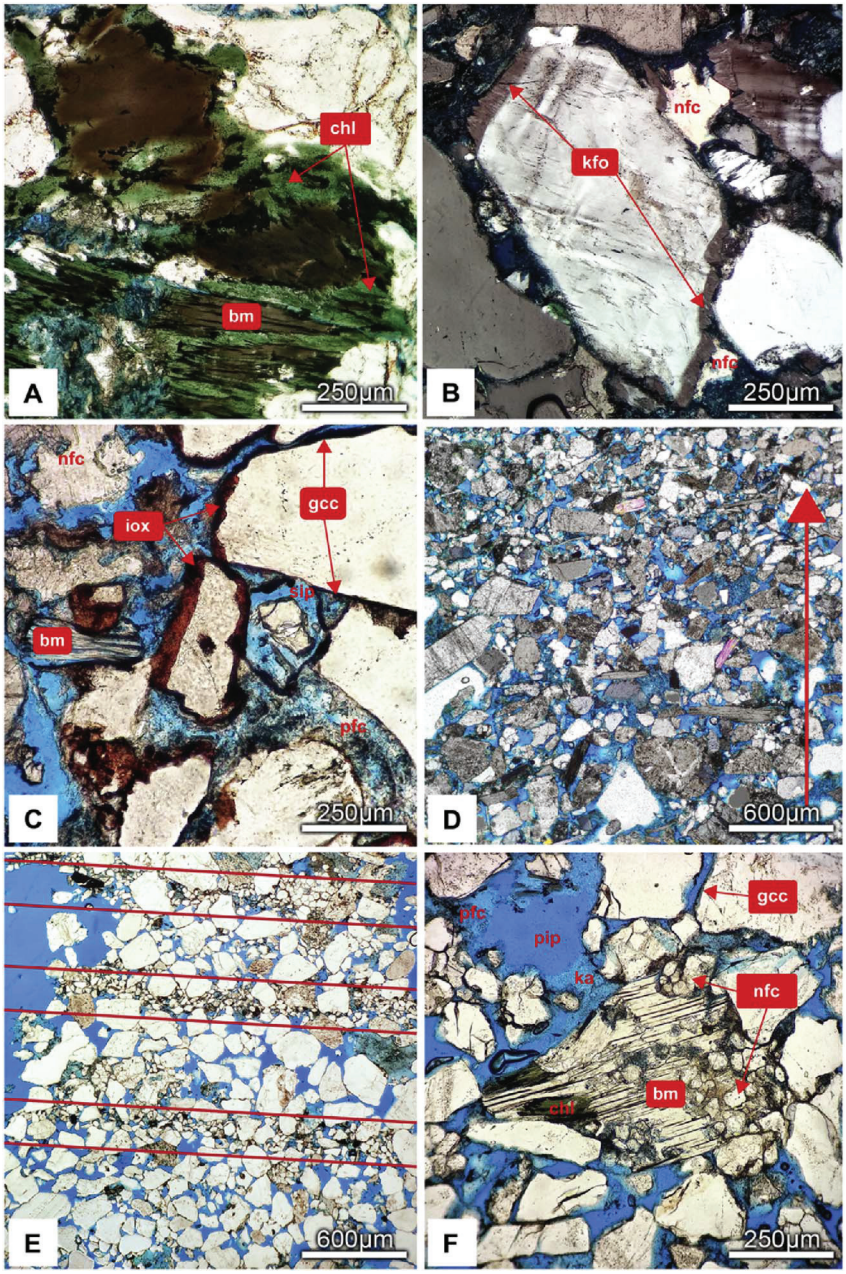

Fig. 7. (A) Close-up (10× PPL) view from well 16.1–13, 1979.25 m, of chlorite (chl) replacing biotite mica (bm). Small residual brownish patches of biotite still occur together with dark bits of titanite. (B) K-feldspar overgrowth (kfo) occluding primary pore space. Non-ferroan calcite (nfc) postdates the K-feldspar overgrowth. From well 16/1–13, 1974.80 m, 10× view under XPL. (C) Fe-oxide (iox) staining on the detrital grain coating clay (gcc) minerals. These clay minerals probably started as smectite. The pore-filling clays (pfc) postdate the hematite precipitation. The biotite mica grain shows deformation and is compacted between the ridged grains. 16.1–13, 1982.90 m, 10× PPL. (D) The sample is from a sandstone unit, 16/1–18, 1958.80 m, displaying upward-fining trend. The grains show weak horizontal alignment. 4× XPL. (E) Cross-stratified sandstone sample from well 16/1–13, 1924.75 m. Pinstripe lamination is present in-between the red lines, representing deposition of silt and very fine sand in the troughs of advancing wind ripples. 4× PPL. (F) The samples from well 16/1–13, 1952.50 m, illustrating kaolinite booklets choking primary intergranular pores (IGP) and enclosing optically non-resolvable pore-filling (pfc) and grain-coating clays (gcc), which are comprised of mixed-layer chlorite/smectite. Non-ferroan calcite (nfc) and chlorite (chl) are partially replacing dissolved biotite (bm). 10× PPL. (For interpretation of the references to colour in this figure legend, the reader is referred to the Web version of this article.)

Kaolinite is present in different amounts and often pre-dates carbonate cement, as seen in the SEM analysis. The kaolinite mostly occurs as a pore-filling phase, choking both primary intergranular and secondary intragranular pore space. Kaolinite often occurs mostly as thin vermicular finely stacked booklet type crystals (5–10 µm), but may sometimes show blocky to thick, well-developed crystals (Fig. 8C).

Carbonate cement plays a major role and occurs both as pore-filling and grain replacement phase. The carbonate cement is composed mainly of calcite and dolomite, with some minor amounts of siderite.

Dolomite is the most abundant carbonate cement phase in the conglomerate and interbedded sandstone units, 0.1–17.6% of total rock volume based on bulk XRD analysis (Table 3). Dolomite is generally very rare or totally absent in the large-scale cross-stratified sandstone units. In thin sections the dolomite is generally characterized by rhombohedral crystal forms. Occasionally calcite cement has been observed precipitated on the edges of dolomite (Fig. 9).

Non-ferroan calcite abundance is highly variable ranging from 0.1 to 13.6% in the siliciclastic deposits (Table 2). It occurs as intergranular cement, local poikilotopic or with blocky mosaic texture, as well as grain-replacive phase. It often encloses framework grains as well as their overgrowths, but also pore-filling/pore-lining clays. Patchy pore-filling carbonate cement has often been observed within secondary pores of dissolved K-feldspar grains.

K-feldspar overgrowth occurs in varying amounts (trace to 3%) based on point counting analysis. It occurs largely as euhedral crystals protruding into and occluding primary pore space (Figs. 6B and 7D). It usually grows on K-feldspar grains, and typically displays evidence of etching due to dissolution (cf. Fig. 8D). The K-feldspar overgrowths have similar elemental composition to the host grain.

Authigenic quartz is poorly developed in the studied samples and occurs in trace to minor amounts. It was observed both in SEM (Fig. 7F, H) and CL analyses, forming discontinuous euhedral crystals approximately 1–15 µm. Their further growth was probably hampered by the development of early authigenic clays, but also to relative low max burial temperature (~80° to 83 °C).

Minor authigenic albite occurs as euhedral overgrowths, generally

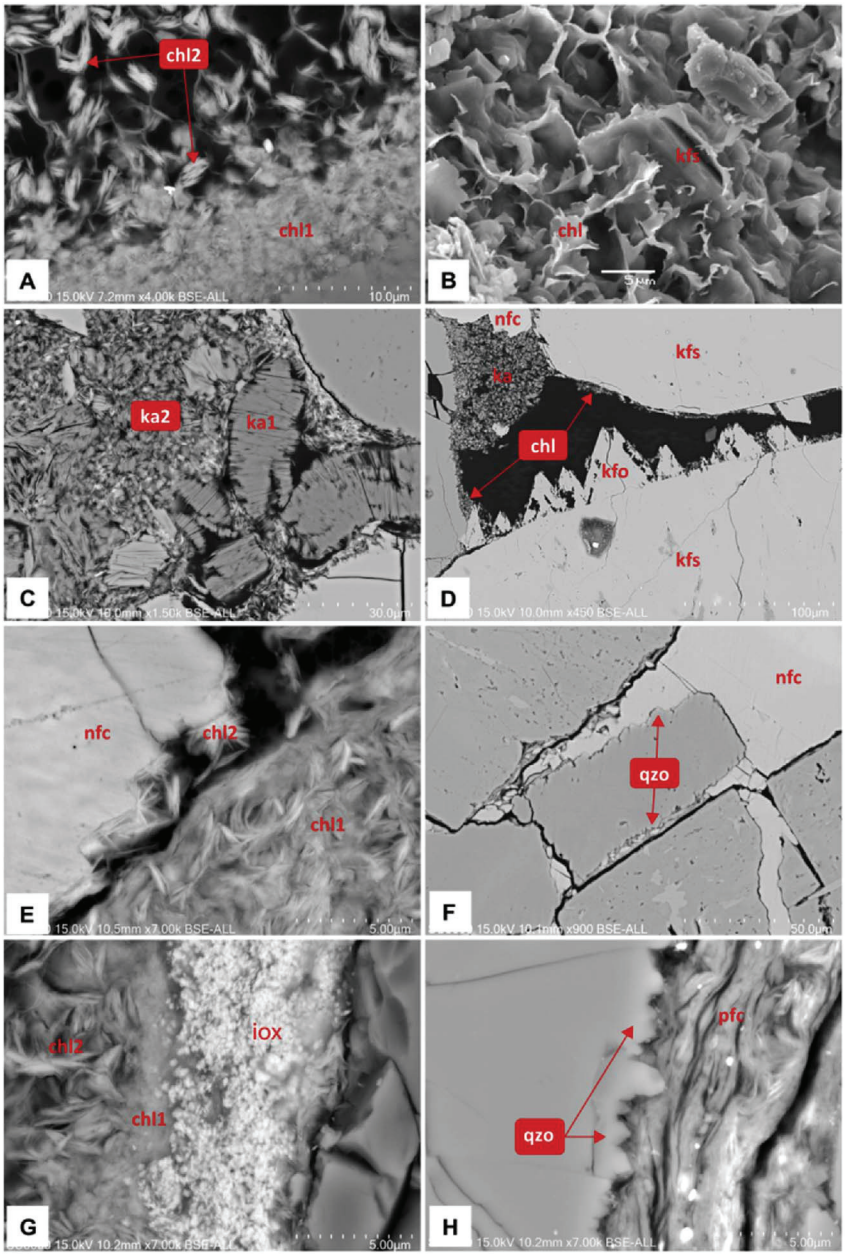

Fig. 8. (A) SEM image showing two generations of chlorite, chl1 (Mg-rich) and chl2 (Fe-rich). The first generation of chlorite (chl1) acts as grain-coating clay, generally displaying webby pore-bridging appearance akin to smectite. These may represent mixed-layer chlorite/smectite. The second generation (chl2) often shows well-formed rosettes and plates. (B) SEM image showing webby grain-coating chlorite surrounding K-feldspar grain. (C) Two sizes of kaolinite (ka1 and ka2) are present, both choking primary pore space. This may be due to space available for the kaolinite to grow and porewater circulation. (D) K-felspar overgrowth (kfo) shows dissolution and development of secondary porosity. Kaolinite (ka) is filling the primary pore space. (E) Fe-rich chlorite (chl2) is growing on non-ferroan calcite. Pore-filling clays are present, represented by Fe- and Mg-rich chlorite. (F) Non-ferroan calcite postdates quartz overgrowth. (G) Fe-oxide (iox) staining grain-coating chlorite (chl1). Fe-rich chlorite is present, but shows no hematite staining. (H) Quartz overgrowth (qzo) predates the porefilling clays (pfc).

precipitating on detrital plagioclase grains, and as intragrowths within dissolved plagioclase grains. Nucleation on K-feldspar grains has been confirmed by SEM analysis. Albite overgrowths surround earlier diagenetic phases, such as authigenic clay minerals, kaolinite and K-feldspar overgrowths.

Diagenetic Fe-oxide identification is generally based on optical and XRD analysis (Table 3), ranging from 0.2 to 3.4% of total rock volume, but may be locally abundant. Fe-oxide commonly coats and stains grain-coating clays (Fig. 7C).

Framboidal pyrite occurs in trace amounts (< 1%) and was only

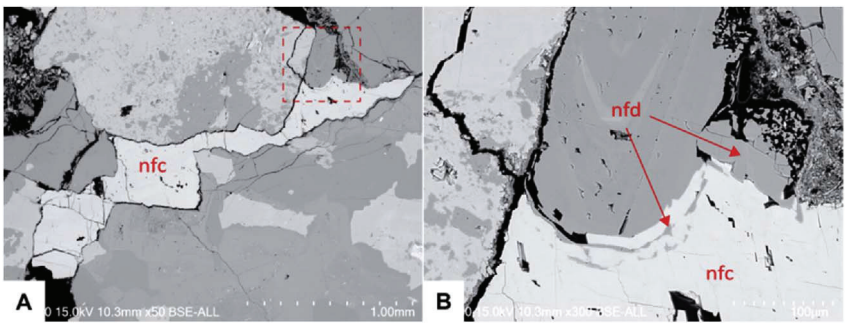

Fig. 9. (A) SEM images of non-ferroan calcite (nfc) and non-ferroan dolomite (nfd). (B) Suggests that the non-ferroan calcite probably nucleated upon dolomite.

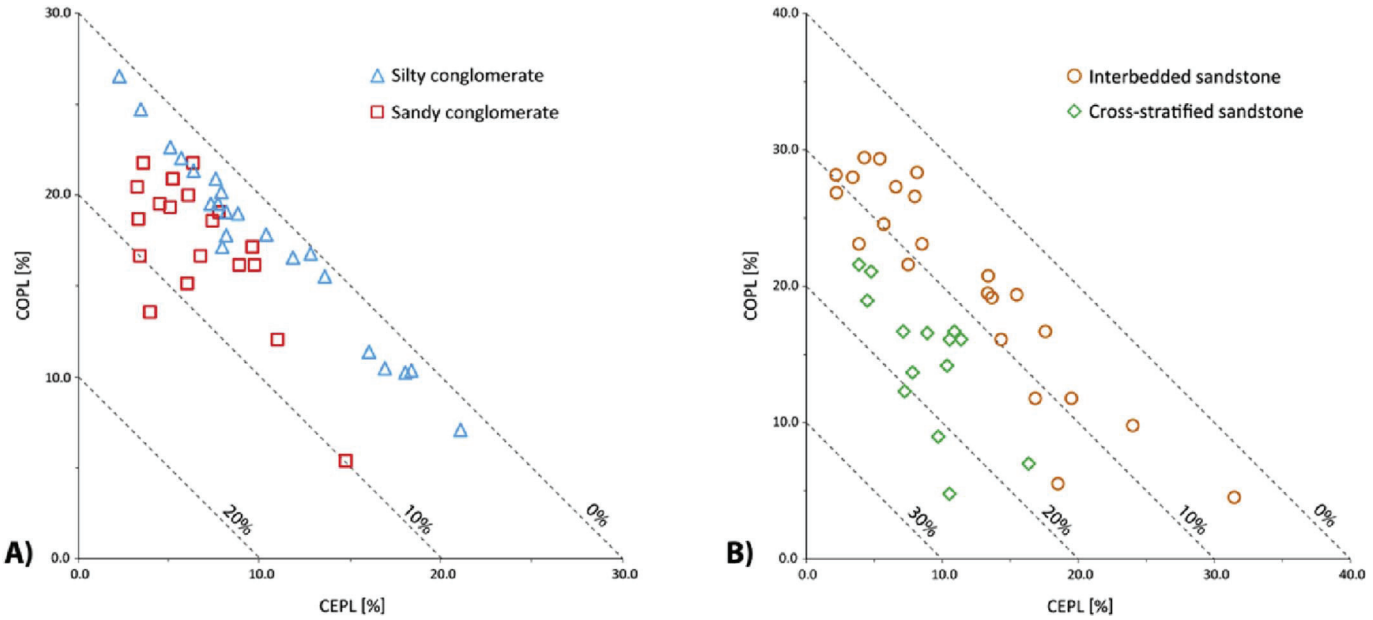

Fig. 10. Compactional porosity loss (COPL) and cementational porosity loss (CEPL) calculated according to Ehrenberg (1995). A) COPL-CEPL plot for the conglomerate units with initial porosity of 30%. B) COPL-CEPL plot for the sandstone units with initial porosity of 40%.

observed during SEM-imaging. Occasional tiny euhedral Ti-oxide (anatase) crystals have been observed in association with degradation of heavy minerals.

5.3. Compaction, primary and secondary porosity, and permeability

The sedimentary succession of the Edvard Grieg field reveals abundant evidence of mechanical and chemical compaction. These two groups of processes are responsible for the diagenetic history of the field, discussed in paragraph 6.1. The present section sets out the results of a range of analyses that have provided the basis for interpreting and reconstructing the diagenetic development.

Upon burial, sediments will compact mechanically when the effective stress is increased, resulting in porosity and total rock volume reduction (Bjørlykke, 2014). However, early cementation of the sediments, e.g. carbonate cement, may strengthen the grain framework and thus reduce the compaction. The mechanical compaction is typically associated with deformation of mica grains and mud clasts (which were later converted into pseudomatrix), as well as localized fracturing of quartz and feldspar grains, and grain reorientation and repacking. Based on the grain contacts, dominated by point and long-grain contacts, the compaction is assigned as weak to moderate.

Increasing burial depths and temperatures may trigger chemical compaction, involving dissolution and precipitation of minerals, thus resulting in reduced porosity and bulk volume, and increased rock density. In this dataset, chemical compaction is evidenced by quartz grain dissolution along grain contacts, and silica diffusion and re-precipitation as quartz overgrowths out of the grain contact area. Since silicate reactions are slow, temperature is very important for the onset of chemical compaction. Thus, whereas mechanical compaction will control porosity loss at shallow burial depths according to effective stress and the textural and mineralogical composition of the sediments, with increasing depths and burial temperatures (> 70–100 °C) chemical compaction will dominate porosity loss, and associated mineral reactions, e.g., quartz cementation and clay mineral alterations, will be controlled by thermodynamics and kinetics (Bjørlykke, 2014: Fig. 3).

5.3.1. Primary and secondary porosity

Primary intergranular porosity (IGP) is the main porosity type revealed by the investigations and varies widely throughout the studied samples. IGP is generally most abundant within the sandstone units, especially in the clean cross-stratified sandstone units, up to 26% (Table 2). In the conglomeratic matrix, the primary pore throats are significantly narrower due to the poor sorting and high proportions of authigenic clay minerals and cements. Compared to the conglomerate matrix, pore connectivity in the sandstones is better and the distribution of authigenic minerals, e.g. calcite and kaolinite, typically patchy.

Secondary porosity (i.e. intragranular porosity) is generally associated with partial to pervasive dissolution of detrital feldspar grains (plagioclase > potassium feldspar), either as single crystals or crystals within rock fragments, and ranges from trace amounts up to 7.5% (Table 2). Secondary porosity is also occasionally observed in K-feldspar overgrowths (Fig. 8D). Whole grain dissolution is often observed and the space commonly filled by clay minerals (e.g. kaolinite) and carbonate cement. There is a negative correlation between the amounts of clay minerals and carbonate cement. In samples with an abundance of detrital clays and pseudomatrix, the secondary pores are generally isolated from the primary pore space. However, in some cases secondary intragranular porosity can be connected to the primary pore network and thereby has increased the permeability. Minor porosity later developed from shrinkage of infiltrated clays, conversion of smectite into mixed-layer illite/smectite (I/S) and mixed-layer chlorite/smectite (C/S) (Moraes and De Ros, 1990), and possibly from dissolution of carbonate cement.

5.3.2. Intergranular volume (IGV)

The overall IGV in the four wells, which is the sum of intergranular pore space, intergranular cement and depositional matrix, ranges from 4.6 to 37% (Table 2), with highest values in part relate to precipitation of early carbonate cements (calcite and dolomite). The IGV values calculated from petrographic data together with total cement volume (CEM) data, can be used to quantify porosity loss due to mechanical compaction (COPL) and cementation (CEPL) (Fig. 10), after Ehrenberg (1995):

$$COPL = OP - \frac{(100\,x\,IGV) - (OP\,x\,IGV)}{(100 - IGV)} \quad (1)$$

$$CEPL = (OP - COPL) - \frac{CEM}{(IGV)} \quad (2)$$

where OP is the original porosity (initial or depositional porosity), here accepting 40% for the interbedded sandstone and large scale cross-stratified sandstone units and 30% for the silty and sandy conglomerate units (Beard and Weyl, 1973).

Both the mechanical compaction and cementation are important factors in porosity reduction. However, based on calculation of average values for COPL and CEPL (Table 1), the COPL is dominant for all four lithology units in the analyzed Edvard Grieg samples.

5.4. Mineral mapping and quantification of porosity loss

5.4.1. The silty conglomerate unit

The silty conglomerate matrix (Fig. 11A) displays a high degree of heterogeneity, generally associated with the poor sorting and large amounts of cements and authigenic minerals. Today's porosity is highly influenced by pore-filling/lining clay minerals and carbonate cements. The sample at level 1982.30 m from well 16/1–13 represents today's texture and mineralogy with feldspar (mostly plagioclase) grains partly or fully dissolved and replaced by clay minerals and carbonate cement. The present total optical porosity, i.e. intra- and intergranular porosity, calculated for the studied portion of the thin section is 7.9%. Pore-filling carbonate cement is responsible for only a minor part of the porosity reduction observed in this sample, 0.4% of the image area. The carbonate cement mostly occurs as grain-replacing phase, calculated to 1.4% of the total 1.8% carbonate cement.

The pore-filling and grain-coating authigenic clay minerals are calculated to be 7.2% of the image area. The total amount of pore-filling cement in the samples, i.e. carbonate cement and clay minerals, is 7.9% of the image area.

After removal of all the main diagenetic phases and secondary porosity, it was possible to restore what was probably the post mechanical compaction texture and primary intergranular porosity (12.4%), i.e. IGV value. The overall porosity loss due to the mechanical compaction (COPL) is calculated to be at 20.1%, while porosity loss due

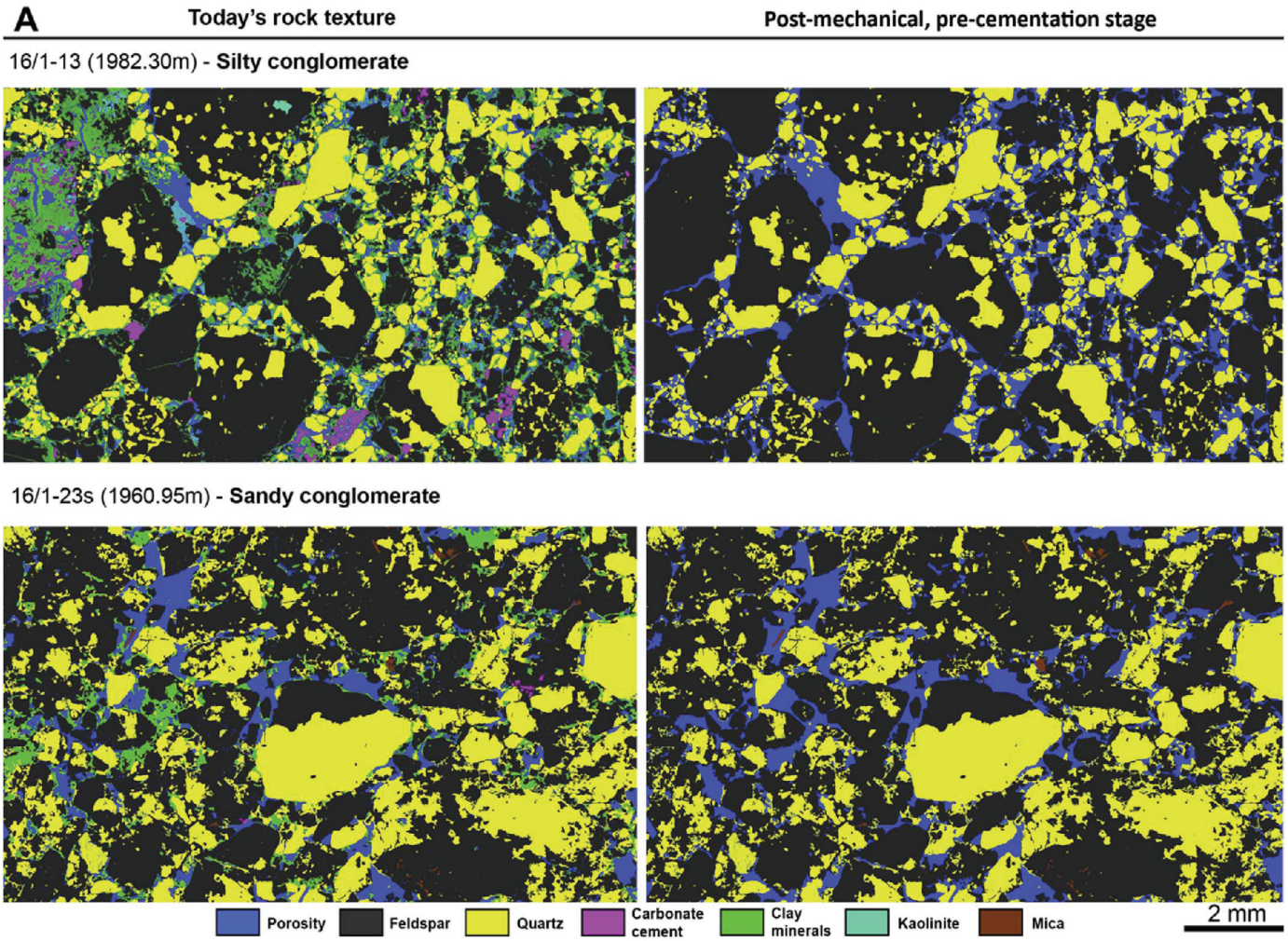

Depth_well	Stage	Total clay minerals	Total kaolinite	Total carbonate cement	Total pore-filling cement	Total porosity	Framework grains	Compactional porosity loss (%)	Cementational porosity loss (%)
1982.30_13	Post-mechanical, pre-cementation stage	-	-	-	-	12.4	87.6	20.1	6.3
	Today's rock texture	13.2	1.5	1.8	7.9	7.9	75.6		
1960p95_23s	Post-mechanical, pre-cementation stage	-	-	-	-	13.2	86.8	19.3	3.2
	Today's rock texture	6.1	-	0.9	3.9	10.1	82.9		

Fig. 11. (A) – Reconstruction of initial texture and mineralogy for the silty conglomerate (16/1–13 1982.30 m) and the sandy conglomerate (16/1-23s 1960.95 m). **Today's rock texture** showing the different mineral phases. The table shows total amount of each phase, i.e. pore-filling and replacive phase. The **compactional** and **cementational** porosity loss is calculated based on pore-filling and grain coating cements (i.e. authigenic clay minerals, carbonates and other type of cements).
(B) – Reconstruction of initial texture and mineralogy for the sandstone unit (16/1–13 1952.50 m) and the cross-stratified sandstone (16/1–13 1959.20 m). **Today's rock texture** showing the different mineral phases. The table shows total amount of each phase, i.e. pore-filling and replacive phase. The **compactional** and **cementational** porosity loss is calculated based on pore-filling and grain coating cements (i.e. authigenic clay minerals, carbonates and other type of cements).

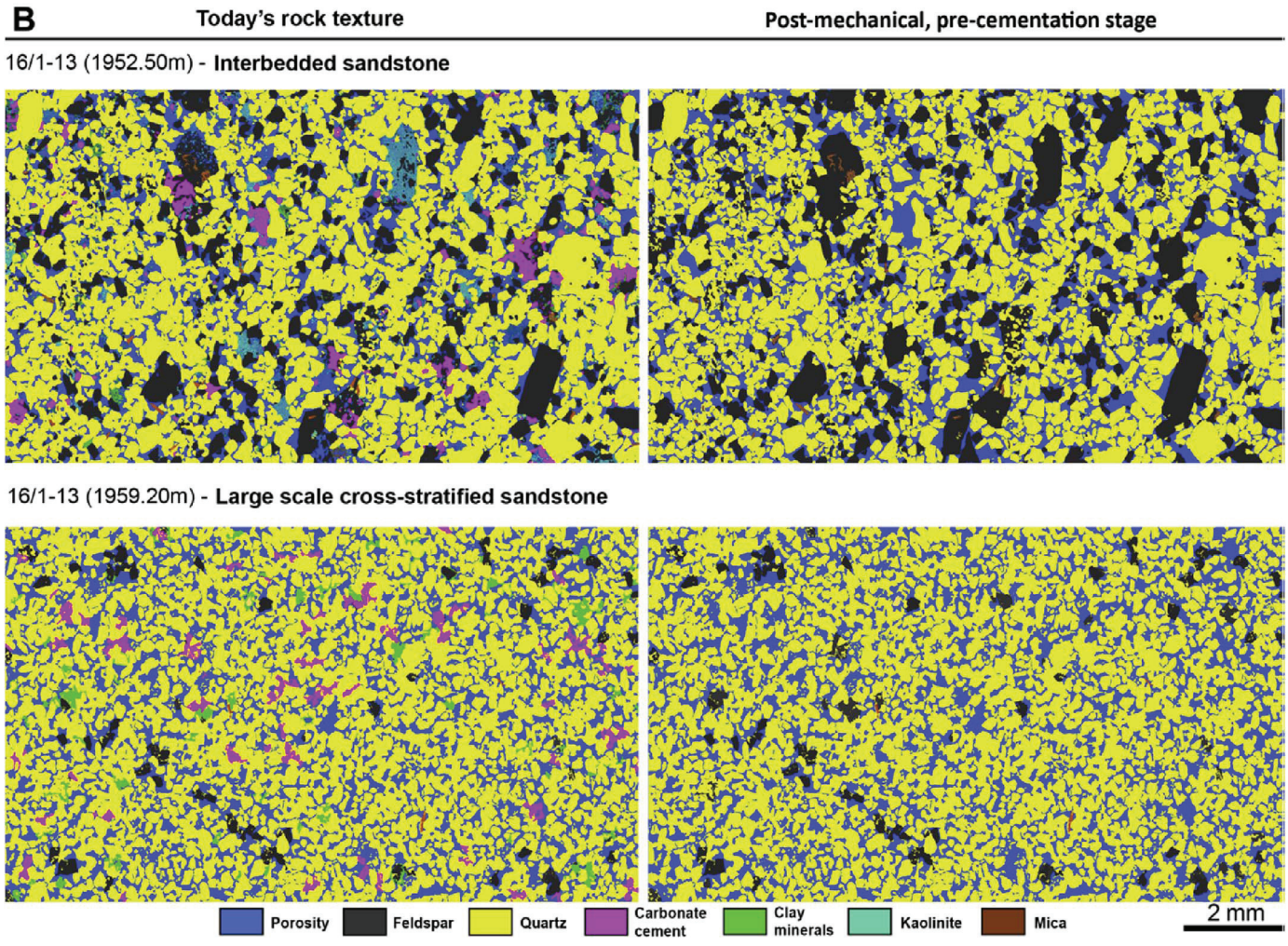

Depth_well	Stage	Total clay minerals	Total kaolinite	Total carbonate cement	Total pore-filling cement	Total porosity	Framework grains	Compactional porosity loss	Cementational porosity loss
1952p50_13	Post-mechanical, pre-cementation stage	-	-	-	-	21.5	78.5	23.5	5.0
	Today's rock texture	2.5	4.1	3.3	6.6	18.0	72.1		
1959p20_13	Post-mechanical, pre-cementation stage	-	-	-	-	30.1	69.9	14.2	4.5
	Today's rock texture	2.2	0.9	3.0	5.2	24.0	69.9		

Fig. 11. (*continued*)

to cementation (CEPL) is calculated to 6.3% of the original depositional porosity. These results are close to the point-counting values of 22.6% and 5% for mechanical and chemical porosity loss, respectively.

5.4.2. The sandy conglomerate unit

The sandy conglomerate matrix (16/1–13, 1960.95 m) displays the same high degree of heterogeneity as the silty conglomerate (Fig. 11A). However, in this sample the pore-filling authigenic clay minerals (3.9%) are only about half the amount found in the silty conglomerate. Pore-filling kaolinite and carbonate cement has not been observed. However, small amount (0.9%) of replacive carbonate cement is present in the sample (Fig. 11A). Total pore-filling cements are calculated to 3.9% of the image area. Today's total optical porosity calculated in the sandy conglomerate matrix is 10.1% of the studied thin section.

After removal of all the main diagenetic phases and secondary porosity, the primary intergranular porosity is 13.2%, i.e. IGV value. The overall porosity loss due to the mechanical compaction is 19.3%, while porosity loss due to cementation (CEPL) is calculated to 3.2% of the original depositional porosity. These results are very close to the point-counting values of 20.5% and 3.2% for mechanical and chemical porosity loss, respectively.

5.4.3. The interbedded sandstone unit

We used the same methodology on the interbedded sandstone from level 1952.50 m from well 16/1–13 (Fig. 11B). The sample displays much better sorting than the conglomerate sample. Quartz is the dominant framework mineral, followed by feldspar. This moderately well sorted sandstone is generally affected by pore-filling carbonate cementation (2.0% of the image area), and by grain-lining and pore-filling clay minerals (4.6%). The amount of total pore-filling cement in this sample is 6.6% of the image area. Today's total optical porosity is calculated as 18.0% of the image area.

After removal of all the main diagenetic phases and secondary porosity, it was possible to restore what was probably the post mechanical compaction texture and primary intergranular porosity (21.5%), i.e. IGV value. The overall porosity loss due to the mechanical compaction is 23.5%, while porosity loss due to cementation (CEPL) is calculated to 4.5% of the original depositional porosity. The point-counting values are 16.6% and 8.8% for mechanical and chemical porosity loss, respectively.

5.4.4. The large scale cross-stratified sandstone unit

The clean cross-stratified sandstone sample from level 1959.20 m

from well 16/1–13 (Fig. 11B), displays the best sorting of the selected samples. Quartz is the dominant framework mineral, with minor amounts of feldspars. This cross-stratified sandstone is affected by pore-filling carbonate cementation (2.5% of the image area), and almost equally by grain-coating and pore-filling clay minerals (2.7%). The total pore-filling cement in this sample is 5.2% of the image area. Today's total optical porosity is calculated to 24.0% of the image area.

After removal of all the main diagenetic phases and secondary porosity, it was possible to restore what was probably the post mechanical compaction texture and primary intergranular porosity (30.1%), i.e. IGV value. The overall porosity loss due to the mechanical compaction is calculated to be at 14.2%, while porosity loss due to cementation (CEPL) is calculated to 4.5% of the original depositional porosity. The point-counting values are 16.7% and 7.1% for mechanical and chemical porosity loss, respectively.

6. Discussion

6.1. Diagenesis

The diagenetic evolution appears to be very similar within similar lithologies of the four wells. Due to the absence of datings, the precise timing and duration of the individual diagenetic stages cannot be fully concluded. The reservoir properties are controlled by several distinct diagenetic modifications that have developed near-surface (early diagenesis) and during burial (late diagenesis). These key diagenetic modifications are discussed in the sections below.

6.1.1. Early diagenesis

6.1.1.1. Grain coating. During the early diagenetic regime, near-surface and early diagenetic processes took place, and the detrital minerals reacted with the circulating meteoric water and atmosphere. The sediments also underwent grain re-organization related to mechanical compaction.

The Triassic alluvial fan systems and aeolian deposits of the Edvard Grieg field (North Sea region) developed under an arid to semi-arid climate with periods of intense precipitation. Early infiltration of detrital clays, dominantly smectite (Chamley, 1989; Moraes and De Ros, 1990), were introduced to the sediments by wind and floods and formed thin coating around the detrital grains (Krinsley, 1998) (Fig. 12A). Inherited clay coating can be introduced to the sediments by water rich in suspended clay that percolates through the deposits. According to Moraes and De Ros (1990), the clay can be filtered out of the water and deposited as clay coatings on the grains. XRD of the clay fraction indicated the possible presence of trioctahedral smectite (saponite) (Fig. 13). Under semi-arid climate conditions with net evaporation, preferably in low-lying topography with poor drainage similar to the study area, meteoric water tends to be hypersaline and enriched with Mg^{2+} and SiO_2 which may produce trioctahedral smectite (e.g. saponite, sepiolite) and palygorskite (Beaufort et al., 1997; Mayayo et al., 2000; Wilson, 1999; Ryan and Hillier, 2002; Worden and Morad, 2003; McKinley et al., 2003; Worden and Burley, 2003). In contrast to the trioctahedral varieties, dioctahedral smectite and mixed-layer I/S form in environments that are less prone to evaporite formation (Worden and Morad, 2003).

The authigenic Fe-oxide staining of detrital clays was observed locally in well 16/1–10 and to a minor extent in 16/1–13 and 16/1–18 (Fig. 3). The alteration and dissolution of unstable detrital minerals (e.g. pyroxenes and amphiboles), and possibly biotite and chlorite, took place very early after deposition, through reactions with oxidant circulating meteoric waters (Ross, 1969; Acker and Bricker, 1992). Possibly during periods of droughts, evaporative concentration of the near-surface groundwater may have caused precipitation of authigenic Fe-oxides and minor amounts of titanium oxide (anatase). The presence of Fe-oxide generally is restricted to fine-grained conglomeratic matrix, especially where detrital clays are abundant, i.e. red matrix. Originally the distribution of Fe-oxide may have been more extensive in all the four wells during early diagenesis, as the typically observed red staining characteristic of a dry continental climate (e.g. Walker, 1967, 1976; Kessler, 1978; Burley et al., 1985).

Based on the XRD analysis Fe-oxides were observed in the green matrix as well, while totally absent in the grey matrix (cf. Table 3). From the petrographic analyses, the sandier grey matrix generally shows slightly better reservoir quality (i.e. porosity and permeability) compared to the green and red matrix. The bleaching of the sediments, which resulted in present day greenish and grey colours, may be due to mobilization and reduction of iron during burial by interaction with reducing fluids in relation to hydrocarbon migration, methane, organic acid or hydrogen sulphides (Surdam et al., 1993; Ormö et al., 2004). Bleaching of the sediments is dependent on the mobility of the iron, fluid composition and flow path. The latter is a function of permeability, lithology, sedimentology, stratigraphy and structure (e.g. Ormö et al., 2004; Busch et al., 2017). Pye and Krinsley (1986) discovered in the underlying Rotliegend aeolian sandstones (southern North Sea) three different pore-fluid regimes: (1) alkaline, oxidizing conditions during shallow to intermediate burial; (2) acid, reducing conditions during intermediate to deep burial; (3) alkaline, reducing conditions during deep burial and uplift.

6.1.1.2. Carbonate cement. The authigenic carbonates represent both replacive and pore-filling cement phases. They to some extend replace degraded and partly dissolved grains, (e.g. feldspars), and form cement filling both in inter- and intragranular porosities.

Based on XRD and SEM analysis, non-ferroan dolomite (except in core 16/1–13) is volumetrically the most dominant carbonate cement in the studied samples. The absence of iron in the dolomite can indicate deposition in O_2-rich waters. Dolomite is found to precipitate during times of high Mg^{2+}/Ca^{2+} and low Ca^{2+}/CO_3^{2-} ratios, high temperature, low salinities, and where fluids release CO_2 (Machel and Mountjoy, 1986), indicating a Mg-rich groundwater at the time of dolomitization (Fig. 14). This dolomite might have started as phreatic dolocrete which could typically be formed by three major processes (Wright and Tucker, 1991); 1) evaporation and evapotranspiration of mobile, shallow groundwater, 2) CO_2 degassing, and 3) dissolution of feldspar and clays. Exactly which of these explanations are preferable for dolomite growth is uncertain, but the arid to semi-arid climate during the Triassic may have caused extensive surface water evaporation and concentration of Mg^{2+}.

Carbonate cementation typically formed poikilotopic crystals that largely impeded compaction, suggesting that its precipitation occurred very early during diagenesis. Blocky non-ferroan calcite has also been observed to extensively replace ductile grains (e.g. mica) and igneous rock fragments. The calcite shows deformation between rigid framework grains (Fig. 7F) suggesting that it precipitated prior to the main phase of compaction, resulting in a chaotic arrangement of blocky crystals. Evidence of early diagenetic origin of the carbonate cements are: 1) the homogeneous chemical composition of the carbonate cements, with very low iron, suggest oxidizing meteoric water composition (Morad et al., 1990a); 2) high IGV values (> 25%) (Fig. 10) indicate early precipitation of carbonate cement; 3) traces of etched non-ferroan calcite and dolomite observed in SEM analysis; and 4) Fe-rich chlorite platelets have been observed to precipitate on calcite cement (Fig. 8E). However, SEM and optical microscope analyses show that carbonate cement generally postdates grain-coating clays.

The source of the calcium carbonate ($CaCO_3$) may have been introduced to the Edvard Grieg deposits by water- or wind-borne carbonate dust from adjacent carbonate-rich playa lakes (Lattman, 1973). Possible evidence of ephemeral pond or lake deposits has been observed in the cores. The distribution of carbonates in alluvial fans systems can also be explained based on the hydrological pattern (Nickel, 1985). Rivers and groundwater in highlands generally contain very low salinities. Further downfan the salinity of the river and groundwater may

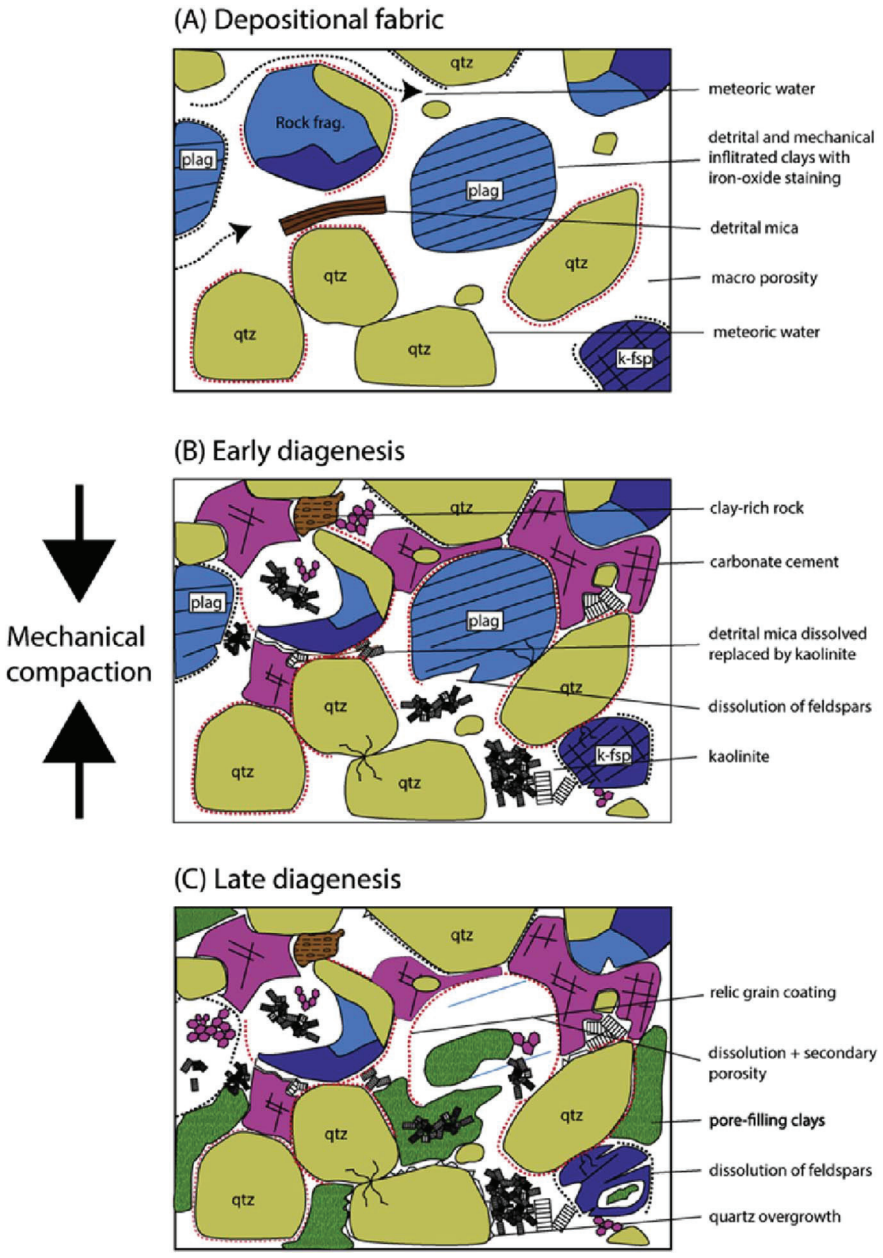

Fig. 12. General schematic cartoon illustrating mechanical and chemical compaction in Edvard Grieg samples. (A) At time of deposition, mechanically infiltrated clay minerals may stick to framework grains. Fe-oxide staining occurred at this time. These coating clays formed precursors to later pore-filling and pore-lining clay minerals. (B) Grain repacking, rotation, and brittle grain fracturing. Early carbonate cement precipitated also at this time, typically forming poikilotopic crystals. (C) Further increase in pressure, temperature and porewater chemistry led to further dissolution of unstable minerals and precipitation of pore-filling clay minerals and cements.

increase, e.g. due to the weathering reactions in the aquifer. With annual net evaporation in arid and semi-arid regions, these waters may initiate the precipitation of phreatic cement (Nickel, 1985). Carbonate cement, such as calcrete and dolocrete, may also form as vadose (pedogenic) cement, linked to soil formation (Wright and Tucker, 1991). The logged cores from the Edvard Grieg field lack any unequivocal evidence of pedogenic modification, suggesting either that there were no long-lived exposure events, or perhaps more likely, that the cored section records deposition by high energy depositional events with sufficient erosive capacity to remove any finer grained sediments that may have accumulated during quiescent periods.

6.1.1.3. Authigenic kaolinite. During early diagenesis, slightly acidic waters may have been involved in minor alteration and dissolution of silicate grains, e.g. feldspar and mica. Liberated ions such as Al and Si may have resulted in the precipitation of comparable amounts of authigenic kaolinite (Reactions 1 and 2) (Fairbridge, 1967; Lanson et al., 2002). These reactions take place near the surface where meteoric water is required to supply H^+ and remove the reaction products such as Na^+ and K^+ (Hancock, 1978; Hancock and Taylor, 1978; Bjørlykke, 1998). XRD and petrographic observations indicate that the distribution and amount of kaolinite in the Edvard Grieg deposits may be facies controlled. The silty conglomerate contains the least amounts of kaolinite compared to the other more sandy units (Tables 1 and 2). Minor occurrence of early diagenetic kaolinite has occasionally been observed within expanded mica (e.g. biotite) grains (Fig. 15). Kaolinised micas generally show expanded textures (Ketzer et al., 2003; Morad et al., 2010) which indicate that kaolinisation took place before significant burial. Furthermore, precipitation of carbonate cement around kaolinite crystals (Fig. 16) suggests early kaolinite

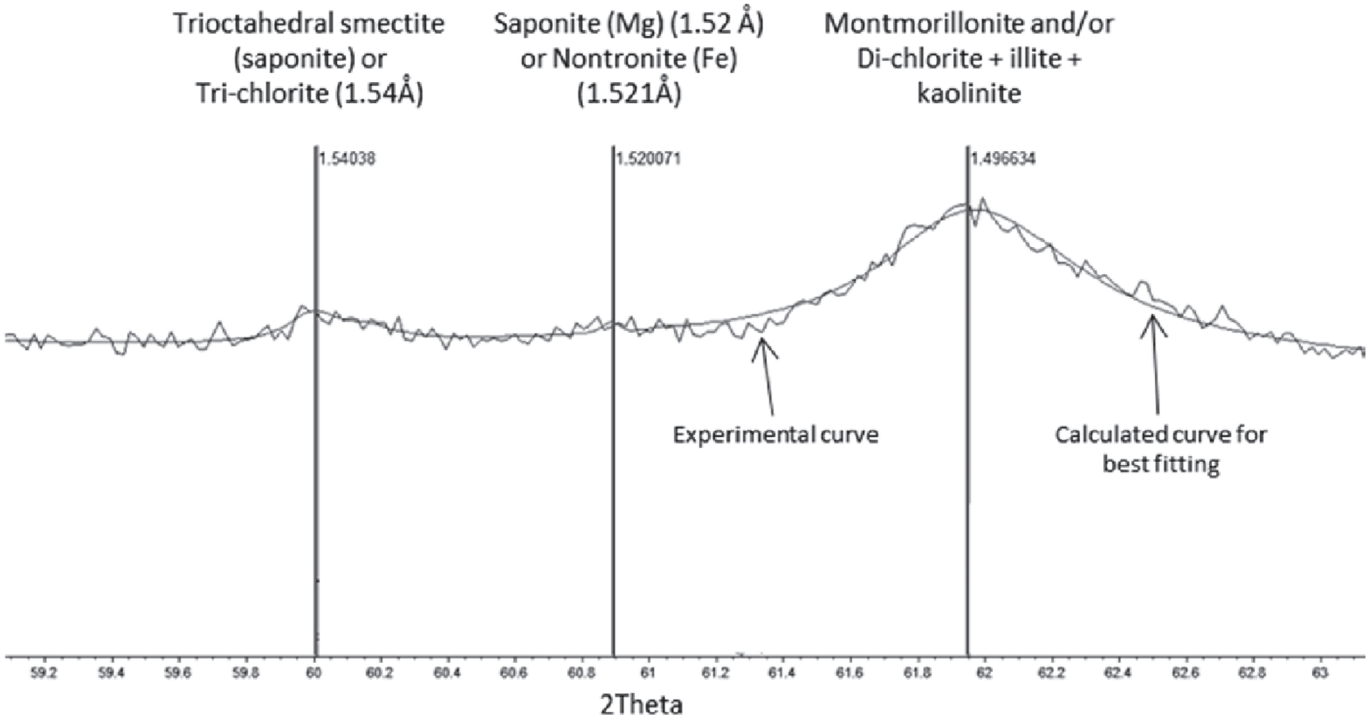

Fig. 13. X-ray diffractogram (060 peaks) of silty conglomerate (16/1–13, 1995.65 m) showing possible trioctahedral smectite (saponite) at 1.54 Å.

development.

$$\underset{\text{K–Feldspar}}{2K(Na)AlSi_3O_8} + 2H^+ + 9H_2O \leftrightarrow \underset{\text{Kaolinite}}{Al_2Si_2O_5(OH)_4} + \underset{\text{Dissolved silica}}{4H_4SiO_4} + 2K^+(2Na^+) \quad (3)$$

$$\underset{\text{Mica}}{2KAl_3Si_3O_{10}(OH)_2} + 2H^+ + 3H_2O \leftrightarrow \underset{\text{Kaolinite}}{3Al_2Si_2O_5(OH)_4} + 2K^+ \quad (4)$$

The replacement of the early vermicular kaolinite with the more block morphology observed during SEM analysis, began probably during higher temperatures (< 80 °C) and porewaters with low K^+/H^+

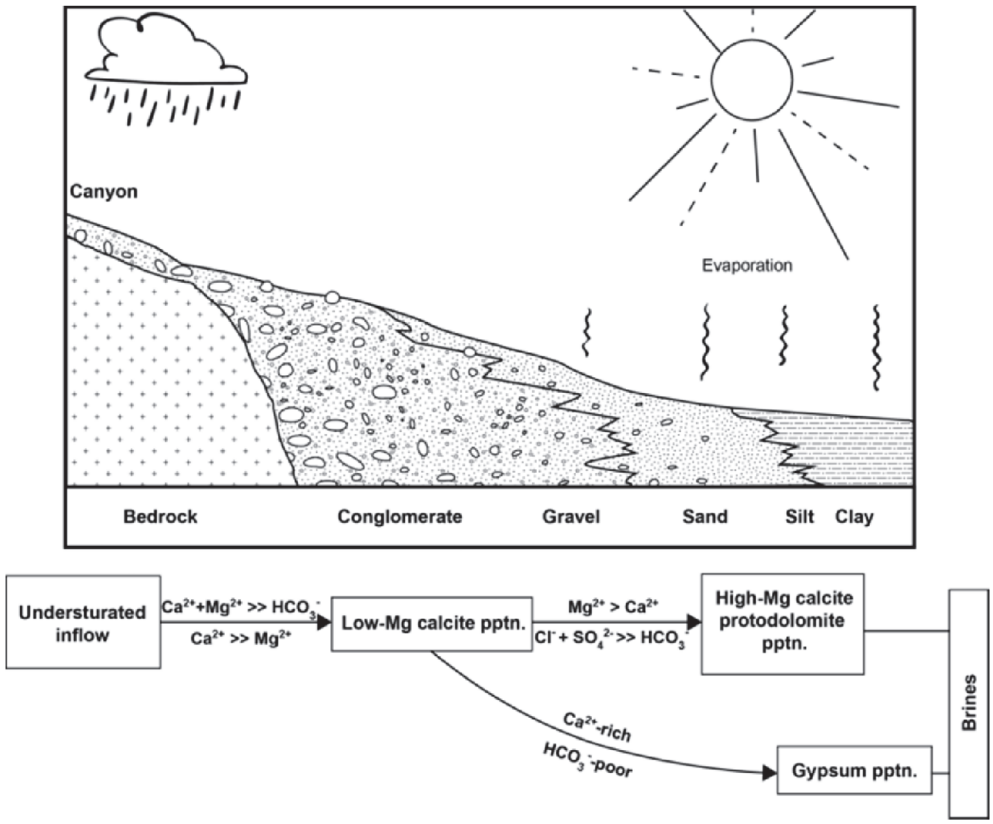

Fig. 14. Conceptual model of alluvial-fan zonation with the evolution of carbonate-sulphate brines from proximal to distal areas in an alluvial-fan system (Modified from Nickel, 1985).

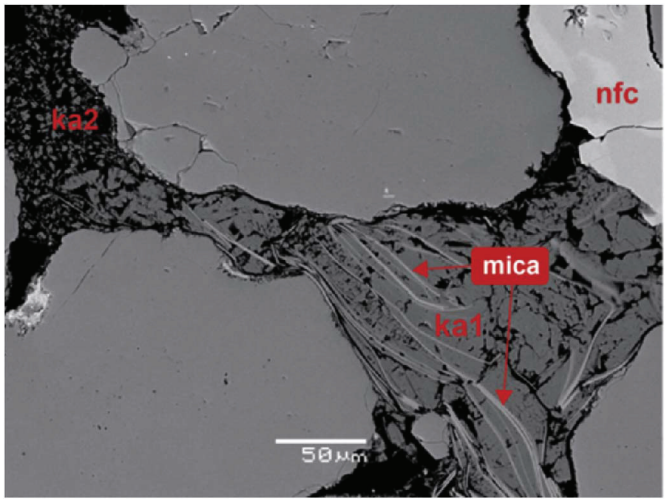

Fig. 15. SEM-BSE images of large vermiform kaolinite (ka1) in-between mica sheets. Kaolinite likely nucleated upon mica originally. The smaller blocky kaolinite (ka2) consists of euhedral, sub-hexagonal plates. Non-ferroan calcite (nfc).

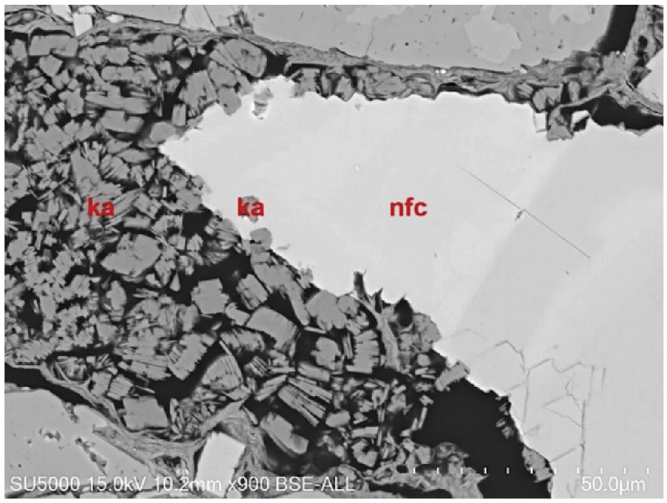

Fig. 16. SEM-BSE images of non-ferroan calcite (nfc) surrounding kaolinite (ka).

ratios. Similar kaolinite transformation has been observed in the Skagerrak Formation from the Danish Sub-basin (Weibel, 1999) and Brent Group, UK North Sea (Osborne et al., 1994).

6.1.1.4. K-feldspar cement. Early diagenetic precipitation of K-feldspar overgrowth is common in the area (e.g. Riber et al., 2015), but minor cement requires high silica activity and K^+/H^+ ratios (Morad et al., 2000; Rossi et al., 2002; Schmid et al., 2004). The origin of early K-feldspar has been much debated over the years (e.g. Morad et al., 1989) since it is a regular, minor, early cement in aeolian and ephemeral river sediments. Bjørlykke et al. (1986) concluded that formation of authigenic K-feldspar in the Jurassic sandstones in the Haltenbanken area (north of the North Sea) occurred at temperatures < 50 °C. Since the authigenic K-feldspar predates significant burial, an internal source such as compaction and pressure solution is less likely. Authigenic kaolinite and K-feldspar overgrowths may form at the same time in a closed system below 50 °C if muscovite is present and minimum silica supersaturation with respect to quartz is in the pore fluid. The overall reaction is:

$$\underset{\text{Mica}}{KAl_3Si_3O_{10}(OH)_2} + 2SIO_2(aq) + H_2O \leftrightarrow \underset{\text{K–feldspar}}{KAlSi_3O_8} + \underset{\text{Kaolinite}}{AI_2Si_2O_8(OH)_4} \quad (5)$$

In summary, the early diagenesis of the Edvard Grieg deposits was characterized by grain-coating Fe-oxides, microcrystalline and poikilotopic carbonates (dolomite and calcite), K-feldspar overgrowths and kaolinite precipitation. The early cement paragenesis observed in Edvard Grieg deposits is typical of diagenesis in semi-arid fluvial sediments (Colson and Cojan, 1996).

6.1.2. Late diagenesis

With further burial and higher temperatures the Edward Grieg field deposits moved into the late diagenetic regime as the system became isolated from surface (meteoric) water. The chemical compaction resulted in further dissolution and was followed by precipitation of cements and authigenic clays. Early diagenetic carbonate cement had an important role in constraining mechanical compaction during the late diagenetic phase. The maximum temperature for the studied wells ranges from 81° to 83 °C, based on average geothermal gradient of 40.5 °C from the wells. This geothermal gradient fits well with observed gradients in the North Sea, ranging from 30 to 40 ^{O}C (Bjørlykke et al., 1995).

6.1.2.1. Illitization of smectite. Pore-filling and pore-lining clays were observed in all the studied samples during SEM analysis: chlorite, illite, mixed-layer C/S and mixed-layer I/S. The precursor detrital clay for these authigenic clays was probably early stage smectite, and other Mg-Fe-rich clays which developed during early diagenesis under warm, arid to semi-arid conditions (Hillier, 1994; Hillier et al., 1996; Morad et al., 2000; Worden and Morad, 2003).

In the presence of K^+, illitisation of smectite (dioctahedral) probably took place developing mixed-layer I/S (Dypvik, 1983; Bjørlykke, 1998; Worden and Morad, 2003) as observed during SEM analysis. This reaction is strongly controlled by temperature, begins at 60° to 80 °C (Nadeau et al., 2005), and extent of potassium supply where dioctahedral smectite transforms gradually to illite.

Smectite + Al^{3+} + K^+ → illite + Si^{4+} (Hower et al., 1976; McKinley et al., 2003) (6)

Smectite + K-feldspar → illite + chlorite + quartz (McKinley et al., 2003) (7)

Albitisation of K-feldspar is a possible source of potassium for the illitisation process. Direct replacement of K-feldspar by albite can be expressed by the reaction:

$KAl\ Si_3O_8 + Na^+ \rightarrow NaAlSi_3O_8 + K^+$ (Saigal et al., 1988) (8)

6.1.2.2. Formation of chlorite. There are two types of chlorite in the Edvard Grieg samples: 1) Mg-rich chlorite coating (Fig. 8A – chl1) linked to early, mechanically infiltrated coatings during early diagenesis; 2) late diagenetic well-developed pore-filling Fe-rich platelets/rosettes (Fig. 7E, G – chl2). Boxwork and honeycomb-like pore lining patterns have also been observed; these could represent smectite-to-chlorite intermediate stages, with trioctahedral smectite as the precursor mineral developed during shallow burial. Possible trioctahedral smectite has been observed in clay fraction XRD analyses. The neoformed chlorite coatings usually have porosity preserving potential, since they can contain substantial micro-porosity between the chlorite grains while inhibiting the formation of quartz overgrowth (Hillier, 1994).

Fe-rich chlorites often develop in marine environments, while the more Mg-rich varieties are common in arid to semi-arid environments (Hillier, 1994). The chlorite platelets analyzed here display high Fe/(Fe + Mg) ratios of > 0.8, which may indicate the presence of interstratified chlorite/berthierine (Ryan and Hillier, 2002); the Fe-rich end member being chamosite (Humphreys et al., 1989). Jahren and Aagaard (1989) proposed that the both chemically and structurally unstable berthierine recrystallised to more stable chamosite around

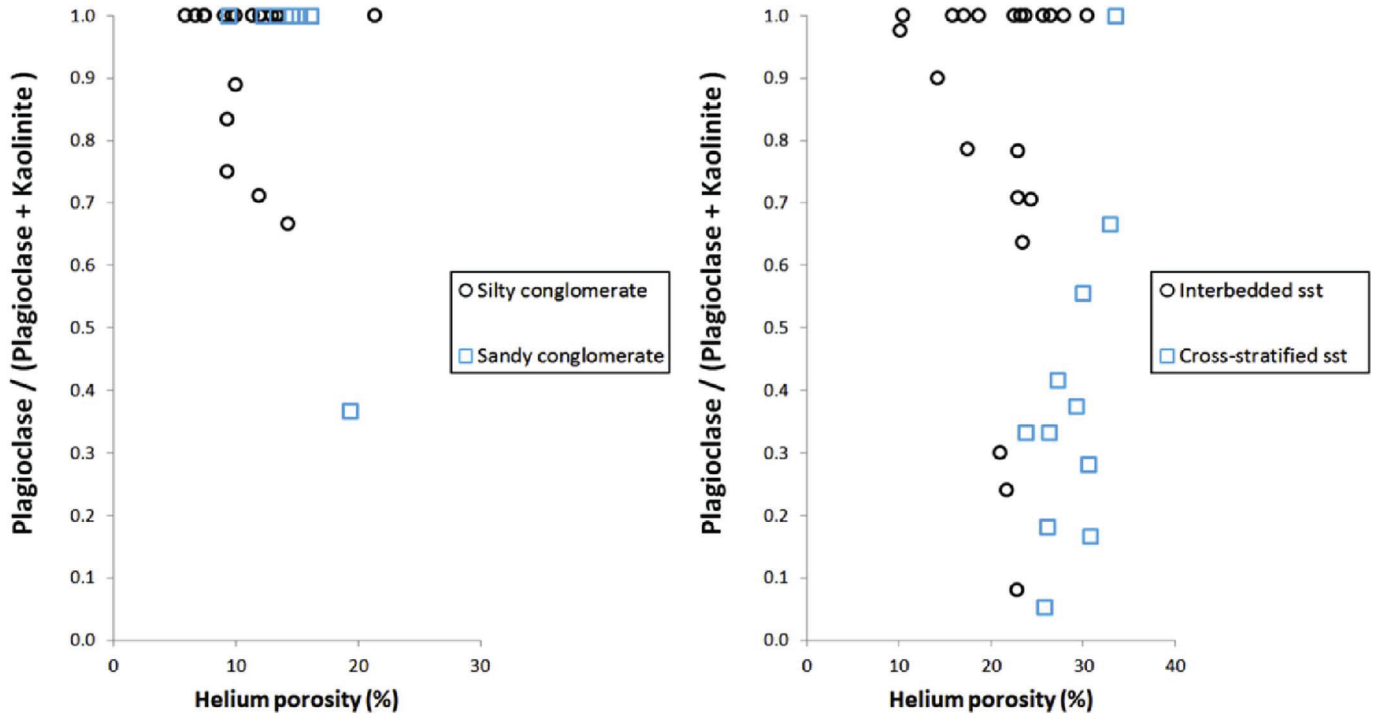

Fig. 17. Petrographic results of plagioclase/(plagioclase + kaolinite) vs helium porosity. Slight increase in helium porosity when kaolinite content increases and plagioclase content decreases in the conglomerate and interbedded sandstone samples. The cross-stratified sandstone show an inverse trend, where helium porosity decreases with increased kaolinite content.

70 °C. The Fe-rich precursor mineral in the Edvard Grieg deposits, e.g. berthierine or odinite, may have been formed at near-surface conditions associated with marine and meteoric water mixing zone (Humphreys et al., 1989; Hillier, 1994) during the Jurassic marine transgression. Ehrenberg (1993) suggested that Fe-rich chlorite coatings in marine sediments from the North Sea developed from synsedimentary enrichments of Fe-rich clay mineral precursors in a freshwater-influenced shallow marine setting.

6.1.2.3. Quartz cement. At higher temperatures, above 70-90 °C, the porewater is close to equilibrium with quartz (Bjørlykke, 2014) and precipitation of quartz overgrowth may have taken place (Wilkinson and Haszeldine, 2002). The amounts of quartz cement in the studied samples is generally below 1%, and mostly occurs as microquartz precipitating on grains under clay coatings (Fig. 8H). Similar microquartz development below chlorite coatings have also been observed in more deeply buried sandstones (e.g. Ajdukiewicz and Larese, 2012). The low max temperature (~81–83 °C) of the studied Edvard Grieg deposits, together with early infiltrated clay coatings (e.g. chlorite and iron oxide coating) probably inhibited further quartz cementation (Ehrenberg, 1993; Ajdukiewicz et al., 2010; Taylor et al., 2010; Busch et al., 2017), along with pervasive cementation of early diagenetic carbonate cements. Quartz cementation generally pick up around 70 to 80 °C, starting first with low rates and increasing with higher temperatures (e.g. Walderhaug, 1994; Worden and Morad, 2003; Bjørlykke, 2014). Relative low amounts of quartz cement (< 5%) has been found in deeper Skagerrak Formation of the Heron Crater, North Sea (Stricker et al., 2016). The author argued that clay coating (chlorite and mixed chlorite/illite), microquartz coating and overpressure were probably the main mechanisms inhibiting quartz cementation despite elevated temperatures (up to 180 °C). Possible internal silica sources can include intergranular pressure dissolution, smectite illitisation or kaolinite illitisation. Only the former has been observed in the studied samples. However, the dissolution of Ca-rich plagioclase and the precipitation of albite may have consumed dissolved silica at temperatures lower than 90 °C, which may have contributed further grain-contact quartz dissolution (Schmid et al., 2004).

6.2. Impact of compaction and cementation on reservoir quality

Depositional facies and climate have a significant control on the distribution of early diagenetic and late diagenetic alterations (Morad et al., 2000, 2010). The initial framework grains, grain size and sorting, and matrix content, will have considerable influence on porosity and permeability developments through burial. The diagenetic events, such as dissolution of unstable grains and precipitation of clay minerals, pseudomatrix generation and carbonate cement, also strongly influenced the evolution of reservoir quality in the Edvard Grieg field. It is important to note that the occurrence of all these different diagenetic phases, vary significantly between the individual lithologies which can have a significant impact on the final reservoir quality.

Plotting COPL vs. CEPL (Fig. 10) shows that in the Edvard Grieg deposits mechanical compaction has had a greater effect than cementation on the main porosity reduction. High IGV values reflect early carbonate cement, which reduced the effect of mechanical compaction. The mechanical compaction caused by lithostatic overburden led to the reorientation and repacking of grains and to the reduction of the bulk volume which is characterized entirely by the reduction of the IGV. The reduction of the IGV caused by mechanical compaction from the initial 40% of loose sand is limited to 26% characterizing the arrangement of an ideal sphere packing (Houseknecht, 1987). Note that the estimated initial values of porosity in this study has been estimated in 30% for the conglomeratic units, and 40% for the sandstone units, due to poorer sorting of the conglomeratic units as compared to the sandy units. Further reduction of the IGV can only be achieved through chemical compaction (i.e. grain dissolution) at point contacts. Sandstones with higher amounts of ductile grains, e.g. micas, will tend to experience more compaction than rigid-grain deposits (Rittenhouse, 1971).

Cements and authigenic clay phases had a major impact on the reservoir quality of the Edvard Grieg field by their effect on porosity and permeability evolution. The reduction of primary porosity is mostly caused by development of pore-filling clay minerals and carbonate

cementation. The secondary porosity in the samples is generally associated with dissolution of feldspars. These secondary pores are commonly filled by kaolinite, to a lesser extent, by other replacive clays and carbonate cement. Petrographic observations of conglomerate and interbedded sandstone samples generally have a slight increase in helium porosity with increasing kaolinite and decreasing plagioclase content (Fig. 17). However, the large scale cross-stratified sandstone samples have an opposite trend, where helium porosity decreases with increasing kaolinite content. This implies that the reservoir quality is reduced in the cross-stratified sandstone samples due to kaolinite precipitation, whereas slightly increased in conglomerates and interbedded sandstone samples. There is no direct linear correlation between decreasing plagioclase and increasing kaolinite content in the different lithology units, which means that kaolinite precipitation probably resulted from different processes, e.g. dissolution of micas, and not exclusively derived from post-depositional feldspar dissolution. Furthermore, depositional plagioclase content could also have been variable between the different lithological units. Similar observations were made for the Brent Group sandstone of Gullfaks Field (Ehrenberg and Jakobsen, 2001). Secondary porosity is often enclosed by relic grain-coating clay minerals that preserve the grain boundaries. Even if these authigenic clay minerals, e.g. chloritic and illitic grain coatings, might contain significant microporosity, the permeability will generally decrease drastically due to occluded pore throats. Study by Nadeau et al. (2005) showed that transformation of smectite to illite (60° to 80 °C) within shale pore system had a rapid and severe permeability reduction at the onset of this reaction. The formation of fluid overpressure and hydrocarbon occurrence at or above these temperatures also increased exponentially. Secondary porosity rarely has beneficial effects on reservoir quality, since material from dissolved minerals will commonly precipitate somewhere else (Bjørlykke, 1984). Quartz overgrowth is not volumetrically important in relation to porosity loss in the Edvard Grieg deposits, but may affect the permeability by obstructing pore throats.

6.2.1. The silty and sandy conglomerate units

The poor sorting within the highly heterogeneous conglomerates appears to be the main control of reservoir quality in these lithologies, but carbonate cement, generation of pseudomatrix and precipitation of the authigenic clay minerals also display significant effects on the quality. In the silty conglomerate samples the porosity decreased from assumed initial 30% to present 7.9% as measured by image analysis in thin section (Fig. 11A), due to a combination of compaction and cementation processes. The early, primary grain coating clay minerals probably had porosity-preserving effects, inhibiting possible later effects of mechanical compaction and cementation, e.g. prohibiting later stage quartz cementation. These grain-coating clays were probably detrital, such as smectite. These pore-filling clay minerals might block the pore throats, and hamper porewater flow, thereby prohibiting precipitation of carbonate cement. This would explain the negative correlation observed between the clay mineral content and carbonate phases. Well 16/1–10 samples have the highest proportion of the red matrix conglomerate (Fig. 3); this generally displays the lowest porosity and poorest reservoir quality, likely related to the higher abundance in detrital clays in these intervals. The reservoir quality of the conglomerate dominated intervals is low and very low in the red matrix intervals. However, the sandy conglomerate units (Fig. 3) observed in well 16/1–18 and 23S have better reservoir quality due to higher average porosity, better sorting and lower amounts of carbonate cement (Table 2).

6.2.2. The interbedded sandstone unit

In the sandstone-dominated units observed in all four wells (Fig. 3), the reservoir quality is increased compared to the conglomerates due to better sorting (Fig. 11B). While compaction is the dominant porosity reducing mechanism, carbonate cement and authigenic clay minerals also contribute to porosity loss by cementation. From mineral quantification analysis (Fig. 11B), pore-filling carbonate cements (2% of the image area), usually surrounding framework grains, probably had an important part in prohibiting mechanical compaction. However, the exact timing and amounts of these carbonate cements is ambiguous. The reservoir quality in the sandstones is moderate.

6.2.3. The large scale cross-stratified sandstone unit

Cross-stratified sandstone deposits are well to moderately sorted with minor occurrence of patchy carbonate cement and a generally low proportion of authigenic minerals (e.g. clay coatings). Locally abundant replacive kaolinite has been observed filling both the primary and secondary pore space, associated with the alteration of igneous rock fragments and feldspars. The kaolinite is often well preserved and not covered by grain coating clays. Authigenic K-feldspar overgrowths, showing euhedral crystals were observed growing into open pore space. Overall, the primary pores are abundant and well interconnected in the cross-stratified sandstone samples. This suggests these deposits exhibit very good reservoir quality.

7. Conclusions

- Depositional facies had an important influence on the diagenetic development. The conglomeratic-dominated alluvial fan deposits are predominantly texturally and mineralogically immature and poorly sorted. The samples from these intervals generally have a higher abundance of authigenic clay minerals and cements, both early and late diagenetic. The authigenic clays are generally dominant in the sandy conglomerate and sandstone units. The reservoir quality of the conglomeratic unit intervals is low to very low. Inter- and intragranular pores are often minor in most of the samples. However, the sandy conglomerates, and especially the interbedded alluvial fan sandstone units, have shown greater reservoir quality in terms of porosity and permeability due to their better sorting.
- The large scale cross-stratified deposits were originally more mature petrographically than the other lithologies, their mineralogy dominated by quartz and minor amounts of feldspar and rock fragments. A suggested change in sediment provenance for large scale cross-stratified sandstones is proposed based on the presence of metamorphic rock fragments. Patchy carbonate cement and kaolinite are the main cement phases. The reservoir quality is generally very good in areas with minimal cementation. The primary porosity is common and well interconnected. Locally the pore space can be occluded by an abundance of kaolinite.
- The initial sediment composition and deposition in an arid to semi-arid climate exerted the major control on early diagenesis within the Edvard Grieg deposits. Furthermore, the dry to semi-dry climatic conditions during early diagenesis enhanced the infiltration of clays and precipitation of Fe-oxides.
- Early diagenetic processes include the growth of microcrystalline and poikilotopic non-ferroan carbonate cement, and minor amounts of authigenic K-feldspar, micro-quartz, and vermicular kaolinite. The latter is associated with slightly acidic porewater and dissolution of mica grains.
- Two main types of chlorite occur in the Edvard Grieg reservoirs. First generation Mg-rich pore-lining chlorite is linked to early mechanically infiltrated smectite coatings. The second generation is Fe-rich pore-filling chlorite developed during a later stage of burial.
- Late diagenesis saw the dissolution of feldspars grains and crystals within rock fragments, and precipitation of quartz and K-feldspar overgrowth from grain-contact dissolution. Furthermore, recrystallization of illite and chlorite, most likely from early grain-coating dioctahedral and trioctahedral smectite, and albitisation of plagioclase also occurred.
- Quantification of the main diagenetic phases and reconstruction of the initial texture and mineralogy (post mechanical compaction) based on the mineral maps helped provide a better understanding of

the visible primary and secondary porosity changes through the diagenetic evolution.

Acknowledgments

The authors would like to thank Lundin Norway AS for sponsoring this project, providing the core material, and for stimulating discussions of the results. Thanks to Maarten Aerts, Berit Løken Berg and Salahalldin Akhavan at the University of Oslo, and Lars Kirksæther at Petro-Sec, for helping out with sample preparation and analyses. Thanks to Lars Riber for reviewing the manuscript and Adrian Read for correcting the English. The authors wish to thank (Jose Arribas, Laura I. Net) and an anonymous MPG reviewer for valuable comments and suggestions.

References

Acker, J.G., Bricker, O.P., 1992. The influence of pH on biotite dissolution and alteration kinetics at low temperature. Geochem. Cosmochim. Acta 56 (8), 3073–3092.
Ajdukiewicz, J.M., Larese, R.E., 2012. How clay grain coats inhibit quartz cement and preserve porosity in deeply buried sandstones: observations and experiments. AAPG (Am. Assoc. Pet. Geol.) Bull. 96, 2091–2119.
Ajdukiewicz, J.M., Nicholson, P.H., Esch, W.L., 2010. Prediction of deep reservoir quality using early diagenetic process models in the Jurassic Norphlet Formation, Gulf of Mexico. AAPG (Am. Assoc. Pet. Geol.) Bull. 94, 1189–1227.
Beard, D.C., Weyl, P.K., 1973. Influence of texture on porosity and permeability of unconsolidated sand. In Diagenesis of Sandstones. AAPG (Am. Assoc. Pet. Geol.) Bull. 57 (2), 349–369.
Beaufort, D., Baronnet, A., Lanson, B., Meunier, A., 1997. Corrensite: a single phase or a mixed-layer phyllosilicate in the saponite-to-chlorite conversion series? A case study of Sancerre-Couy deep drill hole (France). Am. Mineral. 82 (1–2), 109–124.
Bjørlykke, K., 1984. Formation of secondary porosity: how important is it. In: Clastic diagenesis. AAPG Memoir, 37, pp. 277–286.
Bjørlykke, K., 1998. Clay mineral diagenesis in sedimentary basins—a key to the prediction of rock properties. Examples from the North Sea Basin. Clay Miner. 33 (1), 15–34.
Bjørlykke, K., 2014. Relationships between depositional environments, burial history and rock properties. Some principal aspects of diagenetic process in sedimentary basins. Sediment. Geol. 301, 1–14.
Bjørlykke, K., Aagaard, P., Dypvik, H., Hastings, D.S., Harper, A.S., 1986. Diagenesis and reservoir properties of Jurassic sandstones from the Haltenbanken area, offshore mid-Norway. In: Spencer, A.M. (Ed.), Habitat of Hydrocarbons on the Norwegian Continental Shelf. Graham & Trotman, London, pp. 275–286.
Bjørlykke, K., Aagaard, P., Egeberg, P.K., Simmons, S.P., 1995. Geochemical constraints from formation water analyses from the North Sea and the Gulf Coast Basins on quartz, feldspar and illite precipitation in reservoir rocks. Geol. Soc. Lond. Special Publ. 86 (1), 33–50.
Blair, T.C., McPherson, J.G., 1994. Alluvial fans and their natural distinction from rivers based on morphology, hydraulic processes, sedimentary processes, and facies assemblages. J. Sediment. Res. A64, 450–489.
Blair, T.C., McPherson, J.G., 2009. Processes and forms of alluvial fans. In: Parsons, A.J., Abrahams, A.D. (Eds.), Geomorphology of Desert Environments. Springer, Netherlands, pp. 413–467.
Bull, W.B., 1972. Recognition of alluvial fan deposits in the stratigraphic record. In: In: Rigby, J.K., Hamblin, W.K. (Eds.), Recognition of Ancient Sedimentary Environments, vol. 16. SEPM Special Publication, pp. 63–83.
Burley, S.D., Kantorowicz, J.D., Waugh, B., 1985. Clastic diagenesis. In: Brenchley, P.J., Williams, B.P.J. (Eds.), Sedimentology: Recent Development and Applied Aspects, pp. 189–226 The Geological Society, London, Special Publications, 18(1).
Busch, B., Hilgers, C., Gronen, L., Adelmann, D., 2017. Cementation and structural diagenesis of fluvio-aeolian Rotliegend sandstones, northern England. J. Geol. Soc. 174, 855–868 jgs2016-122.
Chamley, H., 1989. Clay Sedimentology. Springer-Verlag, Berlin Heidelberg, pp. 623.
Colson, J., Cojan, I., 1996. Groundwater dolocretes in a lake-marginal environment: an alternative model for dolocrete formation in continental settings (Danian of the Provence Basin, France). Sedimentology 43 (1), 175–188.
Dickinson, W.R., 1970. Interpreting detrital modes of graywacke and arkose. J. Sediment. Res. 40 (2), 695–707.
Döbelin, N., Kleeberg, R., 2015. Profex: a graphical user interface for the Rietveld refinement program BGMN. J. Appl. Crystallogr. 48, 1573–1580.
Dypvik, H., 1983. Clay mineral transformations in Tertiary and Mesozoic sediments from North Sea. AAPG (Am. Assoc. Pet. Geol.) Bull. 67 (1), 160–165.
Ehrenberg, S.N., 1993. Preservation of anomalously high porosity in deeply buried sandstones by grain-coating chlorite: examples from the Norwegian continental shelf. AAPG (Am. Assoc. Pet. Geol.) Bull. 77 (7), 1260–1286.
Ehrenberg, S.N., 1995. Measuring sandstone compaction from modal analysis of thin sections: how to do it and what the results mean. J. Sediment. Res. 65A (2), 369–379.
Ehrenberg, S.N., Jakobsen, K.G., 2001. Plagioclase dissolution related to biodegradation of oil in Brent Group sandstones (Middle Jurassic) of Gullfaks Field, northern North Sea. Sedimentology 48 (4), 703–721.
Fairbridge, R.W., 1967. In: Larsen, G., Chilingar, G. V. (q.v.) (Eds.), Phases of Diagenesis and Authigenesis, pp. 19–89.
Gloppen, T.G., Steel, R.T., 1981. The deposits, internal structure and geometry in six alluvial fan-fan delta bodies (Devonian, Norway) - a study in the significance of bedding sequence in conglomerates. In: Ethridge, F., Flores, R.M. (Eds.), Recent and Ancient Nonmarine Depositional Environments: Models for Exploration: Soc. Econ. Paleontologists Mineralogists.
Goldsmith, P.J., Hudson, G., Van Veen, P., 2003. Triassic. In: The Millennium Atlas: Petroleum Geology of the Central and Northern North Sea. Geological Society, London, pp. 105–127.
Gowers, M.B., Sæbøe, A., 1985. On the structural evolution of the Central trough in the Norwegian and Danish sectors of the North Sea. Mar. Petrol. Geol. 2, 298–318.
Hancock, N.J., 1978. Possible causes of Rotliegend sandstone diagenesis in northern West Germany. J. Geol. Soc. 135 (1), 35–40.
Hancock, N.J., Taylor, A.M., 1978. Clay mineral diagenesis and oil migration in the Middle Jurassic Brent sand Formation. J. Geol. Soc. 135 (1), 69–72.
Harvey, A., 2011. Dryland Alluvial Fans. Arid Zone Geomorphology: Process, Form and Change in Drylands, third ed. pp. 333–371.
Hillier, S., 1994. Pore-lining chlorites in siliciclastic reservoir sandstones: electron microprobe, SEM and XRD data, and implications for their origin. Clay Miner. 29 (4), 665–680.
Hillier, S., Fallick, A.E., Matter, A., 1996. Origin of pore-lining chlorite in the aeolian Rotliegend of northern Germany. Clay Miner. 31, 153–171.
Houseknecht, D.W., 1987. Assessing the relative importance of compaction processes and cementation to reduction of porosity in sandstones. AAPG (Am. Assoc. Pet. Geol.) Bull. 71 (6), 633–642.
Hower, J., Eslinger, E.V., Hower, M.E., Perry, E.A., 1976. Mechanism of burial metamorphism of argillaceous sediment: 1. Mineralogical and chemical evidence. Geol. Soc. Am. Bull. 87 (5), 725–737.
Humphreys, B., Smith, S.A., Strong, G.E., 1989. Authigenic chlorite in late Triassic sandstones from the Central Graben, North Sea. Clay Miner. 24 (2), 427–444.
Isaksen, G.H., Ledje, K.H.I., 2001. Source rock quality and hydrocarbon migration pathways within the greater Utsira High area, Viking Graben, Norwegian North Sea. AAPG (Am. Assoc. Pet. Geol.) Bull. 85, 0861–0884.
Jackson, C.A.L., Kane, K.E., Larsen, E., 2010. Structural evolution of minibasins on the Utsira High, northern North Sea; implications for Jurassic sediment dispersal and reservoir distribution. Petrol. Geosci. 16, 105–120.
Jahren, J.S., Aagaard, P., 1989. Compositional variations in diagenetic chlorites and illites, and relationships with formation-water chemistry. Clay Miner. 24 (2), 157–170.
Kessler, L.G., 1978. Diagenetic sequence in ancient sandstones deposited under desert climatic conditions. J. Geol. Soc. 135 (1), 41–49.
Ketzer, J.M., Morad, S., Amorosi, A., 2003. Predictive diagenetic Clay-mineral distribution in siliciclastic rocks within a sequence stratigraphic framework. In: Worden, R.H., Morad, S. (Eds.), Clay Mineral Cements in Sandstones. Blackwell Publishing Ltd., Oxford, UK, pp. 43–61.
Kim, B.C., Lowe, D.R., 2004. Depositional processes of the gravelly debris flow deposits, South Dolomite alluvial fan, Owens Valley, California. Geosci. J. 8 (2), 153.
Krinsley, D., 1998. Models of rock varnish formation constrained by high resolution transmission electron microscopy. Sedimentology 45, 711–725.
Lanson, B., Beaufort, D., Berger, G., Bauer, A., Cassagnabere, A., Meunier, A., 2002. Authigenic kaolin and illitic minerals during burial diagenesis of sandstones: a review. Clay Miner. 37 (1), 1–22.
Lattman, L.H., 1973. Calcium carbonate cementation of alluvial fans in southern Nevada. Geol. Soc. Am. Bull. 84 (9), 3013–3028.
Laursen, I., Fugelli, E., Lervik, K.S., 1995. Sequence stratigraphic framework of the Paleocene and Eocene successions, block 16/1, Norwegian North Sea. In: Sequence Stratigraphy on the Northwest European Margin: Proceedings of the Norwegian Petroleum Society Conference, 1–3 February 1993, vol. 5. Elsevier, Stavanger, Norway, pp. 471.
Liebske, C., 2015. iSpectra: an open source toolbox for the analysis of spectral images recorded on scanning electron microscopes. Microsc. Microanal. 21 (4), 1006–1016.
Machel, H.G., Mountjoy, E.W., 1986. Chemistry and environments of dolomitization - a reappraisal. Earth Sci. Rev. 23 (3), 175–222.
Mayayo, M.J., Bauluz, B., Lopez, J.M., 2000. Variations in the chemistry of smectites from the Calatayud Basin (NE Spain). Clay Miner. 35 (2), 365–374.
McKinley, J.M., Worden, R.H., Ruffell, A.H., 2003. Smectite in sandstones: a review of the controls on occurrence and behaviour during diagenesis. In: In: Worden, R.H., Morad, S. (Eds.), Clay Mineral Cements in Sandstones, vol. 34. International Association of Sedimentologists Special Publication, pp. 109–128.
Moore, D.M., Reynolds, R.C., 1997. X-ray Diffraction and the Identification and Analysis of Clay, second ed. Oxford University Press, pp. 400.
Morad, S., Márfil, R., Peña, J.A., 1989. Diagenetic K-feldspar pseudomorphs in the Triassic Buntsandstein sandstones of the Iberian range, Spain. Sedimentology 36 (4), 635–650.
Morad, S., Al-Aasm, I.S., Ramseyer, K., Marfil, R., Aldahan, A.A., 1990a. Diagenesis of carbonate cements in Permo-Triassic sandstones from the Iberian Range, Spain: evidence from chemical composition and stable isotopes. Sediment. Geol. 67 (3), 281–295.
Morad, S., Bergan, M., Knarud, R., Nystuen, J.P., 1990b. Albitization of detrital plagioclase in Triassic reservoir sandstones from the Snorre Field, Norwegian North Sea. J. Sediment. Res. 60 (3), 411–425.
Morad, S., Ketzer, J.R.M., De Ros, L.F., 2000. Spatial and temporal distribution of diagenetic alterations in siliciclastic rocks: implications for mass transfer in sedimentary basins. Sedimentology 47 (s1), 95–120.
Morad, S., Al-Ramadan, K., Ketzer, J.M., De Ros, L.F., 2010. The impact of diagenesis on the heterogeneity of sandstone reservoirs: a review of the role of depositional facies

and sequence stratigraphy. AAPG (Am. Assoc. Pet. Geol.) Bull. 94 (8), 1267–1309.
Moraes, M.A., De Ros, L.F., 1990. Infiltrated clays in fluvial Jurassic sandstones of Recôncavo Basin, northeastern Brazil. J. Sediment. Res. 60 (6), 809–819.
Mountney, N.P., 2006. Periodic accumulation and destruction of aeolian erg sequences in the Permian Cedar Mesa sandstone, White Canyon, southern Utah, USA. Sedimentology 153, 789–823.
Nadeau, P.H., Bjørkum, P.A., Walderhaug, O., 2005. Petroleum system analysis: impact of shale diagenesis on reservoir fluid pressure, hydrocarbon migration, and biodegradation risks. Geol. Soc. Lond. Petrol. Geol. Conf. series 6 (1), 1267–1274.
Nemec, W., Steel, R., 1984. Alluvial and coastal conglomeraets: their significant features and some comments on gravelly mass-flow deposits. Sedimentology of gravels and conglomerates. Memoir Canada Soc. Petrol. Geol. 10, 1–31.
Nickel, E., 1985. Carbonates in alluvial fan systems. An approach to physiography, sedimentology and diagenesis. Sediment. Geol. 42 (1), 83–104.
Nilsen, T.H., 1982. Alluvial Fan deposits. In: Sandstone Depositional Environments, vol. 31. AAPG Memoir 31, pp. 49.
NORLEX Project 2012: http://www.nhm2.uio.no/norlex/StandardLithostratigraphicWallchartOffshoreNorway.pdf.
Nøttvedt, A., Johannessen, E.P., Surlyk, F., 2008. The Mesozoic of Western Scandinavia and East Greenland. Episodes 31 (1), 59–65.
NPD, 2017. Factpages. Available at: http://factpages.npd.no/factpages Accessed: 06/06/2017.
Nystuen, J.P., Kjemperud, A.V., Müller, R., Adestål, V., Schomacker, E.R., 2014. Late Triassic to Early Jurassic climatic change, northern North Sea region. In: Martinius, A.W., Ravnås, R., Howell, J.A., Steel, R.J., Wonham, J.P. (Eds.), From Depositional Systems to Sedimentary Successions on the Norwegian Continental Margin. John Wiley & Sons, Ltd, Chichester, UK. http://dx.doi.org/10.1002/9781118920435.ch3.
Ormö, J., Komatsu, G., Chan, M.A., Beitler, B., Parry, W.T., 2004. Geological features indicative of processes related to the hematite formation in Meridiani Planum and Aram Chaos, Mars: a comparison with diagenetic hematite deposits in southern Utah, USA. Icarus 171 (2), 295–316.
Osborne, M., Haszeldine, R.S., Fallick, A.E., 1994. Variation in kaolinite morphology with growth temperature in isotopically mixed pore-fluids, Brent Group, UK North Sea. Clay Miner. 29 (4), 591–608.
Pettijohn, F.J., Potter, P.E., Siever, R., 1987. Sand and Sandstone. Springer Science and Business Media.
Pierson, T.C., Scott, K.M., 1985. Downstream dilution of a lahar: transition from debris flow to hyperconcentrated streamflow. Water Resour. Res. 21 (10), 1511–1524.
Pye, K., Krinsley, D.H., 1986. Diagenetic carbonate and evaporite minerals in Rotliegend aeolian sandstones of the southern North Sea: their nature and relationship to secondary porosity development. Clay Miner. 21 (4), 443–457.
Riber, L., Dypvik, H., Sørlie, R., 2015. Altered basement rocks on the Utsira high and its surroundings, Norwegian North Sea. Norw. J. Geol. 93, 57–89.
Rietveld, H., 1969. A profile refinement method for nuclear and magnetic structures. J. Appl. Crystallogr. 2 (2), 65–71.
Rittenhouse, G., 1971. Mechanical compaction of sands containing different percentages of ductile grains: a theoretical approach. AAPG (Am. Assoc. Pet. Geol.) Bull. 55 (1), 92–96.
Rodríguez-López, J.P., Liesa, C.L., Van Dam, J., Lafuente, P., Arlegui, L., Ezquerro, L., De Boer, P.L., 2012. Aeolian construction and alluvial dismantling of a fault-bounded intracontinental aeolian dune field (Teruel Basin, Spain); a continental perspective on Late Pliocene climate change and variability. Sedimentology 59 (5), 1536–1567.
Ross, G.J., 1969. Acid dissolution of chlorites: release of magnesium, iron and aluminum and mode of acid attack. Clay Clay Miner. 17 (6), 347–354.
Rossi, C., Kälin, O., Arribas, J., Tortosa, A., 2002. Diagenesis, provenance and reservoir quality of Triassic TAGI sandstones from Ourhoud field, Berkine (Ghadames) Basin, Algeria. Mar. Petrol. Geol. 19 (2), 117–142.
Ryan, P.C., Hillier, S., 2002. Berthierine/chamosite, corrensite, and discrete chlorite from evolved verdine and evaporite-associated facies in the Jurassic Sundance Formation, Wyoming. Am. Mineral. 87 (11–12), 1607–1615.
Saigal, G.C., Morad, S., Bjorlykke, K., Egeberg, P.K., Aagaard, P., 1988. Diagenetic albitization of detrital K-feldspar in Jurassic, Lower Cretaceous, and Tertiary clastic reservoir rocks from offshore Norway, I. Textures and origin. J. Sediment. Petrol. 58 (6), 1003–1013.
Salem, A.M., Morad, S., Mato, L.F., Al-Aasm, I.S., 2000. Diagenesis and reservoir-quality evolution of fluvial sandstones during progressive burial and uplift: evidence from the Upper Jurassic Boipeba Member, Reconcavo Basin, Northeastern Brazil. AAPG (Am. Assoc. Pet. Geol.) Bull. 84 (7), 1015–1040.
Schindelin, J., Arganda-Carreras, I., Frise, E., et al., 2012. Fiji: an open-source platform for biological-image analysis. Br. J. Pharmacol. 9 (7), 676–682.
Schmid, S., Worden, R.H., Fisher, Q.J., 2004. Diagenesis and reservoir quality of the Sherwood sandstone (Triassic), Corrib Field, Slyne Basin, west of Ireland. Mar. Petrol. Geol. 21, 299–315.
Steel, R., Ryseth, A., 1990. The Triassic—Early Jurassic succession in the northern North Sea: megasequence stratigraphy and intra-Triassic tectonics. Geol. Soc. Lond. Special Publ. 55 (1), 139–168.
Stricker, S., Jones, S.J., Sathar, S., Bowen, L., Oxtoby, N., 2016. Exceptional reservoir quality in HPHT reservoir settings: examples from the Skagerrak Formation of the Heron Cluster, North Sea, UK. Mar. Petrol. Geol. 77, 198–215.
Surdam, R.C., Jiao, Z.S., MacGowan, D.B., 1993. Redox reactions involving hydrocarbons and mineral oxidants: a mechanism for significant porosity enhancement in sandstones. AAPG (Am. Assoc. Pet. Geol.) Bull. 77 (9), 1509–1518.
Taylor, T.R., Giles, M.R., Hathon, L.A., Diggs, T.N., Braunsdorf, N.R., Birbiglia, G.V., Kittridge, M.K., Macaulay, C.I., Espejo, I.S., 2010. Sandstone diagenesis and reservoir quality prediction: models, myths, and reality. AAPG (Am. Assoc. Pet. Geol.) Bull. 94 (8), 1093–1132.
Walderhaug, O., 1994. Temperatures of quartz cementation in Jurassic sandstones from the Norwegian continental shelf–evidence from fluid inclusions. J. Sediment. Res. Sediment. Petrol. Process. 64A (2), 311–323.
Walker, T.R., 1967. Formation of red beds in modern and ancient deserts. Geol. Soc. Am. Bull. 78 (3), 353–368.
Walker, T.R., 1976. Diagenetic origin of continental red beds. In: Falke, H. (Ed.), The Continental Permian in Central, West and South Europe, pp. 240–282 Reidel Rordrecht, Holland, NATO Advanced Study Inst.
Weibel, R., 1999. Effects of burial on the clay assemblages in the Triassic Skagerrak Formation, Denmark. Clay Miner. 34 (4), 619–635.
Went, D.J., 2005. Pre-vegetation alluvial fan facies and processes: an example from the Cambro-Ordovician Rozel Conglomerate Formation, Jersey, Channel Islands. Sedimentology 52 (4), 693–713.
Wilkinson, M., Haszeldine, R.S., 2002. Fibrous illite in oilfield sandstones–a nucleation kinetic theory of growth. Terra. Nova 14 (1), 56–60.
Wilson, M.J., 1999. The origin and formation of clay minerals in soils: past, present and future perspectives. Clay Miner. 34 (1), 7–25.
Worden, R.H., Burley, S.D., 2003. Sandstone diagenesis: the evolution of sand to stone. In: Sandstone Diagenesis: Recent and Ancient, vol. 4. pp. 3–44.
Worden, R.H., Morad, S., 2003. Clay minerals in sandstones: controls on formation, distribution and evolution. In: Worden, R.H., Morad, S. (Eds.), Clay mineral Cements in Sandstones, pp. 1–41.
Wright, V.P., Tucker, M.E., 1991. Calcretes: an introduction. In: Calcretes. Blackwell Publishing Ltd., Oxford, UK. http://dx.doi.org/10.1002/9781444304497.ch.
Ziegler, P.A., 1990. Tectonic and paleogeographic development of the North Sea rift system. In: In: Blundell, D.J., Gibbs, A.D. (Eds.), Tectonic Evolution of the North Sea Rifts, vol. 181. International Lithosphere Programme, pp. 1–36.
Ziegler, P.A., 1992. North Sea rift system. Tectonophysics 208, 55–75. http://dx.doi.org/10.1016/0040-1951(92)90336-5.

Paper 2

3D characterization of porosity and authigenic cementation in Triassic conglomerates/arenites in the Edvard Grieg field using 3D micro-CT imaging

II

By

Markussen, Ø., Dypvik, H., Hammer, E., Long, H., and Hammer, Ø.

Marine and Petroleum Geology

Volume 99, January 2019, Pages 265-281

Marine and Petroleum Geology 99 (2019) 265–281

Contents lists available at ScienceDirect

Marine and Petroleum Geology

journal homepage: www.elsevier.com/locate/marpetgeo

Research paper

3D characterization of porosity and authigenic cementation in Triassic conglomerates/arenites in the Edvard Grieg field using 3D micro-CT imaging

Ørjan Markussen[a,*], Henning Dypvik[a], Erik Hammer[b], Haili Long[c], Øyvind Hammer[d]

[a] Department of Geosciences, University of Oslo, P.O. Box 1047, Blindern, NO–0316, Oslo, Norway
[b] Lundin Norway AS, Strandveien 4, NO–1366, Lysaker, Norway
[c] Department of Geoscience and Petroleum, Norwegian University of Science and Technology, Trondheim, Norway
[d] Geological Museum, University of Oslo, P.O. Box 1172, Blindern, 0318, Oslo, Norway

ARTICLE INFO

Keywords:
X-ray micro-CT
Digital rock model
Micro- and macropores
Pore-network modeling
Permeability
Carbonate cement
Conglomerates/arenites
Edvard Grieg field

ABSTRACT

X-ray computed tomography (CT) is well known especially in medical applications, but more recently also in geosciences. In this study we present a model for characterizing the distribution and texture of pores and pore-throats in siliciclastic rocks using multi-scale 3D micro-CT imaging and apply this to reservoir rocks of the Edvard Grieg field comprising conglomerates and arenites. The conglomerates are highly heterogeneous and rich in clays which are carrying the majority of the porosity/microporosity. The sandstones display better sorting, permeabilities and porosities, in particular the aeolian samples, compared to the conglomerate matrix. The sandstones also have less clay and carbonate cement. In order to resolve porosity distribution below image resolution, the dry/wet method was applied. This method not only resolves porosity distribution below image resolution, but also the pore throats and connectivities. In this study we also investigate the effect carbonate cementation has had on the porosity and pore-throat characteristics. Low reservoir quality conglomerates (very tight conglomerates) are highly carbonate cemented which has reduced the pore-throat connectivity significantly. In the sandstone samples the pore filling carbonate cement is less abundant and has had a much smaller effect on the porosity reduction and pore throat geometries and, hence permeabilities.

1. Introduction

The stratigraphic and structural development of the northern North Sea Basin has been extensively studied over decades of intensive petroleum exploration (e.g. Ziegler, 1975, 1990; 1992; Steel, 1993; Laursen et al., 1995; Nøttvedt et al., 1995; Slagstad et al., 2011). Since the oil exploration started on the Norwegian shelf, there have been many successful discoveries in the northern and central part of the Utsira High region; such as the Balder, Sleipner, Heimdal, Ringhorne, Grane and Jotun fields in addition to the recent Edvard Grieg (2007) and giant Johan Sverdrup (2010) discoveries. The Utsira High (Fig. 1a) is a large intrabasinal structural high (about 200 × 50 km) and has probably been a positive structural element since the Late Palaeozoic (Laursen et al., 1995). It is flanked by the Viking Graben to the west, the Ling Depression to the south and the Stord Basin to the east. The Edvard Grieg field is part of the southwestern Utsira High (Haugaland High), situated on the eastern margin of the southern Viking Graben. The studied wells (Fig. 1b) are located in a fault-bounded area (half-graben), mostly composed of siliciclastic deposits, most likely of the Triassic Skagerrak Formation of the Hegre Group (Steel and Ryseth, 1990; NPD, 2017) (Fig. 2).

The reservoir units in the Edvard Grieg field comprise highly heterogeneous conglomerate-dominated alluvial fan deposits, sand-dominated alluvial fan deposits, and aeolian dune sands (Mahmic et al., 2018) (Fig. 3). This heterogeneity causes challenges when calculating reserves and estimating oil and gas production due to a complex and inconsistent relationship between porosity and permeability distributions. The most common method used for gathering porosity and permeability information derives from detailed analyses of large amounts of core plugs. The heterogeneous lithologies, conglomerates and sandstones, often with more than one rock type per core plug, results in difficult interpretation of the plug porosities and permeabilities.

During the Triassic the initial sediment composition and deposition, occurring in an arid to semi-arid climate (Goldsmith et al., 2003; Nystuen et al., 2014) was a major control on early diagenesis within the Edvard Grieg deposits. Near-surface the detrital minerals reacted with

* Corresponding author.
E-mail address: orjan.markussen@geo.uio.no (Ø. Markussen).

https://doi.org/10.1016/j.marpetgeo.2018.10.015
Received 1 August 2018; Received in revised form 10 October 2018; Accepted 11 October 2018
Available online 15 October 2018
0264-8172/

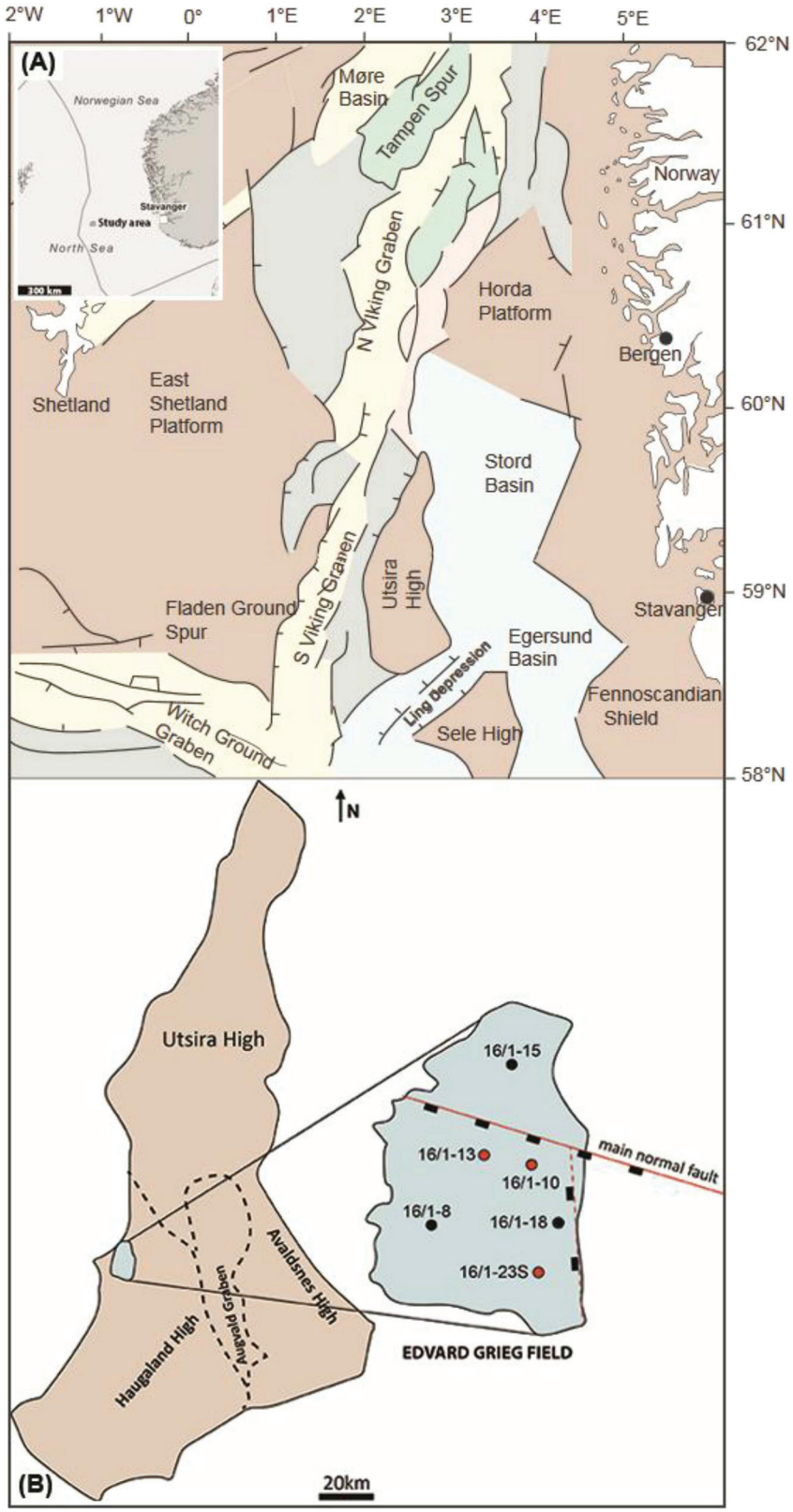

Fig. 1. (a) Regional map, showing the main fault trends, shear zones (grey lines) and different grabens and structural highs in the northern North Sea (Modified from Riber et al., 2015). (b) Map showing the wells used in this study (red circles), major normal fault (solid red line) and a minor normal fault (dashed red line).

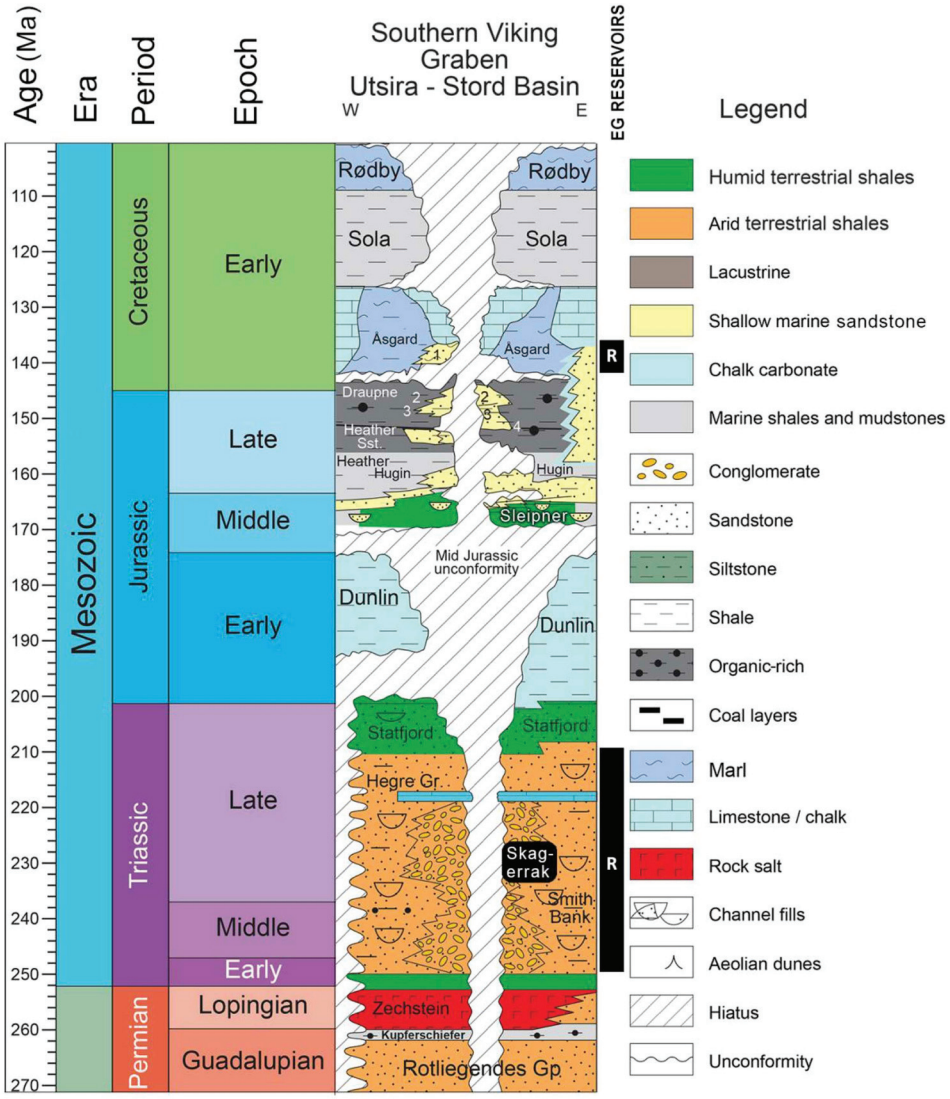

Fig. 2. Stratigraphic column of the Norwegian sector of the South Viking Graben, Utsira and Stord Basin (modified from NORLEX Project, 2012). The main Edvard Grieg reservoir (R) is indicated in the figure.

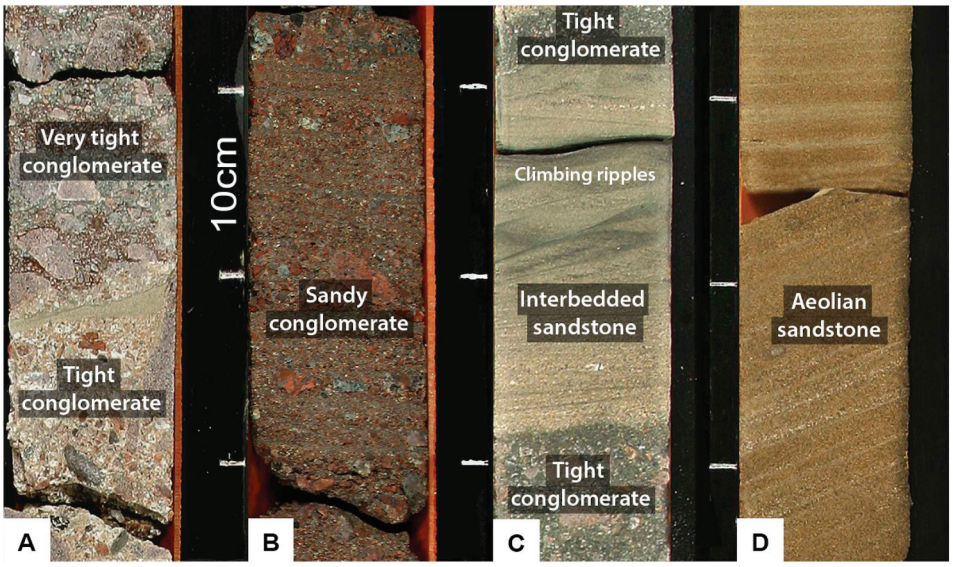

Fig. 3. (a) Very tight (usually associated with reddish and greenish colors) and tight conglomerate deposits. (b) Sandy conglomerate (c) Interbedded sandstone showing waning flow succession from matrix supported conglomerate into moderately sorted planar stratified sandstones with climbing ripples on top. The unit is overlaid by another matrix supported conglomerate. (d) Cross-bedded aeolian deposit composed of moderate to well sorted sandstone.

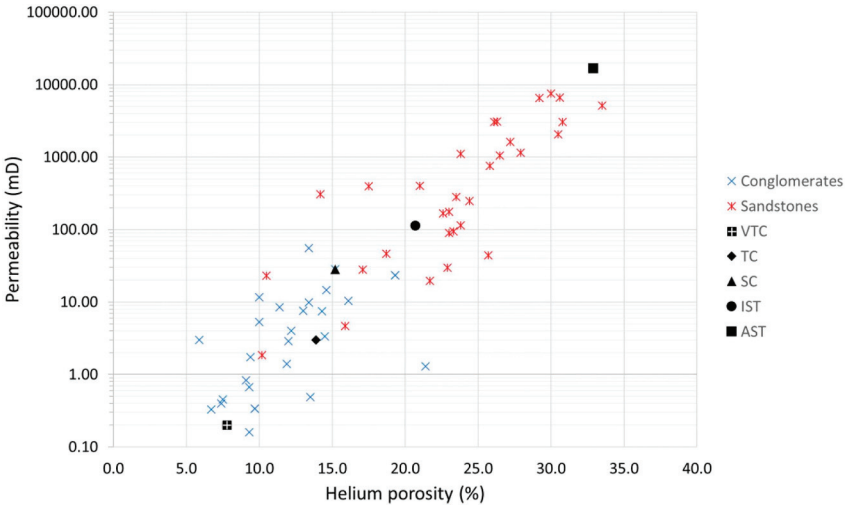

Fig. 4. Laboratory porosity and permeability data plot for conglomerates and sandstones in the Edvard Grieg field (red, blue x). The laboratory data for the five plug samples are also presented in the plot (**VTC** = Very tight conglomerate, **TC** = Tight conglomerate, **SC** = Sandy conglomerate, **IST** = Interbedded sandstone, **AST** = Aeolian sandstone). Conventional core analysis, helium porosity and nitrogen permeability, were measured by Weatherford Laboratories AS.

Table 1
Comparison of dry P_{CT} and wet/dry $P_{W/D}$ tomographic image porosity and laboratory measured porosity values (P_{He}) for the core plugs. $P_{petrology}$ = porosity derived from point counting and k = experimental permeability in millidarcy (mD). The resolution of the samples is represented as plug-scale/sub-plug μm. The percentage (%) of different mineral phases is derived from thin section analysis. **VTCx** = very tight conglomerate, **TCx** = tight conglomerate, **SCx** = sandy conglomerate, **IST** = interbedded sandstone, and **AST** = aeolian sandstone. **PS** = poorly sorted, **MS** = medium sorted, **MWS** = medium well sorted, and **VWS** = very well sorted.

Well	Core plugs					Extra conglomerate samples		
	16/1-10	16/1-13	16/1-23S	16/1-13	16/1-13	16/1-13	16/1-13	16/1-13
Sample name	**VTC (1′)**	**TC (1′)**	**SC (1.5′)**	**IST (1′)**	**AST (1′)**	**VTCx**	**TCx**	**SCx**
Depth (mDD)	1942.88	1999.00	2007.48	1997.80	1926.55	1976.55	1982.30	1967.95
Lithology	Very tight conglomerate	Tight conglomerate	Sandy conglomerate	Interbedded sst	Aeolian sst	Very tight conglomerate	Tight conglomerate	Sandy conglomerate
PHe	7.8	13.9	15.2	20.7	32.9	13.5[a]	14.3[a]	19.3[a]
Petrology	1.0	1.5	13.9	15.0	26.0	1.5	5.2	9.4
PCT (macroporosity)	1.1	2.6	3.5	3.8	22.8	0.8	1.9	5.2
PCT-sub-plug (macroporosity)	1.5	6.9	5.2	5.8	21.7	5.1	9.5	15.5
PW/D (total porosity)	5.7	12.1	14.0	20.2	32.7	4.8	13.5	18.8
k (mD)	0.2	3.0	28.4	113.0	16809.0	0.5[a]	7.5[a]	23.4[a]
% Quartz	16.1	15.0	11.2	42.0	38.8	16.5	16.8	37.2
% Feldspar	12.0	10.5	15.2	22.0	12.7	7.5	10.0	9.3
% Lithics	24.5	59.5	42.9	9.0	15.0	47	46.5	19.1
% Authigenic clays	14.5	11.0	10.5	6.0	3.0	16.5	12.5	20.7
% Cements (non-clay)	8.0	1.5	< 0.1	1.5	3.0	7.0	2.5	5.0
Sorting (modal data)	PS	PS	MS	MWS	VWS	PS	PS	MS
Resolution [μm]	17.9/6.2	13/6.2	32/10.1	18.4/4.9	16.6/3.1	7.3/1.7	10.1/1.65	10.1/1.65

[a] The values marked with an asterisk are from sister plugs.

the circulating meteoric water and atmosphere. Early infiltration of detrital clays, dominantly smectite (Chamley, 1989; Moraes and De Ros, 1990), resulted in substantial grain coating development. Early diagenetic processes also included growth of various cements, such as carbonate cement and authigenic K-feldspar. During the late diagenesis, with higher temperatures and pressures, chemical compaction lead to further dissolution of minerals and precipitation of cements and authigenic clays (e.g. Illitization of smectite) (Bjørlykke, 2014).

The reservoir quality varies significantly between the different units in the Edvard Grieg field. The conglomerate matrix has the poorest reservoir quality, mainly caused by the high abundance of authigenic clays, various non-clay cements (i.e. carbonate cement), and poor sorting (Mahmic et al., 2018). The pores and throats in these rocks are mainly on the nanoscale, generally located in the various authigenic clay minerals. Some macroscale pores and throats are associated with these conglomerates, but the connectivity is generally poor. The sandstone-dominated alluvial fan intervals have better reservoir quality characteristics. These lithologies are generally associated with a greater degree of sorting leading to higher intergranular porosities. The aeolian sandstones have the best reservoir quality (permeability > 10,000mD) (Fig. 4) due to well sorted deposits and minor occurrences of cements and authigenic clay minerals. The pores and pore throats are generally

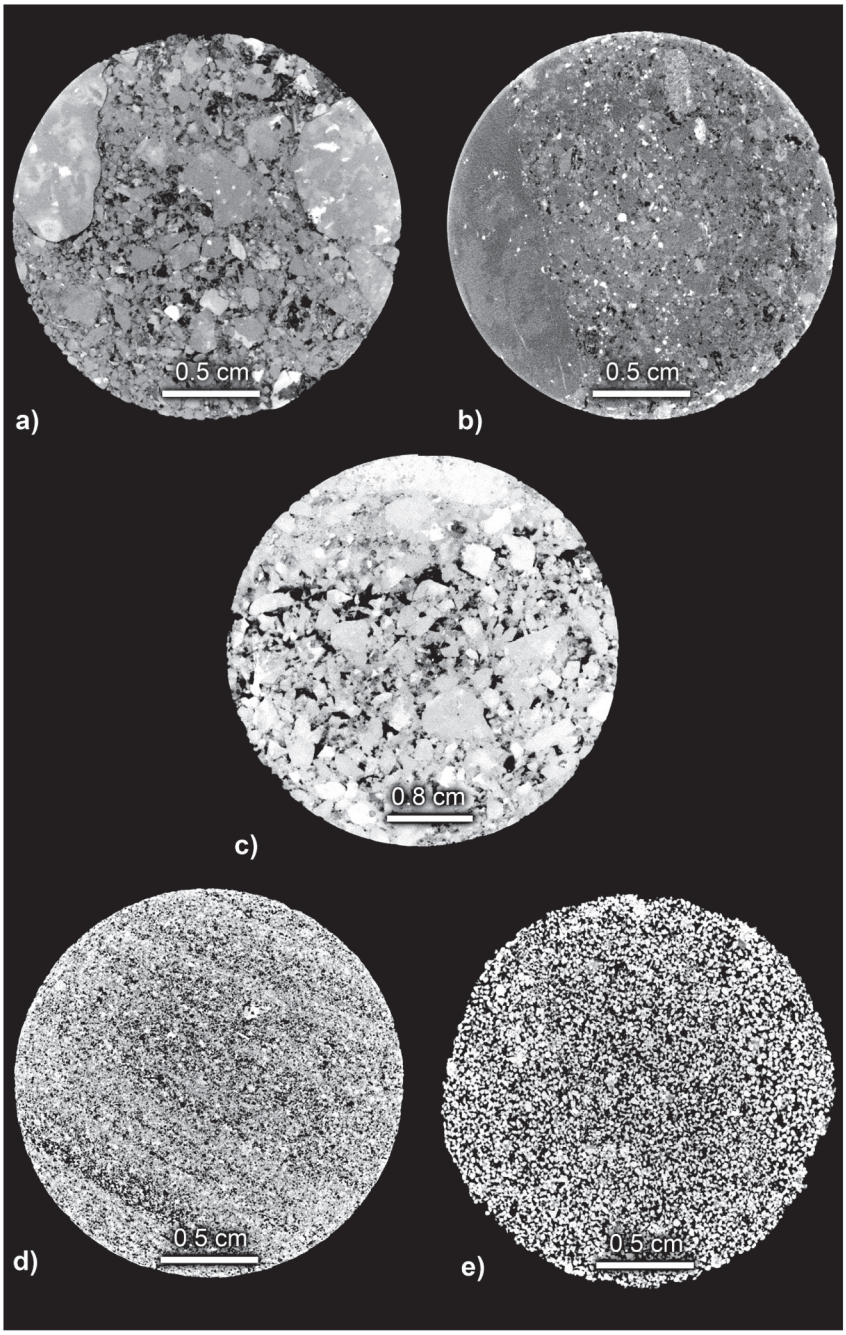

Fig. 5. Plug scale CT slices of the different lithologies. The measured x-ray density is given by a grayscale map which goes from black (pores) through to higher densities (lighter shades). (a) 16/1-13 tight conglomerate (TC) at 17.5 μm/voxel resolution. (b) 16/1-10 very tight conglomerate (VTC) at 17.9 μm/voxel resolution. (c) 16/1-23S sandy conglomerate (SC) at 32 μm/voxel resolution (1.5-inch sample). (d) 16/1-13 interbedded sandstone (IST) at 18.4 μm/voxel resolution. Note the bedding in the image, with areas that are either open (more black) or tight. (e) 16/1-13 aeolian sandstone (AST) at 16.6 μm/voxel resolution.

well connected.

Anovitz and Cole (2015) published a review of different methods for measuring porosity, including direct measurements such as Imbibition, Helium (He) porosimetry and Mercury Intrusion Capillary Pressure (MICP) measuring effective porosity only, as well as imaging methods and techniques such as Optical Petrology, Scanning Electron Microscopy (SEM) and Nuclear Magnetic Resonance (NMR). Resolving all the pore space, particularly sub-micron porosity has, however shown challenging. Hence, using a technique, which can provide three-dimensional (3D) porosity values and geometries (pore-throat) is important for both experimental and simulation studies. In recent years significant progress has been made in the development of high resolution 3-D tomographic imaging that enables of detailed porosity and pore-throat characterization in complex rocks (e.g. Riepe et al., 2011;

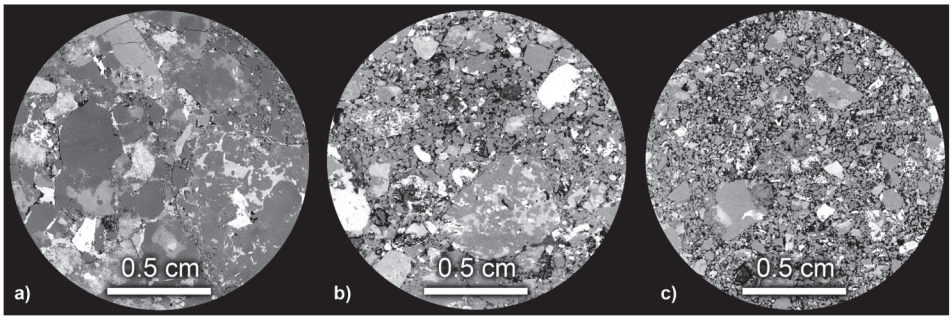

Fig. 6. Three extra conglomerate core samples. (a) 16/1-13 very tight conglomerate (VTCx) at 7.3 μm/voxel resolution. (b) 16/1-13 tight conglomerate (TCx) at 10.1 μm/voxel resolution. (c) 16/1-13 sandy conglomerate (SCx) at 10.1 μm/voxel resolution.

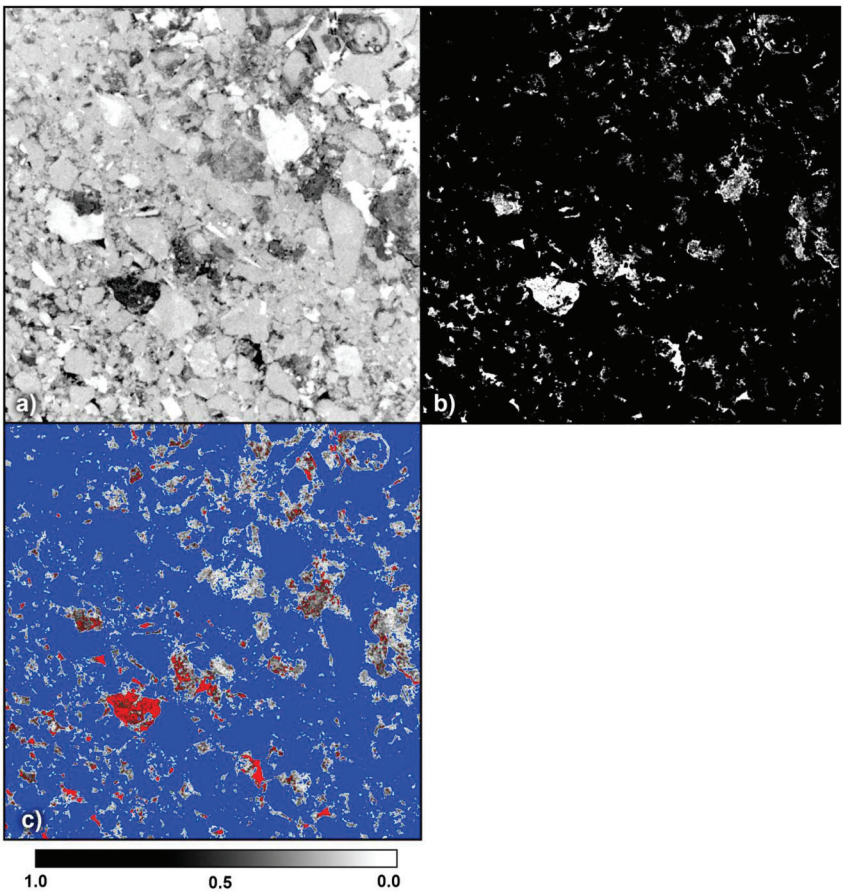

Fig. 7. Example of microporous regions comparison of dry and wet sample (16/1-13 tight conglomerate TC). (a) Dry image, the black is macropores. (b) Wet image, black is solid, white is macropores. (c) Difference map where blue is solid, red is macropores (pores larger than image resolution.), and microporous region is in different shades of grey. The majority of the porosity is in the grey area, where each voxel contains both fraction of solid and a fraction of pore.

Knackstedt et al., 2012; Bin et al., 2013; Bultreys et al., 2015) and carbonates (e.g. Lopez et al., 2012; Prodanovic et al., 2015; Pak et al., 2016; Fheed et al., 2018). Authigenic clays and carbonate cements have a strong influence on porosities and pore-throat geometries and hence reservoir quality by profoundly modifying the nano-to macroscale porosity and permeability characteristics (Worden and Morad, 2003; Salem et al., 2000; Taylor et al., 2010; Bjørlykke, 2014). X-ray based imaging, e.g. high resolution (micro-) computed tomography (CT) has gained substantial importance in the different fields of material and geology sciences (Cnudde et al., 2004; Kalender, 2006; Cnudde and Boone, 2013). Multi-scale 3D imaging, i.e. imaging at different scales and resolutions, allow one to directly investigate and characterize the distribution of pores and pore-throats as well as their characteristics (Attwood, 2006; Sakdinawat and Attwood, 2010). This factor is different from the conventional approach in porosity and permeability studies by applying mercury injection and gas absorption which only gives an overall pore-throat texture and its application is only limited to interconnected micropores (Bin et al., 2013). Improved understanding of pore geometry and development through time is necessary for an optimal recovery strategy.

In this paper, multi-resolution CT imaging, pore-network modeling, carbonate cement distribution, and spatial image registration techniques are demonstrated to capture and characterize heterogeneity to resolve special pore connectivity/distribution in the different

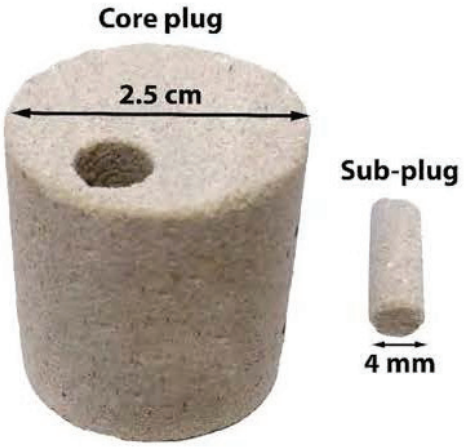

Fig. 8. Example of core plug and its sub-plug from interbedded sandstone. The core plug is scanned at 18.4 μm/voxel resolution, while the sub-plug is scanned at 4.9 μm/voxel resolution.

sedimentological units of the Edvard Grieg field. Spatial registration is the aligning or overlaying two or more data sets into the same coordinate system. In registration, typically one of the data sets is taken as the reference, and the other one is rotated, moved and/or possibly re-scaled, until both data sets match (Avizo, 2017). Differences in X-ray attenuation, i.e. changes in density caused by porosity and/or various minerals in the rock, are insufficient alone to distinguish mineralogy and regions that contain pore and matrix features. Therefore traditional petrographic techniques, such as optical microscopy, high resolution scanning electron microscopy (SEM) imaging and automated mineralogy mapping by 2D SEM-EDS, are necessary to use as complimentary methods. However, even if SEM can determine 2D micro-pores geometry and pore size at different scales (Lame et al., 2004), it is incapable to determine 3D pore-throat distribution and interconnectivity (Bin et al., 2013). Therefore, the integration of the different techniques with micro-CT analyses offers a better understanding for characterizing complex reservoirs rocks.

2. Material and methods

2.1. Samples studied

A total of five reservoir core plug samples (Table 1) were chosen based on lithology from wells 16/1-10, 16/1-13 and 16/1-23S from the Edvard Grieg field (Fig. 1b). Three of the samples are conglomerates, one is interbedded sandstone, and one is from aeolian sandstone. Furthermore, the conglomerate samples are divided into very tight conglomerate (VTC), tight conglomerate (TC) and sandy conglomerate (SC) (Figs. 3 and 5). The main criteria for sample selection, apart from lithology, were to cover the wide range of observed porosities and permeabilities (Fig. 4). Because of the high heterogeneity between the conglomerates, three extra core samples from the conglomerates (marked with an x in the sample name in Table 1) have been investigated to better understand textures, porosity and permeability in these complex lithologies (Fig. 6).

The helium porosity P_{He} and experimental permeability k for each sample are given in Fig. 4 and Table 1. Comprehensive petrological analysis based on thin-section petrography, scanning electron microscope (SEM-EDS), X-ray diffraction and diagenesis study of these different lithology units has been done by Mahmic et al. (2018). The optical microscope porosity $P_{petrology}$ and mineral content are also presented in Table 1.

2.2. Plug scale micro-CT imaging

The five standard core plug samples, 2.5–3.8 cm in diameter, were selected for micro-CT imaging and modeling at resolutions between 13 and 32 μm/voxel. A voxel is the three-dimensional (3D) equivalent of a pixel with added third coordinate (z) to x-y. Each of the coordinates is defined in terms of its position, color, and density. After imaging in dry state, the plugs were saturated under vacuum with X-ray attenuation brine (1M NaI–H_2O solution) following the method of Bhattad et al. (2014). This "wet" plug was imaged again by micro-CT and the tomograms were registered to the "dry" tomograms using the 3D-to-3D registration technique in the FEI Avizo/Pergeos software (Avizo, 2017). The brighter regions in the "wet" tomograms contain the NaI-bearing

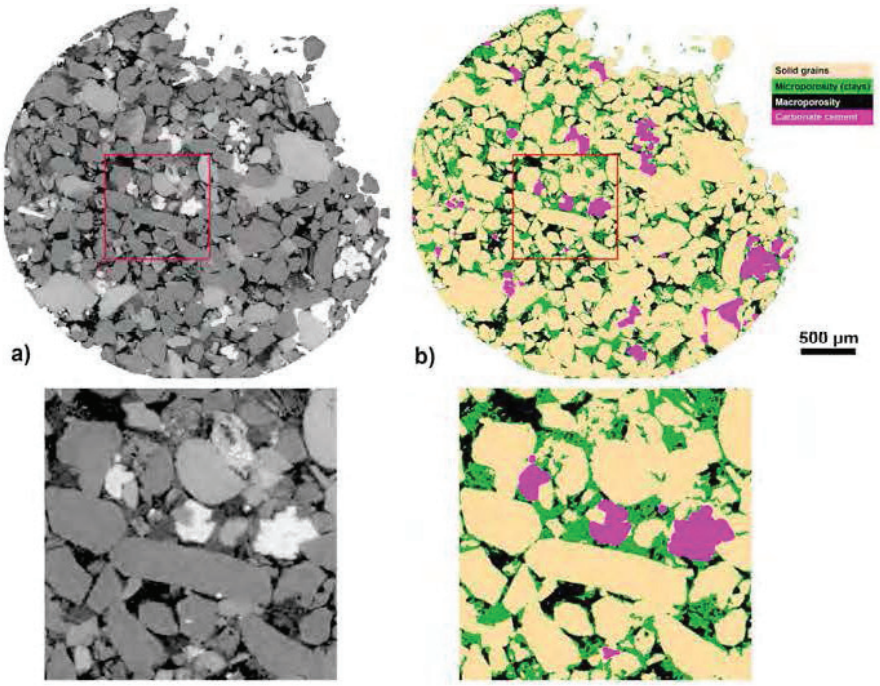

Fig. 9. (a) Slice from 3D tomogram. Black is macropores. (b) The segmented or phase separated pore/mineral phases. The lower two images are zoomed in areas.

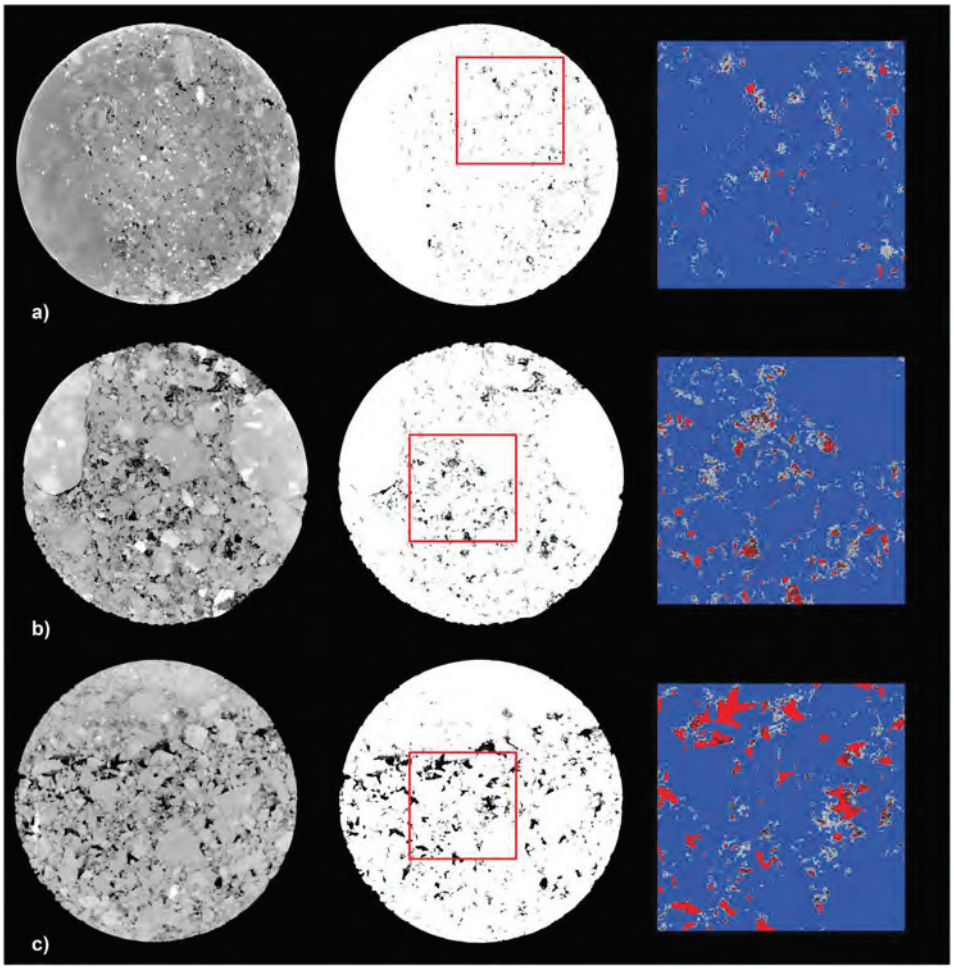

Fig. 10. "Dry" tomographic images (left side) of the conglomerates. Porosity map (middle images) from wet/dry difference with macropores (black), solid grain (white) and micropores (shades of grey). (a) 16/1-10 very tight conglomerate (VTC). (b) 16/1-13 tight conglomerate (TC). (c) 16/1-23S sandy conglomerate (SC). Right side images are zoomed sections of the difference map where blue is solid, red is macropores (pores larger than image resolution.), and microporous region is in different shades of grey.

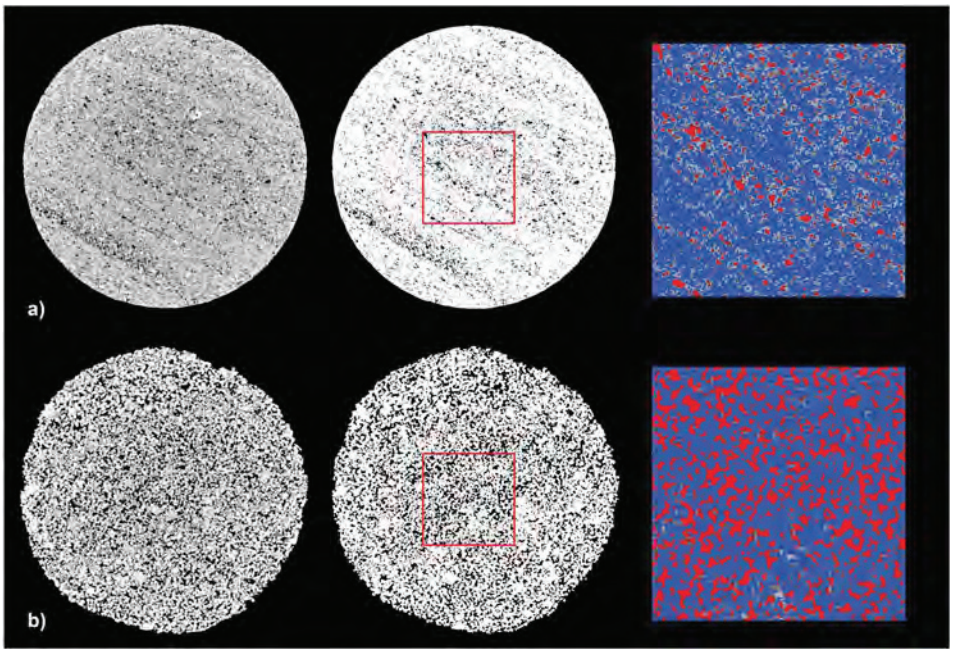

Fig. 11. "Dry" tomographic image (left side) of the sandstones. Porosity map (middle images) from wet/dry difference with macropores (black), solid grain (white) and micropores (shades of grey). (a) 16/1-13 interbedded sandstone (IST) at 18.4 μm/voxel resolution. Note the bedding in the image, with areas that are either open (more macroporosity) or tight (more solid). (b) 16-1-13 aeolian sandstone (AST) at 16.6 μm/voxel resolution. Right side images are zoomed sections of the difference map where blue is solid, red is macropores (pores larger than image resolution.), and microporous region is in different shades of grey.

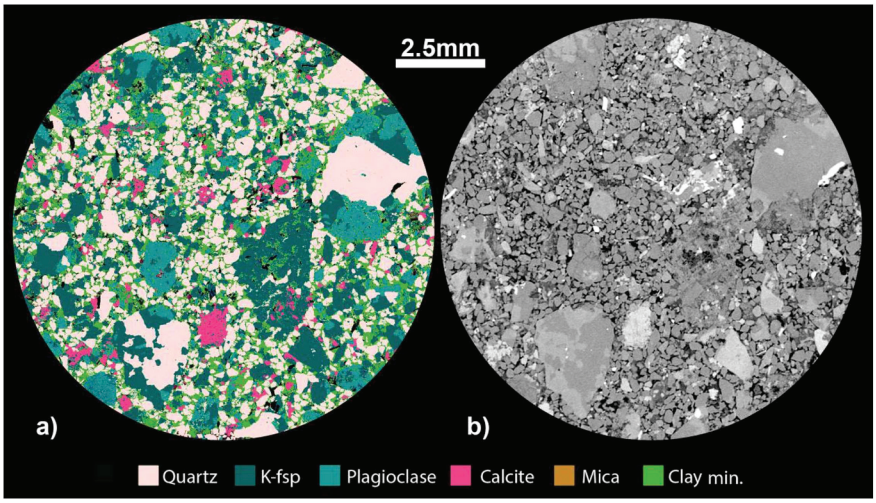

Fig. 12. Example of SEM-EDS in-situ mineral map and 3D tomogram of conglomerate sample (SCx). (a) In-situ mineralogy analysis, where black areas are macroporosity. The clay minerals in green have been grouped together, and are generally composed of various amounts of chlorite, illite, mixed–layer I/S, mixed–layer C/S and kaolinite. (b) Registered 3D tomogram image in "dry" state. Black areas are macroporosity.

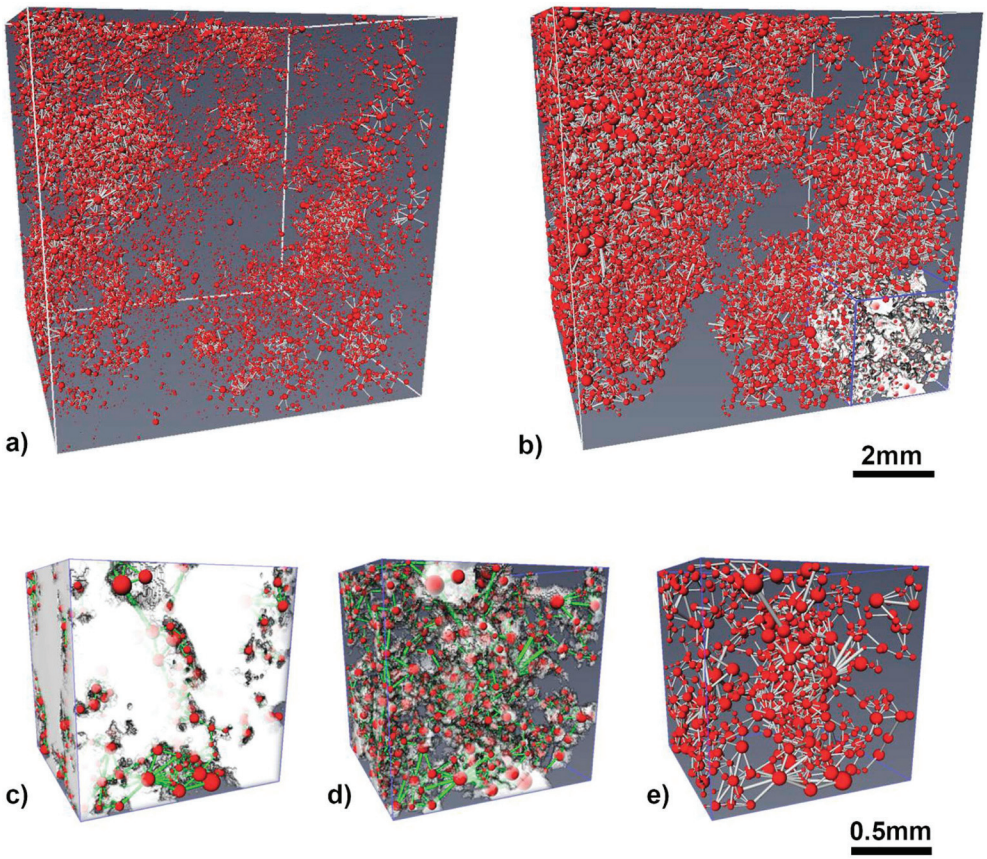

Fig. 13. 3D visualization of pore network model of 500 μm^3 subset cube. (a) Macroporosity and pore throat model of tight conglomerate sample TC (note the disconnected macropores in red). (b) Added micropores which gives the total porosity and connectivity. (c)(d) zoomed in on a 150 μm^3 cube subset showing solid regions (white) with macro- and microporosity (e) and only pore-throats network.

fluid and represent regions with significant microporosity (Fig. 7).

These plug scale CT scans were used to get a better overview over macro- and micro-porosity, lithological variations, carbonate cement distribution, and laminations. The microporosity in this study is defined as pores which are below resolution of the plug-scale micro-CT scan. The approach was aimed at selecting the location for thin section analyses and higher resolution pore scale sub-plugs.

High resolution backscattered scanning electron microscope (BSEM) images were carried out on polished faces at 750 nm/pixel resolution and registered into the best-fit 3D tomogram following the method of Latham et al. (2008). These polished faces were also scanned using an automated mineral and petrographic analysis (SEM-EDS), quantifying the *in-situ* mineralogy based on their chemical composition. This approach provides high resolution analysis of the sample, down to nano-scale, and should lead to drastic improvement in the identification of pore-filling clay and micro-pores.

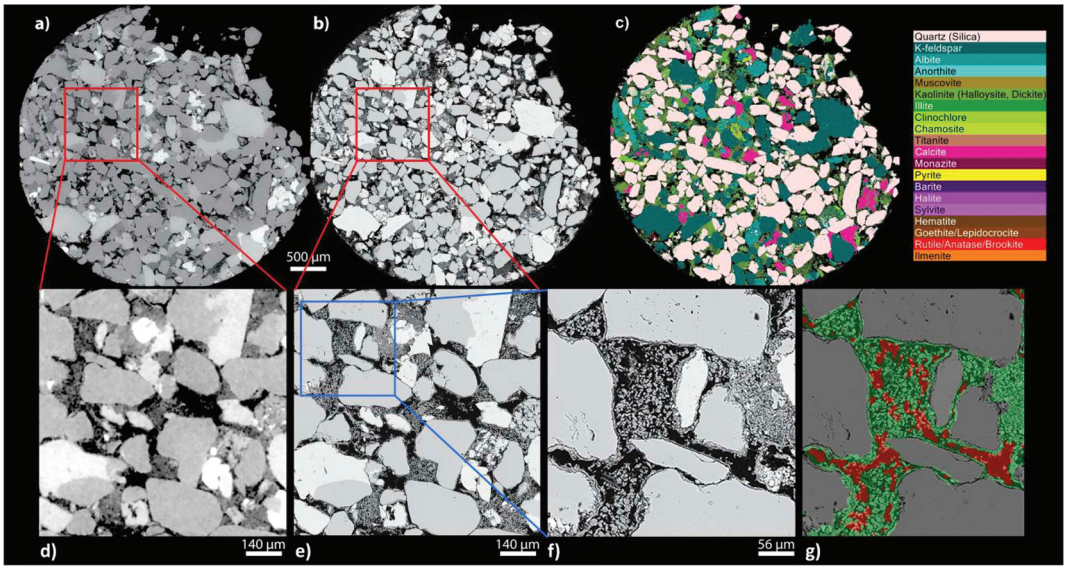

Fig. 14. Registered sub-plug tomogram and SEM of sandy conglomerate SCx. (a) Registered 2D tomogram of SCx sub-plug at 1.65 µm/voxel resolution. (b) Registered 2D high resolution SEM at 250 nm/pixel resolution. The two lower images show magnified sections of microstructures of the 2D SEM image. (c) In-situ SEM-EDS automated mineralogy analysis. (d) Magnified section of tomogram (black = macroporosity). (e) Magnified section of 2D SEM image (f) an inset of (e) showing microporosity. (g) Combined high-resolution 2D SEM images and segmented 3D tomogram image where macroporosity is in red and microporosity in green color. This enables to quality control of the segmentation.

2.3. Sub-plug micro-CT imaging

In order to obtain images of microporosity sub-plugs of 4–10 mm diameter were drilled from the corresponding core samples and scanned from 1.65 to 6.2 µm/voxel (Fig. 8) to probe the porosity microstructures < 6 µm in these highly heterogeneous samples.

To investigate the detailed pore structures, the 2D SEM images at 250 nm/pixel resolution were registered into the comparable tomogram, which involves searching the entire 3D dataset for the exact slice and orientation of the tomogram that matches the 2D SEM image (Arns et al., 2005; Knackstedt et al., 2012; Avizo, 2017). The 2D SEM-EDS mineralogy maps are into the 3D data volume for direct identification of minerals with corresponding X-ray attenuation.

2.4. Image processing and segmentation

The image segmentation, transforming a grayscale image into a binary image, is a crucial step in the image analysis to produce correct 3D model of the sample. The goal is to separate different compositional phases based on greyscale values in the images (Knackstedt et al., 2012). The individual 8-bit grey scale images where de-noised to remove most of the image noise and we applied edge sharpening (non-local means filter) on the tomographic images (Avizo, 2017).

The tomographic images were then digitally segmented in FEI Avizo v.8 and Pergeos v.1 software into four main phases, i.e. macroporosity P_{CT}, microporosity, carbonate cement and solid grains, based on the X-ray attenuation values of each voxel (Fig. 9). The micropores are generally associated with clay fraction or diagenetic cement. In this study we apply the fast watershed algorithm to auto segment the 3D grey scale image. The watershed technique is based on a topological interpretation of the image. Any grayscale image can be viewed as a topographic surface where high intensity grey values denotes peaks and hills while low intensity grey values denotes valleys. You start filling every isolated valleys (local minima) with different colored water (labels). An approach is to imagine the landscape being immersed in a lake, with holes pierced in local minima. Basins (isolated vallyes) will fill up with water starting at these local minima, and, at points where water coming from different basins would meet, dams are built. When the water level has reached the highest peak in the landscape, the process is stopped. As a result, the landscape is partitioned into regions or basins separated by dams, called watershed lines or simply watersheds (Roerdink and Meijster, 2000: Avizo, 2017). Tomogram image porosity with pore size above image resolution P_{CT} is underestimated compared to the helium and petrographic porosity because of the unresolved microporous regions, such as in the clay phase, which contributes to the total porosity.

To resolve both the macro and microporosity in the 3D image a difference map of “wet-dry”, obtained by subtracting a “dry” from “wet” image (Figs. 10 and 11), was used to locate and quantify the microporosity of each voxel in 3D (Arns et al., 2005; Riepe et al., 2011; Knackstedt et al., 2012; Bin et al., 2013; Bhattad et al., 2014). All the voxels without X-ray contrasting fluid saturation (i.e. in solid grains) are shown in white, while macroporosity is in black and microporosity in shades of grey, i.e. regions with significant microporosity. In addition to quantification of the microporosity, the connectivity of these pores is also an important petrophysical property. Saturation with contrasting fluid is consequently crucial to visualize the pore connectivity in 3D. Further investigation and quality control of the porosity microstructures along with in-situ quantitative mineralogy was obtained by SEM-EDS (Fig. 12).

3. Results and discussion

3.1. Conglomerates

The conglomerate matrix samples exhibit a wide range of mineral phases, e.g. quartz carbonate cement, feldspar, clay minerals in

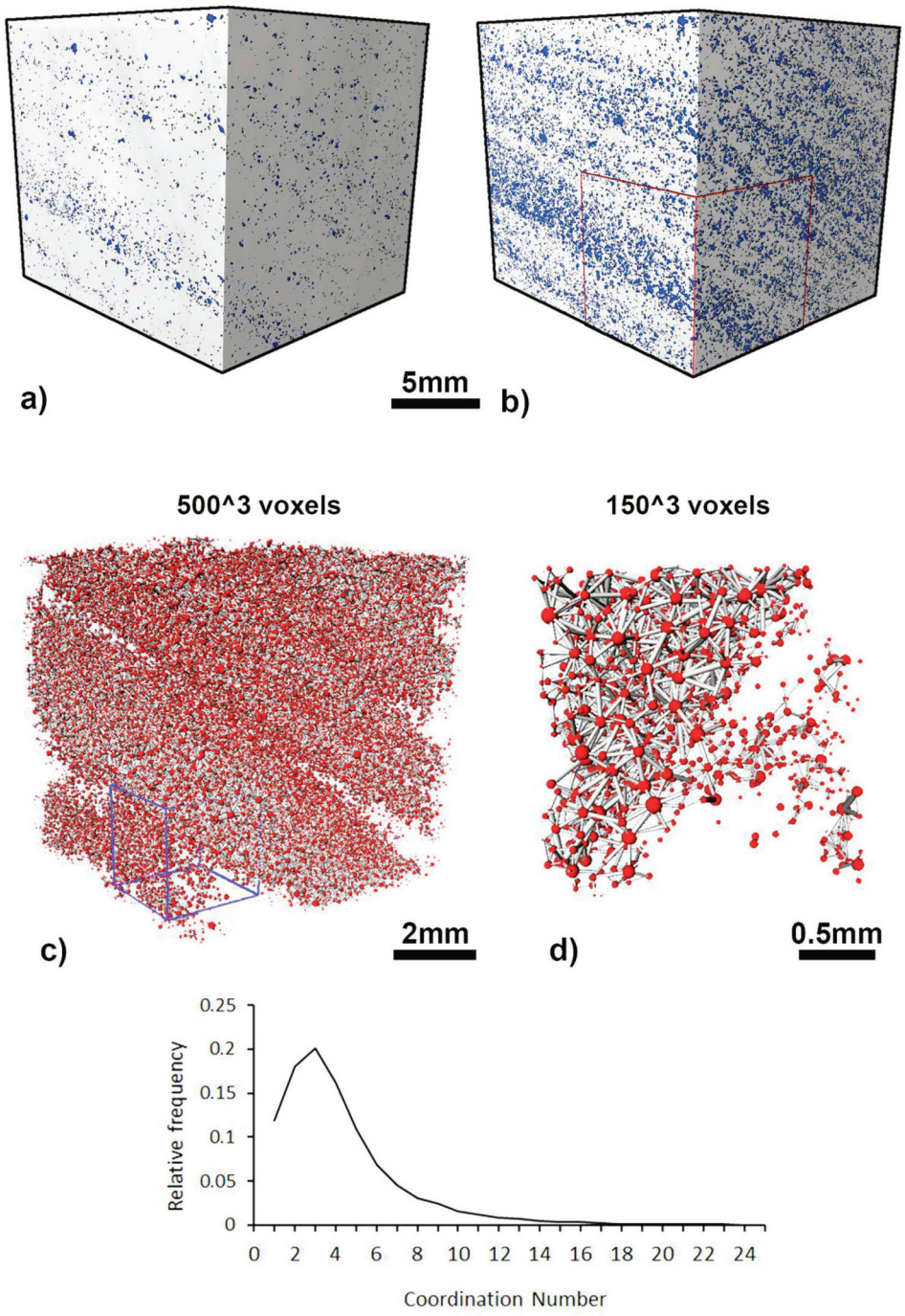

Fig. 15. Macro- and microporosity in the interbedded sandstone. (a) Macropores (blue) above 18.4 μm. (b) Microporosity distribution (blue). (c) 500 μm^3 zoomed cube subset, red square (b) showing the pore-throat distribution and interconnections. Note the very tight layers with less pores and pore-throats. However, they are still connected as shown in (d). The majority (16.4%) of the total 20.2% porosity is located below 18.4 μm resolution. Bottom plot is coordination number (number of contacts a pore has with its neighbors) plot represents the degree of connectivity within the pores (b).

addition to rock fragments. Petrological analysis based on thin-section petrography and SEM-EDS showed that the very tight and tight conglomerate matrix, with permeability 0.2mD and 3mD respectively, display a high degree of heterogeneity and low reservoir quality (Fig. 5a and b). The low reservoir quality is generally associated with the poorly sorted matrix (silt to very coarse) and large amounts of cements and authigenic clay minerals, which highly influence the total porosity and permeability. Based on XRD and SEM analysis the clay phase (cf. Fig. 12) is composed of various amounts of intergranular chlorite, illite, mixed–layer illite/smectite (I/S), mixed–layer chlorite/smectite (C/S) and kaolinite. The sandy conglomerates also display this high degree of heterogeneity, but the matrix is more sandy, hence more porous and

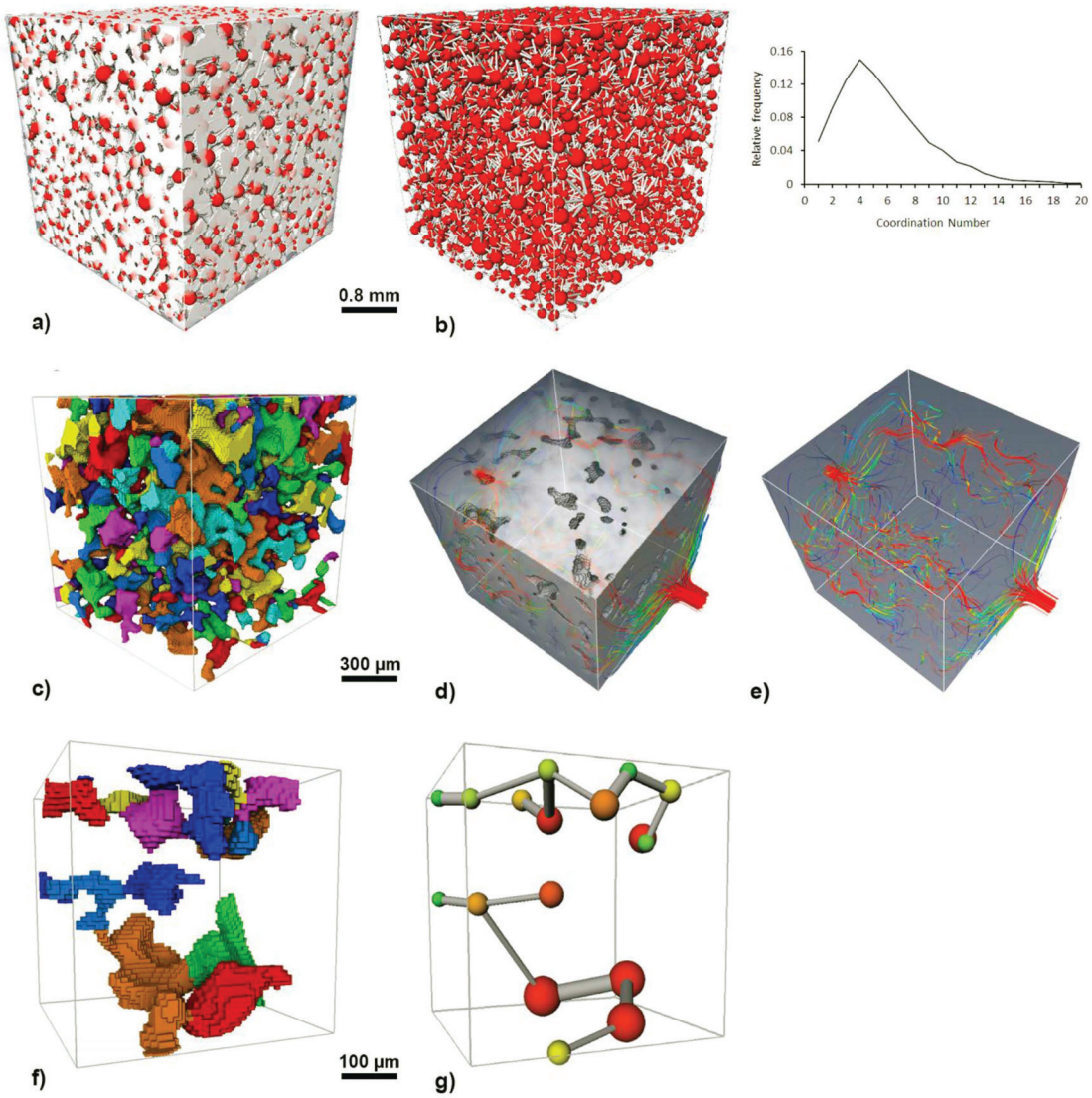

Fig. 16. 3D visualization of pore and throat network model of 500 µm^3 subset cube of aeolian sandstone. (a) Pore-throats with solid phase (white). (b) The pore-throats network model without solid phase. It show well interconnected pore-throats. A coordination number (number of contacts a pore has with its neighbors) plot to the right represents the degree of connectivity within the pores. (c) 150 µm^3 zoomed cube subset view of separated pores (d and e) Simulated continuous velocity flow through the pore space. Slower streams near the blue end of the spectrum, and faster stream near the red end of the spectrum. Detailed view of the separated pores (f) and pore network (g).

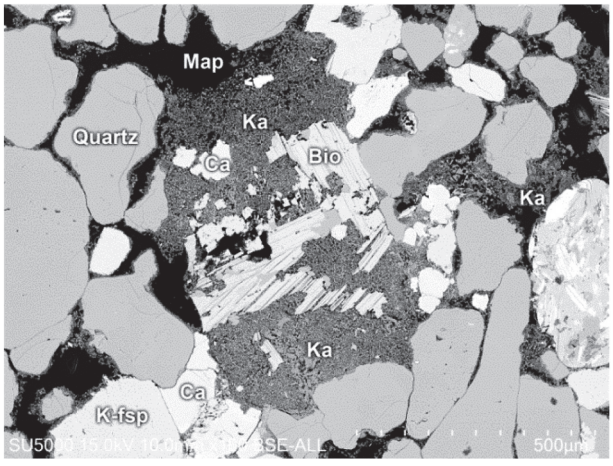

Fig. 17. High resolution 2D SEM image of aeolian sandstone showing locally abundant kaolinite. *Map* = macroporosity, *Ka* = kaolinite, *Ca* = carbonate cement, *Bio* = biotite and *K-fsp* = K-feldspar. Note the microporosity (black) in the regions with kaolinite. This microporosity is generally unresolvable in the micro-CT tomograms.

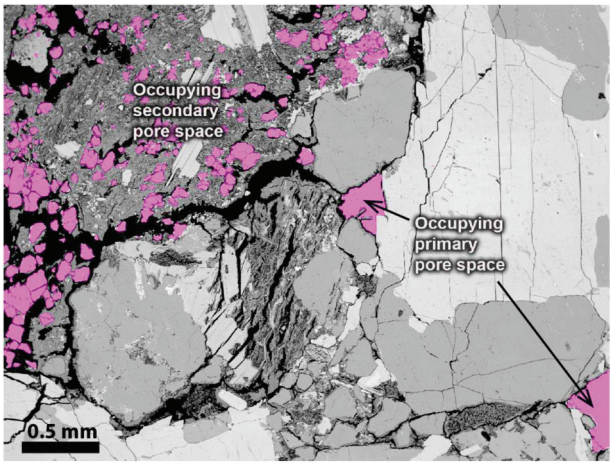

Fig. 18. 2D SEM image of carbonate cement (purple) occupying both the primary and secondary pore space in the tight conglomerate.

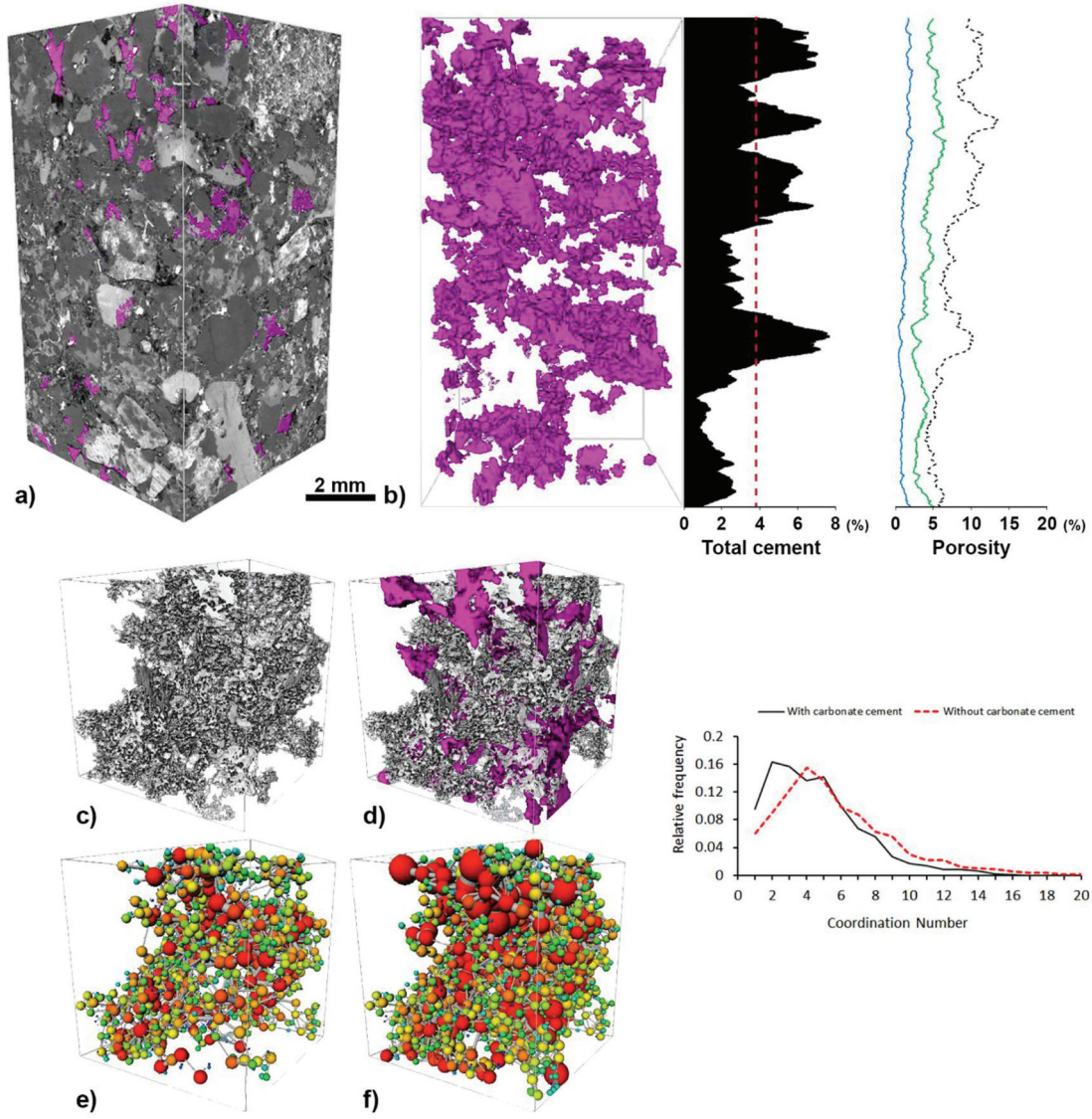

Fig. 19. 3D visualization of carbonate cement and total macroporosity in the very tight conglomerate (VTCx). (a) 3D visualization of carbonate cement (purple color) together with different mineral phases (shades of grey). (b) 3D visualization of carbonate cement and profile of total amount of cement along the sample (red dotted line is the average). The left side graphs show the porosity distribution in the samples. The blue (left) curve is macroporosity, middle curve (green) is total porosity (macro- and microporosity), and right dotted line is total porosity when carbonate cement is removed from the 3D model. (c) Zoomed 500^3 cube sub-set of total porosity. (d) Total porosity (white/grey) and carbonate cement (purple). (e) Pore-throat network model of total porosity with carbonate cement. (f) Pore-throat network model of total porosity when carbonate cement is removed from the 3D model. A coordination number (number of contacts a pore has with its neighbors) plot to the lower right represents the degree of connectivity within the pores. Note the higher connectivity when the carbonate cement is removed from the 3D model (red dashed line).

permeable (> 20mD) compared to the very tight and tight conglomerate matrix types which are silt dominated.

Based on tomogram observations the derived macroporosity P_{CT} is less than P_{He} and $P_{petrology}$ (Table 1). The thin-sections were impregnated with blue-stained epoxy making regions of microporosity visible, partly explaining the higher $P_{petrology}$ values. The thin-section, SEM-EDS, "dry/wet" scanning, and conventional experimental results of core analysis, i.e. helium porosity, does indicate that the majority of the total porosity, up to more than 70% in the tight and very tight conglomerate, is located in the clay rich phases. Hurst and Nadeau, 1995 estimated microporosity of diagenetic clay minerals from BSE micrographs of petrographic sections. They found microporosities in authigenic kaolinite averaging to 43%, grain-coating chlorite to 50% and illite approximately 90%. Detrital clays on the other hand had porosities in the range of 10%. These values compare to our study, having a mix of kaolinite, chlorite and illite, and suggest that the clays in the Edvard Grieg samples are authigenic. In the conglomerates the "dry/wet" microporosity in the clay rich parts contributes between 40 and 75% of the total porosity. In the more kaolinite rich aeolian sandstone the microporosity, associated with the clays, contributes 34% of the total porosity. The pore-throats and pore connectivity associated with these clays can have important control on the flow capacity, water saturation, and hydrocarbon flow rate in reservoir rocks. Therefore, the porosity alone is not alone an accurate indicator of reservoir quality (Rushing et al., 2008). The advantage of this "dry/wet" approach becomes even more evident in lithologies with abundance of pore-filling clay minerals, such as in the tight conglomerates.

The macro and micro pore networks give 3D topological and geometric characterization of the pore space. The majority of macropores (e.g. Figs. 13a and 15a) above the image resolution appear disconnected, often with associated secondary porosity. When combined together with microporosity regions (e.g. Figs. 13b and 15b), the

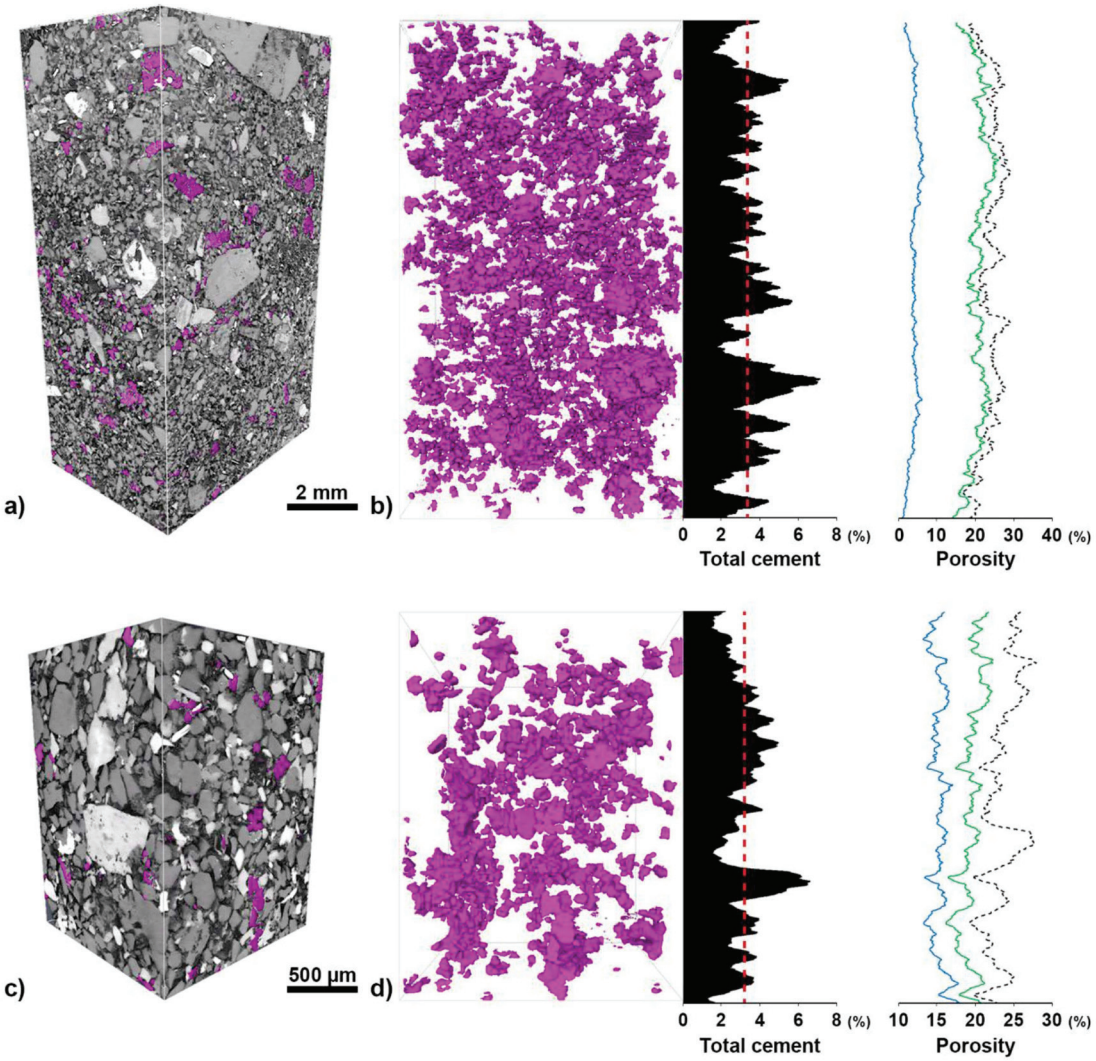

Fig. 20. Example of carbonate cement distribution in the sandy conglomerate sample (SCx) at 10.1 µm/voxel. (a) 3D visualization of carbonate cement (purple color) together with different mineral phases (shades of grey). (b) 3D visualization of carbonate cement and profile of total amount of cement along the sample (red dotted line is the average). (c) 3D visualization in sub-plug (1.65 µm/voxel) of carbonate cement (purple color) together with different mineral phases (shades of grey). (d) Carbonate cement distribution in the sub-plug and profile of total amount of cement along the sample (red dotted line is the average). Note the similarities in the amount and distribution of cement compared to (b). The left side graphs show the porosity distribution in the samples. The blue (left) curve is macroporosity, middle curve (green) is total porosity (macro- and microporosity), and right dotted line is total porosity when carbonate cement is removed from the 3D model.

connectivity increases drastically. The pore-filling clays may locally choke both primary and secondary pores as well as the pore-throats, resulting in overall lower permeabilities in these lithologies. This pattern was observed in all conglomerate samples. In Fig. 13 an example of 3D visualizing the distribution and connectivity of macro- and micropores (mainly in the clay phase) in the tight conglomerate matrix. For the conglomerates matrix, especially the very tight conglomerate matrix, further analyses were done on the registered 2D SEM images to better explain the porosity microstructures and to quality control the phase separation (segmentation) (Fig. 14). This enables a pixel-to-pixel comparison between the high-resolution SEM image and the corresponding tomogram slice from the micro-CT data. The data shows that majority of flow probably occurs through the microporous regions both due to the significant distribution of microporosity in the clays and their highly interconnected microporosities. Some variations are evident between the images possible due to damage (plucking) during sample preparation or polishing of sections for SEM analysis.

3.2. Sandstones

The two sandstone core plug samples, especially the aeolian sample, exhibit better sorting and a reduced amount of authigenic clays compared to the conglomerate matrix samples. The carbonate cement is patchy. Locally abundant replacive kaolinite has been observed in SEM, filling both the primary and secondary pore space, associated with the alteration of igneous rock fragments and feldspars. Kaolinite often occurs mostly as thin vermicular finely stacked booklet type crystals (5–10 µm), but may sometimes show blocky to thick, well-developed crystals. The highest helium porosities and permeabilities have been registered in the aeolian sandstone, 32.9% and 16809mD respectively (Table 1). The interbedded sandstone has higher percentage of authigenic clays, and related microporosity than the aeolian sandstone. In addition, the reduced sorting of the interbedded sandstone explain the lower porosity and permeability, 20.7% and 113mD respectively, compared to the aeolian sandstone.

The “dry/wet” procedure on the aeolian sandstone samples shows that microporosity only contributes around 30% of the total porosity. This reflects the better sorting, increased macroporosity and lower

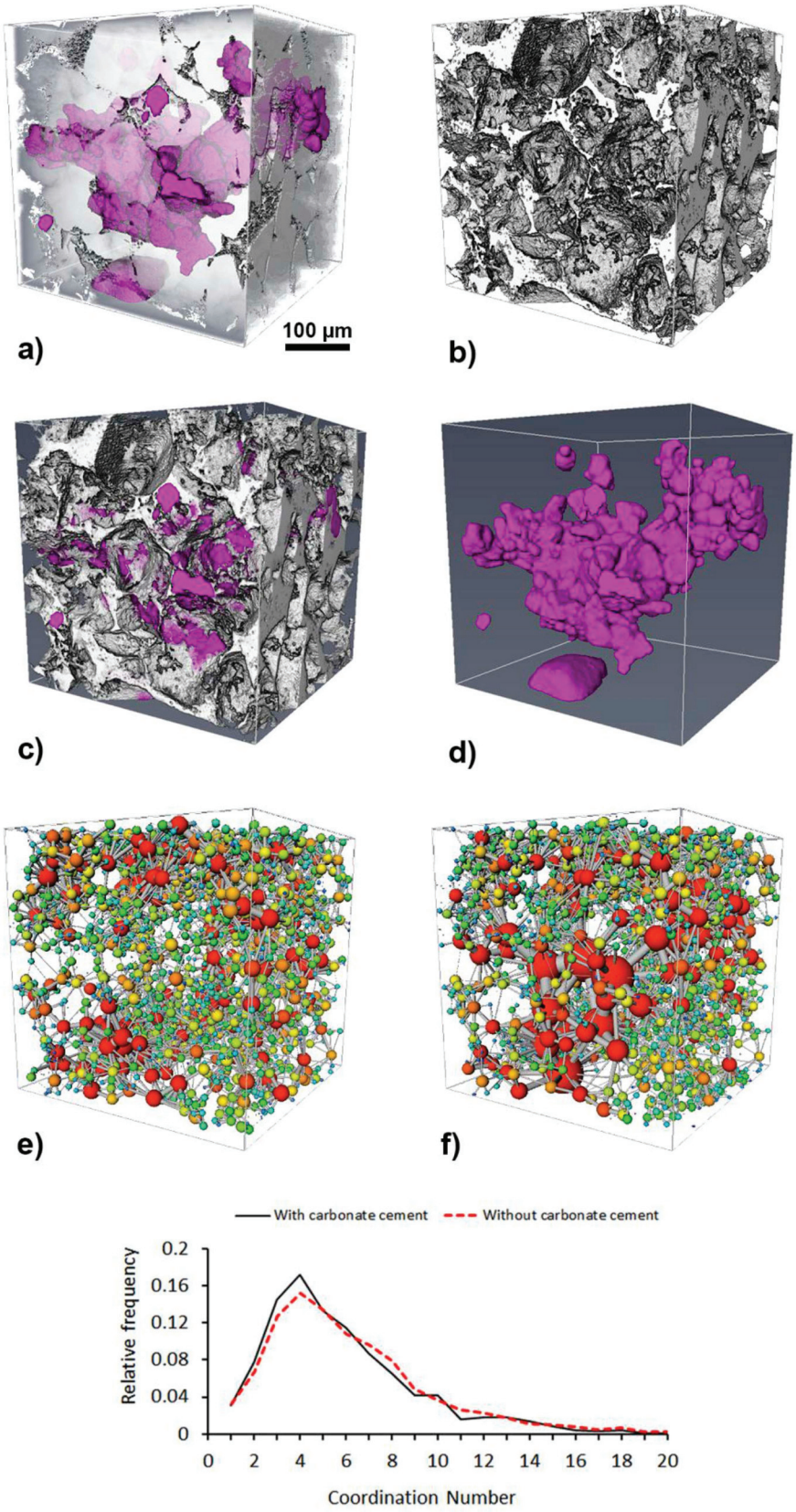

Fig. 21. 3D visualization, 500^3 cube sub-set, of carbonate cement and total porosity in the sandy conglomerate (SCx). (a) Solid phase is white and carbonate cement is in purple. (b) Total porosity. (c) Total porosity (white/grey) and carbonate cement (purple). (d) Carbonate cement visualized in 3D space. (e) Pore-throat network model of total porosity with carbonate cement. (f) Pore-throat network model of total porosity when carbonate cement is removed from the 3D model. A coordination number (number of contacts a pore has with its neighbors) plot on the bottom represents the degree of connectivity within the pores. Note the higher connectivity when the carbonate cement is removed from the 3D model (red dashed line).

diagenetic clay content in the aeolian sandstone sample. The higher microporosity value in the interbedded sandstone sample reflects the very fine grain sizes (< 62.5 µm), where the majority of the total porosity is located below 18.4 µm resolution (16.4%). Macroporosity, which is above the image resolution in the plugs, is generally focused in areas with larger grainsize where the majority of the pores remain disconnected (Fig. 15a). The average macro pore-throat size in the interbedded sandstone sample is 113 µm, while the minimum size is

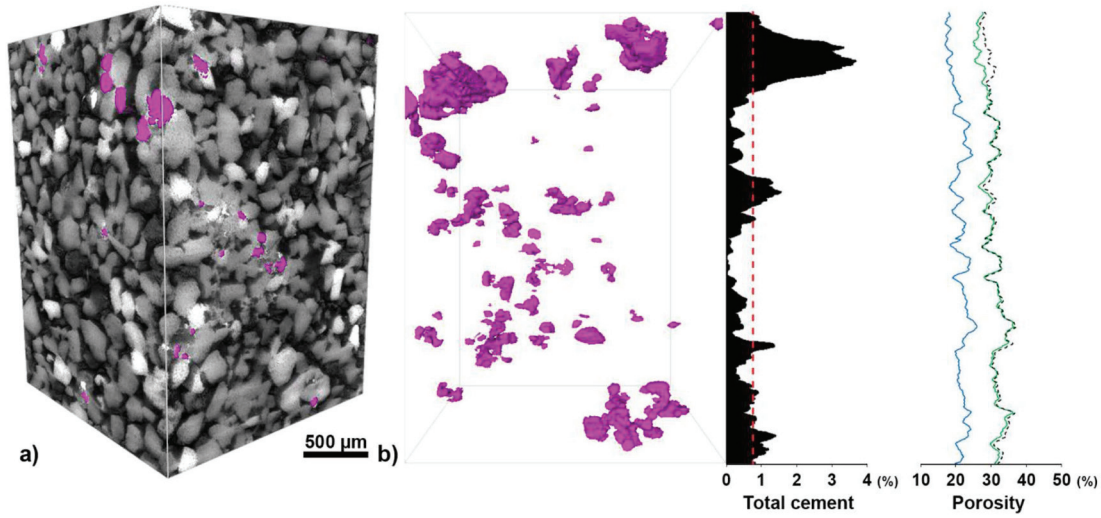

Fig. 22. Example of carbonate cement distribution in 3D in the aeolian sandstone sample (AST). (a) 3D visualization of carbonate cement (purple color) together with different mineral phases (shades of grey). (b) 3D visualization of carbonate cement and profile of total amount of cement along the sample (red dotted line is the average). The left side graphs show the porosity distribution in the samples. The blue (left) curve is macroporosity, middle curve (green) is total porosity (macro- and microporosity), and right dotted line is total porosity when carbonate cement is removed from the 3D model.

20.1 µm. In the aeolian sample the average macro pore-throat size is more than double at 296 µm and the minimum is 18.1 µm. The pore-throats in the aeolian sample are well connected, as shown in the pore and pore-throats network model (Fig. 16). This is contrasting the observations made in the conglomerate samples where the macropores appear disconnected. However, the results of SEM-EDS show that locally the macroporous regions can be occluded by abundance of kaolinite (Fig. 17). This suggests that kaolinite crystals may be partially responsible for permeability reduction in the sandstones, as well as in the conglomerate matrix (c.f. Morris and Shepperd, 1982).

3.3. Carbonate cement

Authigenic carbonate cement (here calcite and dolomite) may have a major impact on the reservoir quality, in controlling porosity and permeability evolution e.g. by reducing permeability by narrowing/closing pore-throats. In this study carbonate cements have been observed occupying both the primary and secondary (replacive) porespace and thus reducing the overall porosity (Fig. 18). The most abundant carbonate cements are found in the very tight conglomerate samples, consequently with a profound impact on the overall reservoir quality. On average, the carbonate cement in the conglomerate matrix is occupying between 2 and 4% of the total 3D volume. In the sandstones the average carbonate cement is < 1%. The carbonate cement represents an early diagenetic phase, including both microcrystalline and poikilotopic non-ferroan carbonate cement (Mahmic et al., 2018). The early diagenetic carbonate cement could in some cases help retain porosity by supporting the framework grains against future compaction, (Bjørlykke, 2014). During the late burial stage, the dissolution of authigenic carbonate cement, due to changes in fluid properties, lead to formation of secondary porosity. Moreover, the secondary porosity which formed by decomposition of the framework grains were pervasively filled by carbonate minerals. Secondary porosity rarely has beneficial effects on reservoir quality, since material from dissolved minerals will commonly precipitate somewhere else (Bjørlykke, 1984).

When 3D data are registered to the 2D SEM-EDS data, it is possible, based on their X-ray attenuations, to differentiate carbonate minerals in the 3D tomogram data set (e.g. Fig. 9). Examples of carbonate cement distribution and how the cement is reducing the macro- and microporosity by occupying primary and secondary porespace in the very tight conglomerate and sandy conglomerate sample respectively are shown in Figs. 19 and 20. This approach gives a much better overview over carbonate cement distribution in the samples, compared to standard optical thin section analysis where only a small part of the sample is visible. The latter can give a partly wrong representation of the amount of carbonate cement in the sample, since the distribution can be highly variable, as observed in Figs. 19 and 20 Fig. 21 show a zoomed sub-set cube of 500^3 µm from sandy conglomerate and the effect of carbonate cement on the total porosity and flow paths. The pore network model (Fig. 21 e and f) show better connectivity with larger pores and pore-throats when carbonate cement is removed from the 3D model. The distinction of carbonate cement phase in the aeolian plug sample (16.6 µm/voxel) within the image volume was ambiguous due to the small crystals size. Therefore the sub-plug sample at 3.1 µm/voxel (Fig. 22) is used to more easily separate the carbonate cement phase. The cement is occupying 0.7% of the total sample, with maximum of 3.5% in one of the tomogram slices, close to the thin section sample. The carbonate cement is patchy and generally has a much lower volume than observed in the conglomerate samples. The overall porosity reduction due to carbonate cement in the aeolian sandstone is consequently much lower than in the conglomerate matrix.

4. Conclusions

In this study we illustrate that the use of dry/wet difference mapping produces better and more accurate characterization of the pore space below image resolution, especially in the heterogeneous and complex reservoir rocks, such as the conglomerate matrix. Furthermore, the use of registration and the accurate alignment of high-resolution 2D SEM-EDS images of thin sections with the corresponding region of the micro-CT 3D image provide further insights. This approach associated with 3D sub-plug samples at higher resolutions, enhances the understanding of the rock material and pore-throat characteristics at different scales.

The clay rich conglomerate matrix samples carry a significant fraction of the porosity in the clay phases (at nanoscale), which have been identified as chlorite, illite, mixed–layer illite/smectite, mixed–layer chlorite/smectite and kaolinite. The macroporosity (above 3D image resolution) in these rocks is unevenly distributed and mostly poorly connected. In the sandstone samples the pores and pore throats are well connected, especially in the aeolian facies.

Compared to the sandstone samples, the conglomerate matrix exhibits strong heterogeneities and the primary pore throats are significantly narrower due to the poor sorting and high proportions of

authigenic clay minerals and cements. The sandy conglomerate samples have a better reservoir quality than the rest of the conglomerate due to a better sorting and higher permeability and porosity.

The amount of carbonate cement and its distribution have an important effect on pore connectivity and flow capacity. The very tight conglomerate samples display the highest amount of carbonate cement compared to the rest of the samples. That the pore connectivity (major fluid pathways) increases when the carbonate cement is removed from the generated 3D digital rock model of the conglomerates matrix. In the sandstone samples the carbonate cement is more patchy and less abundant and does not affect the pore-throat connectivity as much as in the conglomerate matrix. The multi-scale 3D models reconstructed based on the CT data have provided the basis for characterization of macro- and micro pore-throats textures as well as carbonate cement distribution in various Edvard Grieg deposits.

Acknowledgments

The authors would like to thank Lundin Norway AS for sponsoring this project, providing the core material, and for stimulating discussions of the results. Thanks to Berit Løken Berg and Salahalldin Akhavan at the University of Oslo, for helping out with sample preparation and analyses of thin sections. Special thanks to FEI Trondheim AS (Thermo Fisher scientific) for the help with CT scans and helpful discussions. The authors wish to thank (Reinhard Gaupp) and an anonymous MPG reviewer for valuable comments and suggestions.

Appendix A. Supplementary data

Supplementary data to this article can be found online at https://doi.org/10.1016/j.marpetgeo.2018.10.015.

References

Arns, C.H., Bauget, F., Sakellariou, A., Senden, T.J., Sheppard, A.P., Sok, R.M., Ghous, A., Pinczewski, W.V., Knackstedt, M.A., Kelly, J.C., 2005. Digital core laboratory: petrophysical analysis from 3D imaging of reservoir core fragments. Petrophysics 46 (04).

Anovitz, L.M., Cole, D.R., 2015. Characterization and analysis of porosity and pore structures. Rev. Mineral. Geochem. 80 (1), 61–164.

Attwood, D., 2006. Microscopy: nanotomography comes of age. Nature 442 (7103), 642–643.

Avizo, 2017. Avizo software users guide. https://www.fei.com/software/avizo-user-guide, Accessed date: 12 June 2017.

Bin, B., Rukai, Z., Songtao, W., Wenjing, Y., Gelb, J., Gu, A., Xiangxiang, Z., Ling, S.U., 2013. Multi-scale method of Nano (Micro)-CT study on microscopic pore structure of tight sandstone of Yanchang Formation, Ordos Basin. Petrol. Explor. Dev. 40 (3), 354–358.

Bhattad, P., Young, B., Berg, C.F., Rustad, A.B., Lopez, O., 2014. X-ray micro-CT assisted drainage rock typing for characterization of flow behaviour of laminated sandstone reservoirs. In: .International Symposium of the Society of Core Analysts Held in Avignon. France.

Bjørlykke, K., 1984. Formation of secondary porosity: how important is it. Clastic diagenesis: AAPG Memoir 37, 277–286.

Bjørlykke, K., 2014. Relationships between depositional environments, burial history and rock properties. Some principal aspects of diagenetic process in sedimentary basins. Sediment. Geol. 301, 1–14.

Bultreys, T., Van Hoorebeke, L., Cnudde, V., 2015. Multi-scale, micro-computed tomography-based pore network models to simulate drainage in heterogeneous rocks. Adv. Water Resour. 78, 36–49.

Chamley, H., 1989. Clay Sedimentology. Springer-Verlag Berlin Heidelberg, pp. 623.

Cnudde, V., Cnudde, J.P., Dupuis, C., Jacobs, P.J.S., 2004. X-ray micro-CT used for the localization of water repellents and consolidants inside natural building stones. Mater. Char. 53 (2–4), 259–271 (2004).

Cnudde, V., Boone, M.N., 2013. High-resolution X-ray computed tomography in geosciences: a review of the current technology and applications. Earth Sci. Rev. 123, 1–17.

Fheed, A., Krzyżak, A., Świerczewska, A., 2018. Exploring a carbonate reef reservoir—nuclear magnetic resonance and computed microtomography confronted with narrow channel and fracture porosity. J. Appl. Geophys. 151, 343–358.

Goldsmith, P.J., Hudson, G., Van Veen, P., 2003. Triassic. In: The Millennium Atlas: Petroleum Geology of the Central and Northern North Sea. Geological Society, London, pp. 105–127.

Hurst, A., Nadeau, P.H., 1995. Clay microporosity in reservoir sandstones: an application of quantitative electron microscopy in petrophysical evaluation. AAPG Bull. 79 (4), 563–573.

Kalender, W.A., 2006. X-ray computed tomography. Phys. Med. Biol. 51 (13), 29–43.

Knackstedt, M., Golab, A., Riepe, L., 2012. Petrophysical characterization of unconventional reservoir core at multiple scales. In: SPWLA 53rd Annual Logging Symposium. Society of Petrophysicists and Well-Log Analysts.

Lame, O., Bellet, D., Di Michiel, M., Bouvard, D., 2004. Bulk observation of metal powder sintering by X-ray synchrotron microtomography. Acta Mater. 52 (4), 977–984.

Latham, S., Varslot, T., Sheppard, A., 2008. Image registration: enhancing and calibrating X-ray micro-CT imaging. In: Proc. Society of Core Analysts, Abu Dhabi, UAE, SCA2008-S2035.

Laursen, I., Fugelli, E., Lervik, K.S., 1995. Sequence stratigraphic framework of the paleocene and eocene successions, block 16/1, Norwegian North Sea. In: Sequence Stratigraphy on the Northwest European Margin: Proceedings of the Norwegian Petroleum Society Conference, 1-3 February 1993, Stavanger, Norway. Elsevier (5), 471.

Lopez, O., Mock, A., Øren, P.E., Long, H., Kalam, Z., Vahrenkamp, V., Bibrata, M., Seraj, S., Chacko, S., Al Hammadi, M., Al Hosni, H., 2012. Validation of fundamental carbonate reservoir core properties using digital rock physics. In: International Symposium of the Society of Core Analysts, SCA2012-S2019.

Mahmic, O., Dypvik, H., Hammer, E., 2018. Diagenetic influence on reservoir quality evolution, examples from Triassic conglomerates/arenites in the Edvard Grieg field, Norwegian North Sea. Mar. Petrol. Geol. 93, 247–271.

Moraes, M.A., De Ros, L.F., 1990. Infiltrated clays in fluvial Jurassic sandstones of Recôncavo Basin, northeastern Brazil. J. Sediment. Res. 60 (6), 809–819.

Morris, K.A., Shepperd, C.M., 1982. The role of clay minerals in influencing porosity and permeability characteristics in the Bridport Sands of Wytch Farm, Dorset. Clay Miner. 17 (1), 41–54.

NORLEX Project 2012: www.nhm2.uio.no/norlex/StandardLithostratigraphicWallchartOffshoreNorway.pdf.

NPD, 2017. Factpages. http://factpages.npd.no/factpages, Accessed date: 6 June 2017.

Nystuen, J.P., Kjemperud, A.V., Müller, R., Adestål, V., Schomacker, E.R., 2014. Late triassic to early jurassic climatic change, northern North Sea region. In: Martinius, A.W., Ravnås, R., Howell, J.A., Steel, R.J., Wonham, J.P. (Eds.), From Depositional Systems to Sedimentary Successions on the Norwegian Continental Margin. John Wiley and Sons, Ltd, Chichester, UK. https://doi.org/10.1002/9781118920435.ch3.

Nøttvedt, A., Gabrielsen, R., Steel, R., 1995. Tectonostratigraphy and sedimentary architecture of rift basins, with reference to the northern North Sea. Mar. Petrol. Geol. 12, 881–901.

Pak, T., Butler, I.B., Geiger, S., van Dijke, M.I., Jiang, Z., Surmas, R., 2016. Multiscale pore-network representation of heterogeneous carbonate rocks. Water Resour. Res. 52 (7), 5433–5441.

Prodanović, M., Mehmani, A., Sheppard, A.P., 2015. Imaged-based multiscale network modelling of microporosity in carbonates. Geological Society, London, Special Publications 406 (1), 95–113.

Riber, L., Dypvik, H., Sørlie, R., 2015. Altered basement rocks on the Utsira high and its surroundings, Norwegian North Sea. Norw. J. Geol. 93, 57–89.

Riepe, L., Suhaimi, M.H., Kumar, M., Knackstedt, M.A., 2011. Application of high resolution micro-CT-imaging and pore network modeling (PNM) for the petrophysical characterization of tight gas reservoirs-A case history from a deep clastic tight gas reservoir in Oman. In: SPE Middle East Unconventional Gas Conference and Exhibition. Society of Petroleum Engineers.

Roerdink, J.B., Meijster, A., 2000. The watershed transform: definitions, algorithms and parallelization strategies. Fundam. Inf. 41 (1, 2), 187–228.

Rushing, J.A., Newsham, K.E., Blasingame, T.A., 2008. January. Rock typing: keys to understanding productivity in tight gas sands. In: SPE Unconventional Reservoirs Conference. Society of Petroleum Engineers Paper 114164.

Sakdinawat, A., Attwood, D., 2010. Nanoscale X-ray imaging. Nat. Photon. 4 (12), 840–848.

Salem, A.M., Morad, S., Mato, L.F., Al-Aasm, I.S., 2000. Diagenesis and reservoir-quality evolution of fluvial sandstones during progressive burial and uplift: evidence from the upper jurassic boipeba member, reconcavo basin, northeastern Brazil. AAPG (Am. Assoc. Pet. Geol.) Bull. 84 (7), 1015–1040.

Slagstad, T., Davidsen, B., Daly, J.S., 2011. Age and composition of crystalline basement rocks on the Norwegian continental margin: offshore extension and continuity of the Caledonian–Appalachian orogenic belt. J. Geol. Soc. 168, 1167–1185.

Steel, R., Ryseth, A., 1990. The Triassic—early Jurassic succession in the northern North Sea: megasequence stratigraphy and intra-Triassic tectonics. Geological Society, London, Special Publications 55 (1), 139–168.

Steel, R., 1993. Triassic–Jurassic megasequence stratigraphy in the Northern North Sea: rift to post-rift evolution. In: Geological Society, London, Petroleum Geology Conference Series. Geological Society of London, pp. 299–315.

Taylor, T.R., Giles, M.R., Hathon, L.A., Diggs, T.N., Braunsdorf, N.R., Birbiglia, G.V., Kittridge, M.K., Macaulay, C.I., Espejo, I.S., 2010. Sandstone diagenesis and reservoir quality prediction: models, myths, and reality. AAPG (Am. Assoc. Pet. Geol.) Bull. 94 (8), 1093–1132.

Worden, R.H., Morad, S., 2003. Clay minerals in sandstones: controls on formation, distribution and evolution. In: Worden, R.H., Morad, S. (Eds.), Clay Mineral Cements in Sandstones, pp. 1–41.

Ziegler, P.A., 1975. Geologic evolution of North Sea and its tectonic framework. AAPG (Am. Assoc. Pet. Geol.) Bull. 59 (7), 1073–1097.

Ziegler, P.A., 1990. Tectonic and paleogeographic development of the North Sea rift system. In: In: Blundell, D.J., Gibbs, A.D. (Eds.), Tectonic Evolution of the North Sea Rifts: International Lithosphere Programme, vol. 181. pp. 1–36.

Ziegler, P.A., 1992. North Sea rift system. Tectonophysics 208, 55–75. https://doi.org/10.1016/0040-1951(92)90336-5.